



Improving the GBT-based buckling analysis of restrained thin-walled members by considering constrained deformation modes

Heitor de Freitas Araujo¹, Thiago Gonçalves da Silva¹, Cilmar Basaglia¹, Dinar Camotim²

Abstract

This work reports the development, numerical implementation and illustration of a novel/improved approach to perform the buckling analysis of braced/restrained cold-formed steel members by means of Generalized Beam Theory (GBT). The novelty consists of a cross-section analysis procedure that incorporates elastic restraints and, therefore, leads to a set of constrained deformation modes with clear structural meaning for the member under consideration. The potential of the developed GBT-based approach is illustrated by presenting and discussing numerical results concerning cold-formed steel (i) purlins restrained by sheeting and (ii) studs braced by sheathing. For validation and assessment purposes, several GBT-based results are compared with values provided by the programs GBTUL2.0 (conventional GBT), CUFSM (finite strip method) and/or ANSYS (shell finite elements). It is shown that the proposed GBT-based approach is much more efficient than the conventional one – same accuracy achieved with much less computational effort. Moreover, it also offers the possibility of obtaining accurate buckling results with very few (constrained) deformation modes – this feature makes it possible to derive semi-analytical formulae to calculate critical buckling loadings of braced/restrained members. This capability is used in this work to derive GBT-based semi-analytical formulae providing critical length and buckling loading estimates for cold-formed steel purlins and studs restrained by panels (sheeting or sheathing).

1. Introduction

In practical applications, many cold-formed steel members (CFS) are often continuously restrained along their lengths – *e.g.*, purlin-sheeting or sheathed wall stud systems (see Figs. 1(a)-(b)). Most of these braced CFS members exhibit very slender cross-sections, a feature rendering them highly prone to geometrically nonlinear effects, namely those related to local, distortional and/or global (flexural or flexural-torsional) buckling, as well as to interactive behaviors involving more than one of them (*e.g.*, local-distortional or lateral-distortional buckling). Indeed, a fair amount of research work has been recently devoted to the development of efficient design rules for CFS members connected to (restrained by) panels, such as purlins restrained by sheeting or studs braced by sheathing. The most relevant outputs of this research activity are design procedures based on the Direct Strength Method (DSM – *e.g.*, Camotim *et al.* 2016, Schafer 2019), now widely accepted as a very efficient approach to design

¹ FEC, DES, University of Campinas, Brazil.

² CERIS, DECivil, Instituto Superior Técnico, Universidade de Lisboa, Portugal. <dcamotim@ist.utl.pt>

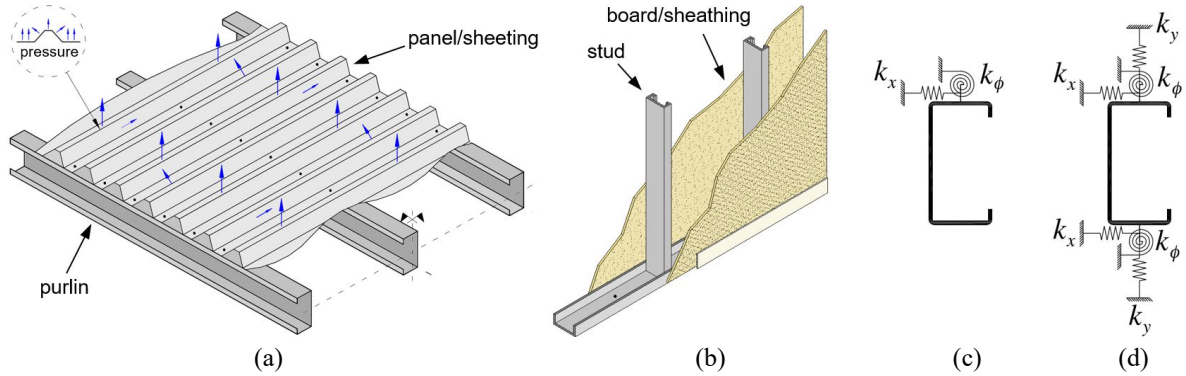


Figure 1: (a) Purlin-sheeting system under wind uplift, (b) sheathed wall stud system, and longitudinally continuous elastic springs used to model the restraints provided by the panel and board/sheathing to (c) purlins and (d) studs.

CFS columns and beams – the member load-carrying capacity is predicted on the sole basis of its elastic buckling and yield loads or moments. In this context, it is worth noting the DSM-based procedures proposed by (i) Gao & Moen (2014) and Ren *et al.* (2016), for purlin-sheeting systems, and by (ii) Vieira Jr. & Schafer (2013) and Selvaraj & Madhavan (2018), for sheathed wall stud systems. In particular, a DSM-based design procedure for restrained members has already been included in the latest edition of the North American Specification for cold-formed steel structural members (AISI 2016, Schafer 2013).

The determination of member buckling loads and moments, required to apply the DSM, is made by means of buckling analyses using the Finite Strip Method (FSM) or Generalized Beam Theory (GBT), due to the availability of the easily accessible and user-friendly computer programs CUFSM (Li & Schafer 2010) and GBTUL 2.0 (Bebiano *et al.* 2010). When calculating the elastic buckling loads/moments, the restraints provided by the sheathing/board or sheeting/panel to the member are simulated by means of longitudinally continuous rotational and/or translational elastic springs (Figs. 1(c)-(d)). The stiffness values of such springs are taken from either experimental tests or simple equations describing the mechanics of simplified structural models (*e.g.*, Schafer 2013, Gao & Moen 2012, Vieira Jr. 2011).

In GBT, which incorporates genuine plate theory concepts (thus accounting for cross-section in-plane and out-of-plane deformations), the cross-section displacement field is expressed as a linear combination of pre-determined deformation modes, which makes it possible to cast the equilibrium equations and boundary conditions in a very convenient unique format. Since first introduced by Richard Schardt (*e.g.*, Schardt 1989), GBT has been considerably developed, mostly by the Lisbon-based research group (*e.g.*, Camotim *et al.* 2010 and Camotim & Basaglia 2013 – an updated list of publications can be found in <http://www.civil.ist.utl.pt/gbt>), but also by other researchers (*e.g.*, Casafont *et al.* 2000, Taig & Ranzi 2015, Miranda *et al.* 2015, Cai & Moen 2016, Duan & Zhao 2019, Muresan *et al.* 2019). The performance of GBT structural analyses involves two main tasks, namely (i) the *cross-section analysis* (*e.g.*, Silvestre & Camotim 2002, Gonçalves *et al.* 2010 and Bebiano *et al.* 2015, to identify the deformation modes and evaluate the associated modal mechanical properties, and (ii) the *member analysis* (first order, buckling, vibration, *etc.*), involving the solution of the appropriate differential equilibrium equations and the interpretation of the (modal) results obtained (*e.g.*, Silvestre & Camotim 2003, Bebiano *et al.* 2018a).

Two approaches can be followed to perform GBT structural analyses in restrained thin-walled members. The first one consists of incorporating the restraints directly in the cross-section analysis, modeling them with longitudinally continuous translational and/or rotational elastic springs – *i.e.*,

they are taken into account at the deformation mode determination stage. This approach was adopted (i) by Schardt (1989), in the context of the first-order analysis of purlins restrained by sheeting under downward loading, and (ii) by Jiang & Davies (1997) and Jiang *et al.* (1994), to perform buckling analyses of restrained purlins subjected to uplift loading – however, these authors dealt exclusively with either (i) global deformations and (ii) very specific types of distortional deformations. Heinz (1994) adopted a similar approach to propose a simplified procedure to analyze the buckling behavior of those same restrained purlins: the constrained/“non-standard” global deformation modes are obtained by linearly combining their unrestrained/standard counterparts. Recently, Taig and Ranzi (2014) used this approach to develop a methodology in which a cross-section discrete model (obtained by a finite element procedure) and transversally distributed springs are employed to obtain the deformation modes of thin-walled members with stiffened cross-sections (*e.g.*, cross-sections with intermediately stiffened walls).

The second approach consists of performing a standard cross-section analysis (no restraints considered), which means that the deformation modes determined concern the unrestrained member cross-section. The influence of the restraints (elastic springs) is incorporated only at the member analysis stage (as constraint equations). This approach was proposed by the Lisbon-based research group and adopted in most of its works – those due to Camotim *et al.* (2008) and Basaglia *et al.* (2013) are worth noting. Moreover, this approach has been incorporated in the computer program GBTUL 2.0 (Bebiano *et al.* 2010), in the context of arbitrary deformation patterns – it amounts to combining the standard/unconstrained deformation modes at the member analysis stage. However, it should be pointed out that this second approach only leads to accurate buckling results if a large amount of deformation mode are included in the analysis, which lowers its computational efficiency. In addition, it may also be argued that using standard/unconstrained deformation modes, which do not adequately reflect the member mechanics, is bound to “cloud” the structural interpretation of the results obtained.

The aim of this work is to present and illustrate the implementation and application of a novel GBT-based approach for the buckling analysis of continuously braced open-section cold-formed steel members, based on an improved cross-section analysis procedure that incorporates elastic restraints – it enhances and outperforms the GBT procedure employed in Schardt (1989), Jiang & Davies (1997) and Jiang *et al.* (1994) to determine the cross-section deformation modes. The output of this procedure is a set of “constrained deformation modes” that reflect accurately the mechanics of the particular restrained member under scrutiny, thus making it possible to obtain accurate local, distortional and/or global buckling results with only a few deformation modes³. After describing in detail the concepts and procedures involved in determining the constrained deformation modes, the paper illustrates the advantages of their use in the GBT-based buckling analysis of restrained CFS members, namely (i) purlins restrained by sheeting and (ii) studs braced by sheathing. Then, it is shown that using constrained deformation modes makes it possible to derive semi-analytical formulae to estimate (with high accuracy) critical buckling loadings of continuously braced/restrained CFS members⁴. This capability is illustrated through the derivation of GBT-based semi-analytical formulae providing very accurate critical lengths and bifurcation loadings of CFS purlins and studs braced/restrained by panels. For validation and assessment purposes, some GBT-based results are compared

³ Preliminary findings on the determination of the “constrained deformation modes”, as well as on the advantages of their use, were recently reported by the authors Silva *et al.* (2019).

⁴ The semi-analytical designation stems from the fact that using the derived formulae requires solving, numerically, an auxiliary standard eigenvalue problem – note, however, that this eigenvalue problem is defined in a fully analytical fashion.

with values either provided by the programs CUFMS (Li & Schafer 2010) or GBTUL2.0 (Bebiano *et al.* 2010), or obtained by means of ANSYS (SAS 2013) shell finite element analyses (SFEA).

It is worth noting that, in the derivations and equations presented throughout the paper, (i) all scalar quantities, including the matrix components, are denoted by *italic letters*, (ii) a virtual variation is denoted by δ , (iii) tensor notation is employed, (iv) a subscript preceded by a comma indicates differentiation (e.g., $(\cdot)_{,x} \equiv d(\cdot)/dx$) and (v) Einstein's summation convention is adopted. Matrix and vector components are identified by square ($[]$) and curly ($\{ \}$) brackets, respectively – however, when specifying components is not necessary, matrices and vectors are identified by **normal bold** and *italic bold* symbols, respectively.

2. Proposed GBT Approach

Modeling the continuous restraint/bracing provided by sheeting, a panel or a slab to a given structural member involves the addition of longitudinally distributed in-plane translational and/or rotational elastic springs. Fig. 2(a) illustrates this modeling for the case of a stud-sheathing assembly: the influence of the restraint provided by the external sheathing board is simulated by translational (vertical/normal and horizontal/tangential – stiffness values K_{TN} and K_{TG} , respectively) and rotational (stiffness K_R) elastic springs continuously attached to the lipped channel stud along the longitudinal line corresponding to the flange mid-point. Naturally, a full restraint (infinite stiffness) means that the corresponding generalized displacement is completely prevented.

Consider the arbitrary prismatic thin-walled open cross-section member schematically displayed in Fig. 2(b), which is deemed (i) formed by n walls (plate elements), each divided into various wall segments with width b_i , and (ii) restrained by continuous translational and rotational elastic springs located at points P_{TN} (wall segment ends or mid-points), P_{TG} (wall segment ends) or P_R (wall segment mid-points). Also shown in Fig. 2(b) are the wall/local coordinate axes x , s and z , respectively along the member axis, cross-section mid-line and wall thickness. In order to obtain a displacement field representation compatible with the classical beam theory, each displacement component $u(x, s)$, $v(x, s)$ and $w(x, s)$ at any given cross-section mid-line point must be expressed as a combination of orthogonal functions. Therefore, one has

$$u(x, s) = u_i(s)\varphi_{i,x}(x) \quad v(x, s) = v_i(s)\varphi_i(x) \quad w(x, s) = w_i(s)\varphi_i(x) \quad (1)$$

where (i) $u_i(s)$, $v_i(s)$, $w_i(s)$ are shape functions used to approximate the cross-section displacement field and (ii) $\varphi_i(x)$ are non-dimensional amplitude functions defined along the member length – information on the derivation of these expressions can be found in the work of Silvestre & Camotim (2002).

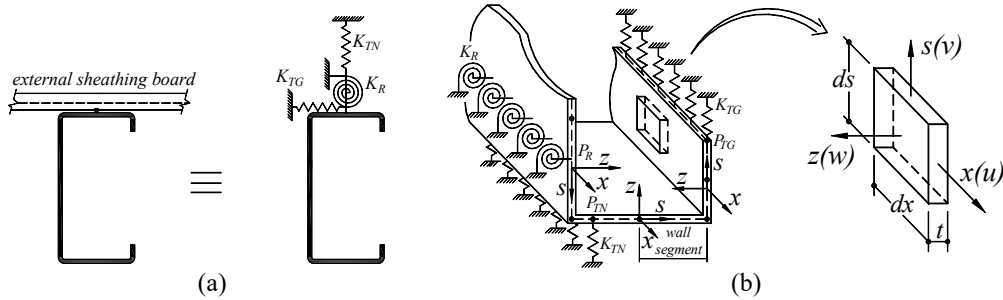


Figure 2: (a) Modeling a lipped channel stud-sheathing assembly with longitudinally distributed translational and rotational elastic springs, and (b) arbitrary continuously restrained thin-walled member and wall/local coordinate axes.

The equations providing the member buckling behavior, taking into account the presence of elastic constraints (springs), are obtained by imposing the stationarity of the total potential energy functional

$$V = \frac{1}{2} \int_{\Omega} \sigma_{ij} \varepsilon_{ij} d\Omega + \frac{1}{2} \int_L K \Delta_r^2 dx \quad (2)$$

in the close vicinity of the member fundamental equilibrium path (adjacent equilibrium). Note that (i) Ω is the member volume (n walls), (ii) σ_{ij} and ε_{ij} are the second Piola-Kirchhoff stress and Green-Lagrange strain tensors, respectively, both including pre-buckling and bifurcated components, (iii) L is the member length, (iv) K is the stiffness of a longitudinally distributed continuous (along an axis r) spring and (v) Δ is the corresponding spring generalized displacement (translation or rotation) – the summation convention applies to subscripts i and j . Then, the equilibrium equations defining the member buckling eigenvalue problem are obtained by (i) linearising the first variation of the total potential energy functional, at the fundamental equilibrium path, and (ii) discarding the pre-buckling strains, thus yielding

$$\delta V = \int_L \left(\delta \boldsymbol{\varphi}_{,xx}^T \mathbf{C} \boldsymbol{\varphi}_{,xx} + \delta \boldsymbol{\varphi}_{,x}^T \mathbf{D}^I \boldsymbol{\varphi}_{,x} + \delta \boldsymbol{\varphi}_{,xx}^T \mathbf{D}^{II} \boldsymbol{\varphi} + \delta \boldsymbol{\varphi}^T \mathbf{D}^{II} \boldsymbol{\varphi}_{k,xx} + \delta \boldsymbol{\varphi}^T \mathbf{B} \boldsymbol{\varphi} + \lambda \mathbf{W}_j^0 \delta \boldsymbol{\varphi}_{,x}^T \mathbf{X}_j \delta \boldsymbol{\varphi}_{,x} \right) dx = 0 \quad (3)$$

with

$$\mathbf{B} = \mathbf{B}^f + \mathbf{B}^s \quad (4)$$

where (i) λ is the load parameter, (ii) $\boldsymbol{\varphi}$ is a vector containing the longitudinal amplitude functions of the cross-section shape functions, (iii) \mathbf{W}_j^0 is a vector whose components are the normal stress resultants profiles associated with uniform internal forces and bending moments j , (iv) \mathbf{B}^s is a matrix associated with the elastic strain energy stored in the translational and rotational springs (novel feature of the proposed approach that is addressed in Section 2.1 – see Eq. (10)), (v) \mathbf{C} , \mathbf{D}^I , \mathbf{D}^{II} , and \mathbf{B}^f are cross-section stiffness matrices and (vi) \mathbf{X}_j is a geometric stiffness matrix associated with the pre-buckling longitudinal normal stresses σ_{xx}^0 . In members with uniform wall thickness (those dealt with in this work), the various matrix components C_{ik} , D_{ik}^I , D_{ik}^{II} , B_{ik}^f and X_{jik} are given by the expressions

$$C_{ik} = E t \int_b u_i u_k ds + \frac{E t^3}{12(1-\nu^2)} \int_b w_i w_k ds \quad (5)$$

$$B_{ik}^f = \frac{E t^3}{12(1-\nu^2)} \int_b w_{i,ss} w_{k,ss} ds \quad (6)$$

$$D_{ik}^I = \frac{G}{3} \int_b t^3 w_{i,s} w_{k,s} ds \quad D_{ik}^{II} = \frac{\nu E}{12(1-\nu^2)} \int_b t^3 w_i w_{k,ss} ds \quad D_{ik} = D_{ik}^I - (D_{ik}^{II} + D_{ki}^{II}) \quad (7)$$

$$X_{jik} = \frac{E t}{C_{jj}} \int_b u_j (v_i v_k + w_i w_k) ds \quad (8)$$

with C_{jj} related to \mathbf{W}_j^0 or σ_{xx}^0 by means of

$$W_j^0 = C_{jj} \varphi_{j,xx}^0 = \sigma_{xx}^0 / \lambda E u_j \quad (9)$$

and where (i) E , ν and G are the steel Young's modulus, Poisson's ratio and shear modulus, (ii) b is the cross-section mid-line overall width and (iii) $u_j \varphi_{j,xx}^0$ stand for the pre-buckling axial displacement field⁵.

2.1 Cross-section Analysis Procedure

The determination of the GBT deformation modes and evaluation of the corresponding cross-section modal mechanical properties require the performance of a cross-section analysis. In the case of unrestrained CFS members exhibiting open cross-section without branching nodes (those dealt with in this work, namely zed-section purlins and lipped channel studs), such analysis involves a sequential procedure that is well documented in the literature (e.g., Schardt 1989, Silvestre & Camotim 2002). The modifications required to take into account the presence of the elastic springs modeling the member restraints/braces are addressed in detail next. For the sake of completion and benefit of the interested reader, the whole cross-section analysis procedure is described, even if the concepts and procedures not directly linked to the addition of the elastic springs are presented in an abbreviated form. The determination of the deformations modes and modal mechanical properties of a continuously restrained open cross-section without branching nodes comprises the following major steps⁶:

- (i) Cross-section discretization involving necessarily $n+1$ natural nodes (ends of the n walls forming the cross-section) and a variable number m of intermediate nodes (located within the walls). Fig. 3(a) shows a possible GBT discretization of a plain channel cross-section – four natural nodes and one intermediate node per wall (located at the mid-point), defining a total of six wall segments.

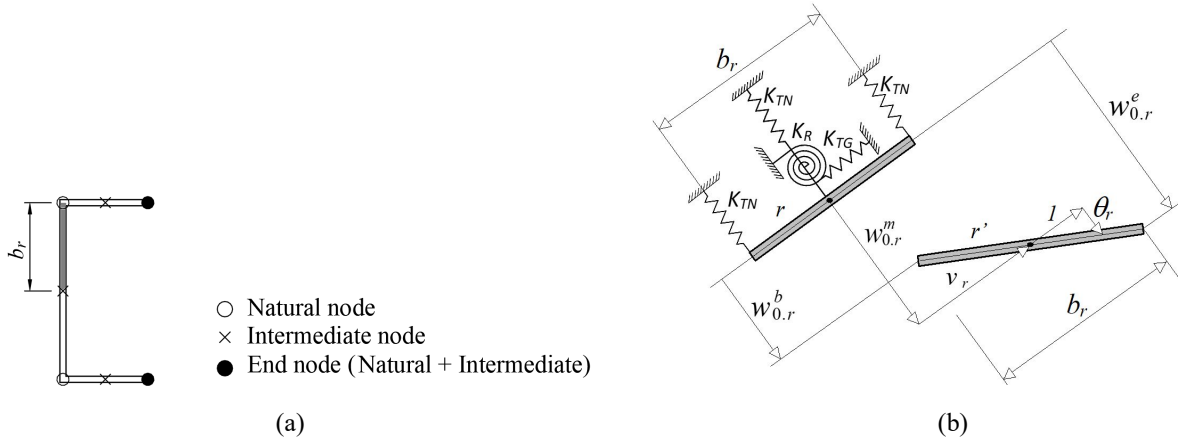


Figure 3: (a) Possible GBT discretization of a plain channel cross-section and (b) springs and rigid-body rotation and translations concerning a wall segment r

⁵ GBT equilibrium equations defining the buckling eigenvalue problem of members acted by general/arbitrary loadings were very recently presented in Bebiano *et al.* (2018b). The main feature is the need to account for the presence of arbitrary pre-buckling stress distributions, which may consist of any possible combination of the stress tensor membrane components σ_{xx}^0 , σ_{ss}^0 and τ_{xs}^0 (in plane stress states).

⁶ Naturally, it is also possible to determine deformations modes and calculate modal mechanical properties for continuously restrained members with more general cross-sections, namely those exhibiting branching nodes and/or closed cells. Since their GBT cross-section analysis is more complex (see Bebiano *et al.* 2015, Silvestre & Camotim 2003) and they have no bearing on the work reported in this paper, it was decided to address here only open cross-section without branching nodes. More general cross-sections will be addressed in the future.

- (ii) Determination of the elementary displacement functions $u_{0i}(s)$ and $w_{0p}(s)$, by sequentially imposing unit warping displacements ($u=1$) at each natural node i and unit flexural displacements ($w=1$) at each intermediate node p . Note that the cross-section end nodes are treated as both natural and intermediate, which means that both unit warping flexural displacements are imposed at them.
- (iii) Definition of initial shape functions $u_i(s)$ from the elementary warping displacements, *i.e.*, $u_i(s)=u_{0i}(s)$.
- (iv) Adoption of the null membrane shear strain and transverse extension assumptions and, using the conventional GBT procedure (*e.g.*, Schardt 1989, Silvestre & Camotim 2002), determine the transverse displacements occurring between the transversal edges of each wall segment. Since the initial warping displacements vary linearly with s , the initial membrane transverse displacement functions $v_i(s)$ are constant in each wall.
- (v) Determination of matrix \mathbf{B}^s , associated with the restraining elastic springs and given by

$$\mathbf{B}^s = \mathbf{F}_{\mathbf{w},\mathbf{b}}^T \mathbf{K}_{\mathbf{TN}} \mathbf{F}_{\mathbf{w},\mathbf{b}} + \mathbf{F}_{\mathbf{w},\mathbf{e}}^T \mathbf{K}_{\mathbf{TN}} \mathbf{F}_{\mathbf{w},\mathbf{e}} + \mathbf{F}_{\mathbf{w},\mathbf{m}}^T \mathbf{K}_{\mathbf{TN}} \mathbf{F}_{\mathbf{w},\mathbf{m}} + \mathbf{F}_{\mathbf{v}}^T \mathbf{K}_{\mathbf{TG}} \mathbf{F}_{\mathbf{v}} + \mathbf{F}_{\boldsymbol{\theta}}^T \mathbf{K}_{\mathbf{R}} \mathbf{F}_{\boldsymbol{\theta}} \quad (10)$$

where (v1) matrices $\mathbf{F}_{\mathbf{w},\mathbf{b}}$ and $\mathbf{F}_{\mathbf{w},\mathbf{e}}$ and $\mathbf{F}_{\mathbf{w},\mathbf{m}}$ contain the elementary nodal flexural displacements at each wall segment beginning ($w_{0,r}^b$), end ($w_{0,r}^e$) and mid-point ($w_{0,r}^m = (w_{0,r}^b + w_{0,r}^e)/2$), respectively, (v2) matrix $\mathbf{F}_{\mathbf{v}}$ contains the transverse membrane displacements of each wall segment (v_r), (v3) matrix $\mathbf{F}_{\boldsymbol{\theta}}$ contains the rigid-body rotations of each wall segment ($\theta_r = (w_{0,r}^e - w_{0,r}^b)/b_r$) and (v4) $\mathbf{K}_{\mathbf{TN}}$, $\mathbf{K}_{\mathbf{TG}}$ and $\mathbf{K}_{\mathbf{R}}$ are diagonal matrices whose non-null components correspond to the translational and rotational spring stiffness values of the restrained wall segments ($K_{\mathbf{TN}}$, $K_{\mathbf{TG}}$ or $K_{\mathbf{R}}$) – Fig. 3(b) shows, for an arbitrary wall segment r , the rigid-body in-plane displacements and rotation, as well as all possible restraining springs.

- (vi) Determination of the initial flexural displacement functions $w_i(s)$, which must ensure, at the cross-section nodes, (vi1) compatibility between the in-plane transverse displacements $v_i(s)$ and $w_i(s)$ and/or (vi2) the continuity of the flexural rotations $w_{i,s}(s)$. The determination of such functions involves two tasks, namely (vi1) the evaluation of the nodal flexural displacements caused by the elementary warping and flexural displacement functions, and (vi2) the solution of a statically indeterminate folded-plate problem, by means of the force method (see (*e.g.*, Schardt 1989, Silvestre & Camotim 2002).
- (vii) At this stage, the cross-section initial shape functions $u_i(s)$, $v_i(s)$ and $w_i(s)$ are known⁷, which makes it possible to calculate matrices \mathbf{B} , \mathbf{C} , \mathbf{D} (linear matrices) and \mathbf{X}_1 (geometric matrix associated with uniform compression) – recall that the elastic strain energy stored in the springs is accounted for by the matrix \mathbf{B}^s (see Eqs. (4) and (10)). Fully populated matrices (highly coupled equilibrium equations) are obtained, whose components have no obvious/clear structural meaning.
- (viii) The identification of the cross-section corresponding deformation modes (final shape functions) $\bar{u}_k(s)$, $\bar{v}_k(s)$, $\bar{w}_k(s)$ and the calculation of the associated cross-section modal mechanical properties constitute the GBT “trademark” and are addressed in Section 2.1.1. They involve the simultaneous diagonalization of matrices \mathbf{C} and \mathbf{B} , by means of a sequence of basis changes, which uncouples the member equilibrium equation system as much as possible and, at the same time, makes it possible to obtain stiffness matrix components with clear structural meanings.

⁷ Note that the initial shape functions are determined before the elastic restraints are taken into account, which leads to a simple and well-known numerical implementation that requires a low computational effort.

2.1.1 Identification and characterization of the constrained deformation modes

The concepts and procedures involved in the proposed novel approach to determine the constrained deformation modes for unbranched open thin-walled cross-section are addressed next. In order to provide a better grasp of these concepts and procedures, the main steps and operations are illustrated through their application to the zed-section ($Z 102 \times 52 \times 11 \times 2.0$) and lipped channel ($C 102 \times 52 \times 11 \times 2.0$) cross-sections shown in Fig. 4(a) – their dimensions, elastic constants and GBT discretizations are also depicted. On the basis of the discretizations shown, the GBT cross-section analysis leads to sets of 18 ($n+p+3$) deformation modes. As for Fig. 4(b), it provides the unrestrained (**Z0** and **C0**) and restrained (**Z1** to **Z3** and **C1** to **C3**) cross-sections, as well as the spring stiffness values.

While the available GBT cross-section analysis procedures (*e.g.*, Silvestre & Camotim 2002, Jiang & Davies 1997, Jiang *et al.* 1994) involve solving three auxiliary eigenvalue problems whose eigenvectors are the standard/unconstrained deformation modes (final base functions), the methodology proposed herein leads to constrained deformation modes and requires (i) solving one, two or three auxiliary eigenvalue problems, involving matrices **B**, **C**, **D** and **X_i** (all calculated with the initial shape functions $u_i(s)$, $v_i(s)$ and $w_i(s)$) and also (ii) performing “cross-section rotation analysis” procedures for some eigenvectors obtained from the first auxiliary eigenvalue problem – these operations are addressed below. The numbers of eigenvalue problems solved and cross-section rotation analyses performed depend on the arrangement, nature (translational or rotational) and stiffness values of the cross-section constraints (springs). Each eigenvalue problem solution corresponds to a different “stage” and superscripts “1, 2 or 3” identify the eigenvalues and eigenvectors concerning the associated stage – no subscript is needed to identify the rotations, since all required rotation analyses are performed in Stage 1.

- (I) **Stage 1.** This stage separates the deformation modes involving transverse plate bending and/or spring deformations from those associated exclusively with rigid-body motions without spring deformations. This is achieved by solving the auxiliary eigenvalue problem

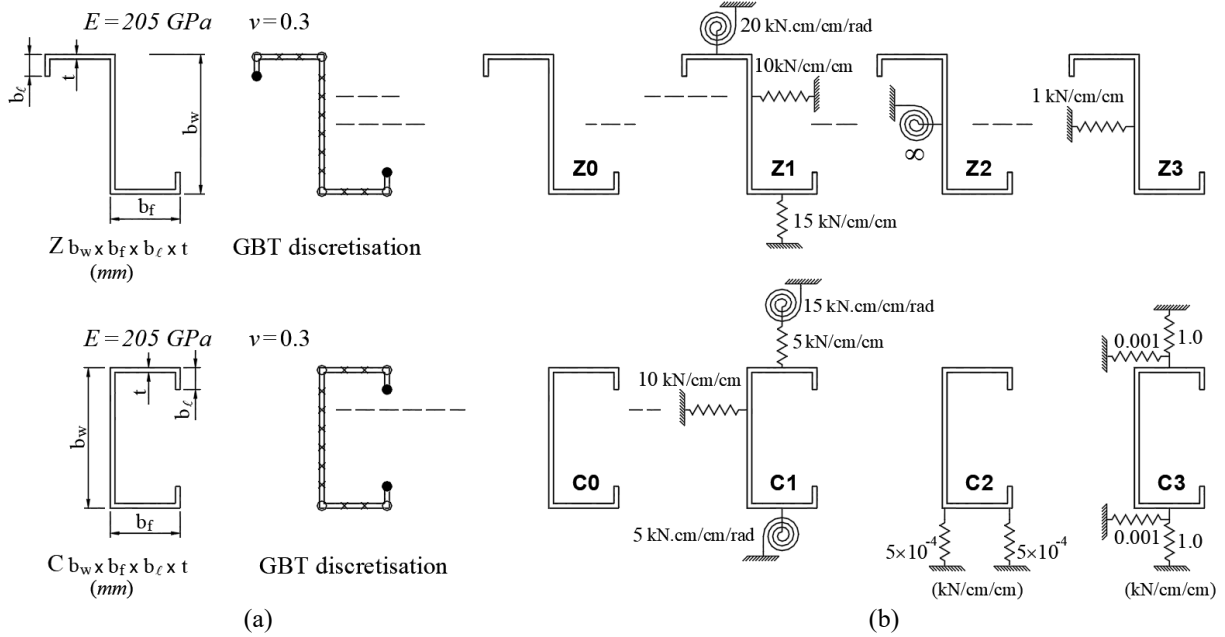


Figure 4: (a) Zed-section and lipped channel dimensions and GBT discretizations, and (b) schematic representations of the unrestrained (**Z0** and **C0**) and restrained (**Z1** to **Z3** and **C1** to **C3**) cross-sections

$$([B_{ik}] - \lambda_k^1 [C_{ik}]) \{a_k^1\} = 0 \quad (11)$$

which has $n+p+3$ eigenvalues λ_k^1 , all with finite positive or null values. It may also be necessary to perform, for some deformation modes associated with the first four eigenvalues that are positive ($\lambda_k^1 > 0$ and $k \leq 4$), cross-section rotation analyses. They are intended to obtain, for each deformation mode, the rotations of the cross-section wall segment chords with respect to their initial (undeformed) positions (see Fig. 3(b)) – θ_{r1} to θ_{r4} values (r is the number of wall segments considered). For each deformation mode k considered, the wall segment chord rigid-body rotations are either (i) all null ($\theta_{rk}=0$: axial extension and/or major/minor axis bending modes), (ii) all non-null and equal ($\theta_{rk}=\theta_k$: torsion and/or coupled bending-torsion modes – these last modes are cast in the form of torsion modes about points not coinciding with the shear centre, which are the poles of the corresponding sectorial areas) or (iii) not all equal ($\theta_{pk} \neq \theta_{qk}$: modes involving local and/or distortional deformations). Concerning the information extracted from the outputs of first auxiliary eigenvalue problem (first four eigenvalues) and subsequent necessary cross-section rotation analyses, it is worth noting that:

- (i) The eigenvectors corresponding to positive eigenvalues ($\lambda_k^1 > 0$) are associated with either (i1) only global deformation modes ($[B_{ik}^s] > 0$ and $[B_{ik}^f] = 0$: major/minor axis bending, torsion and coupled bending-torsion modes – $\theta_{rk}=0$ and $\theta_{rk}=\theta_k$), for $k \leq 4$, (i2) modes combining global and local and/or distortional deformations ($[B_{ik}^s] > 0$ and $[B_{ik}^f] > 0$ – $\theta_{pk} \neq \theta_{qk}$), for $k \leq 4$, or (i3) modes involving exclusively local and/or distortional deformations ($[B_{ik}^s] \geq 0$ and $[B_{ik}^f] > 0$), for $k \geq 5$.
 - (ii) The eigenvectors corresponding to null eigenvalues ($\lambda_k^1 = 0$ – $k \leq 4$) are always associated with global (rigid-body) deformation modes not involving spring deformations⁸ – their stiffness values stem solely from $[C_{ik}]$. Since every vector in this subspace is an eigenvector, none of these rigid-body deformation modes can be identified – this identification has to be made in the subsequent stages.
 - (iii) All the eigenvectors corresponding to deformation modes identified in Stage 1 are normalized as proposed in Silvestre & Camotim (2002) and collected in matrix $[\bar{A}^1]$.
- (II) **Stage 2.** This stage separates the deformation modes involving a rigid-body rotation from the remaining (unidentified) global deformation mode(s). This is achieved by solving the auxiliary eigenvalue problem

$$([\hat{D}_{ik}^2] - \lambda_k^2 [\hat{C}_{ik}^2]) \{a_k^2\} = 0 \quad (12)$$

which corresponds to the simultaneous diagonalization of matrices $[\hat{C}_{ik}^2]$ and $[\hat{D}_{ik}^2]$. These matrices are obtained from the sub-matrices of $[C_{ik}]$ and $[D_{ik}]$ (i) corresponding to the subset of the first four eigenvectors of Eq. (11) with null eigenvalues and (ii) calculated for the associated shape functions⁹. The calculation of $[\hat{C}_{ik}^2]$ and $[\hat{D}_{ik}^2]$ is done by means of Eqs. (5) and (7), respectively, and the aforementioned shape functions are grouped in matrices \mathbf{U}^2 and \mathbf{W}^2 , obtained from

⁸ Because no longitudinal restraints/springs are considered in this work, a null eigenvector corresponding to the axial extension deformation mode always exists.

⁹ In the conventional cross-section analysis (no restraints), the sub-matrices of $[C_{ik}]$ and $[D_{ik}]$ always have dimension 4×4 and correspond to the four null eigenvalues of Eq. (11) (see Silvestre & Camotim 2002, Bebbiano *et al.* 2005).

$$\mathbf{U}^2 = \mathbf{U}^i \hat{\mathbf{Y}}^1 \quad \mathbf{W}^2 = \mathbf{W}^i \hat{\mathbf{Y}}^1 \quad (13)$$

where (i) $\hat{\mathbf{Y}}^1$ is a sub-matrix formed by the eigenvectors under consideration and (ii) the columns of matrices \mathbf{U}^i and \mathbf{W}^i correspond to the initial shape function components $u_i(s)$ and $w_i(s)$. The solution of the second auxiliary eigenvalue problem provides the following information:

- (i) The eigenvector corresponding to the positive eigenvalue ($\lambda_k^2 > 0$) provides the torsion or coupled bending-torsion deformation mode, none involve spring deformation – the bending-torsion mode is again cast in the form of a torsion mode about a point not coinciding with the shear centre, which is the pole of the sectorial area.
 - (ii) The remaining eigenvectors are null ($\lambda_k^2 = 0$) and associated with the axial extension or bending deformation modes – their identification has to be made in Stage 3.
 - (iii) The eigenvector corresponding to deformation mode identified in Stage 2 is normalized as proposed in Silvestre & Camotim (2002) and collected in matrix/vector $[\bar{\mathbf{A}}^2]$.
- (III) **Stage 3.** This stage separates the axial extension and bending global deformation modes not yet identified in Stages 1 and 2. This is achieved by solving the auxiliary eigenvalue problem

$$([\tilde{X}_{ik}^3] - \lambda_k^3 [\tilde{C}_{ik}^3]) \{a_k^3\} = 0 \quad (14)$$

which corresponds to the simultaneous diagonalization of matrices $[\tilde{C}_{ik}^3]$ and $[\tilde{X}_{ik}^3]$. These matrices are obtained from the sub-matrices of $[C_{ik}]$ and $[X_{ik}]$ (i) concerning the (three or two) null eigenvectors of both Eqs. (11) and (12), and (ii) calculated for the associated shape functions¹⁰. Note that Stage 3 does not take place there are if all global deformation modes have been already identified in Stages 1 and 2. The calculation of $[\tilde{C}_{ik}^3]$ and $[\tilde{X}_{ik}^3]$ is done by means of Eqs. (5) and (8), respectively, and the above shape functions are grouped in matrices \mathbf{U}^3 , \mathbf{V}^3 and \mathbf{W}^3 , obtained from

$$\mathbf{U}^3 = \mathbf{U}^{3-1} | \mathbf{U}^{3-2} \quad \mathbf{V}^3 = \mathbf{V}^{3-1} | \mathbf{V}^{3-2} \quad \mathbf{W}^3 = \mathbf{W}^{3-1} | \mathbf{W}^{3-2} \quad (15)$$

with

$$\mathbf{U}^{3-1} = \mathbf{U}^i \tilde{\mathbf{Y}}^1 \quad \mathbf{V}^{3-1} = \mathbf{V}^i \tilde{\mathbf{Y}}^1 \quad \mathbf{W}^{3-1} = \mathbf{W}^i \tilde{\mathbf{Y}}^1 \quad (16)$$

$$\mathbf{U}^{3-2} = \mathbf{U}^i \tilde{\mathbf{Y}}^2 \quad \mathbf{V}^{3-2} = \mathbf{V}^i \tilde{\mathbf{Y}}^2 \quad \mathbf{W}^{3-2} = \mathbf{W}^i \tilde{\mathbf{Y}}^2 \quad (17)$$

where (i) $\tilde{\mathbf{Y}}^1$ and $\tilde{\mathbf{Y}}^2$ are sub-matrices formed by the eigenvectors under consideration and (ii) the columns of matrices \mathbf{U}^i , \mathbf{V}^i and \mathbf{W}^i correspond to the initial shape function components $u_i(s)$, $v_i(s)$ and $w_i(s)$. The solution of the third auxiliary eigenvalue problem provides the following information:

- (i) The null eigenvalue ($\lambda_1^3 = 0$) corresponds to the axial extension deformation mode.
- (ii) The positive eigenvalues ($\lambda_1^3 > 0$) correspond to the bending deformation modes.
- (iii) The eigenvectors corresponding to the two or three deformation modes identified in Stage 3 are normalized as proposed in Silvestre & Camotim (2002) and collected in matrix $[\bar{\mathbf{A}}^3]$.

¹⁰ In the conventional cross-section analysis (no restraints), the sub-matrices of $[C_{ik}]$ and $[D_{ik}]$ always correspond three null eigenvalues of both Eqs. (11) and Eq. (12) (see Silvestre & Camotim 2002, Bebiano *et al.* 2005).

Finally, matrices $[\bar{u}_{ik}]$, $[\bar{v}_{ik}]$ and $[\bar{w}_{ik}]$, containing the various normalize cross-section deformation mode component functions used to determine the modal stiffness matrices \bar{C}_{ik} , \bar{D}_{ik} , \bar{B}_{ik} , \bar{X}_{jik} and \bar{W}_j^0 , are given by

$$[\bar{u}_{ik}] = [u_{ik}][\bar{A}] \quad [\bar{v}_{ik}] = [v_{ik}][\bar{A}] \quad [\bar{w}_{ik}] = [w_{ik}][\bar{A}] \quad (18)$$

with

$$[\bar{A}] = [\bar{A}^1 | \bar{A}^2 | \bar{A}^3] \quad (19)$$

2.1.1 Identification and characterization of the constrained deformation modes

In order to illustrate the procedure described in the previous section, Table 1 shows, for the unrestrained and restrained cross-sections depicted in Figs. 4(a)-(b), the signs of the eigenvalues obtained in Stages 1, 2 and/or 3, and the stages in which the deformation modes are identified. Recall, that,

Table 1: Identification of the deformation modes of unrestrained (**Z0-C0**) and restrained (**Z1-Z3, C1-C3**) zed-section ($Z 102 \times 52 \times 11 \times 2.0$) and lipped channel ($C 102 \times 52 \times 11 \times 2.0$) cross-sections: eigenvalues obtained and deformation modes identified in Stages 1, 2 and 3

		STAGE 1					STAGE 2				STAGE 3		
Unrestrained	K	1	2	3	4	5 to 18	1	2	3	4	1	2	3
Z0	Eigenvalues (λ_k^α)	0	0	0	0	> 0	0	0	0	> 0	0	> 0	> 0
	Identified modes	→ 2				L + D	→ 3		T		AE	B _M	B _m
Restrained	K	1	2	3	4	5 to 18							
Z1	Eigenvalues (λ_k^α)	0	> 0	> 0	> 0	> 0							
	Identified modes	A.E	L-D-G			L + D							
Restrained	K	1	2	3	4	5 to 18	1	2	3				
Z2	Eigenvalues (λ_k^α)	0	0	0	> 0	> 0	0	0	0				
	Identified modes	→ 2			L-D-G	L + D	→ 3				A.E	B _M	B _m
Restrained	K	1	2	3	4	5 to 18	1	2	3				
Z3	Eigenvalues (λ_k^α)	0	0	0	> 0	> 0	0	0	> 0			1	2
	Identified modes	→ 2			L-D-G	L + D	→ 3		T		A.E	B _{M-m}	
Unrestrained	K	1	2	3	4	5 to 18	1	2	3	4	1	2	3
C0	Eigenvalues (λ_k^α)	0	0	0	0	> 0	0	0	0	> 0	0	> 0	> 0
	Identified modes	→ 2				L + D	→ 3		T		A.E	B _M	B _m
Restrained	K	1	2	3	4	5 to 18							
C1	Eigenvalues (λ_k^α)	0	> 0	> 0	> 0	> 0							
	Identified modes	A.E	L-D-G			L + D							
Restrained	K	1	2	3	4	5 to 18	1	2			1	2	
C2	Eigenvalues (λ_k^α)	0	0	> 0	> 0	> 0	0	0			0	> 0	
	Defined modes	→ 2		B _M -T	B _M -T	L + D	→ 3				A.E	B _m	
Restrained	K	1	2	3	4	5 to 18							
C3	Eigenvalues (λ_k^α)	0	> 0	> 0	> 0	> 0							
	Identified modes	A.E	B _M -T	B _m	L-D-G	L + D							

Note:
1) → 2: Requires Stage 2
2) → 3: Requires Stage 3
3) Deformation modes: A.E (axial extension), B_M (major axis bending), B_m (minor axis bending), T (torsion), B_M-T (coupled major axis bending-torsion), L (local), D (distortional), G (global: B_M + B_m + T) and L-D-G (coupled local-distortional-global)

whenever some of the first four eigenvalues obtained in Stage 1 are positive, the identification of the corresponding deformation mode natures requires performance of cross-section rotation analyses (up to a maximum of three). Figures 5 (zed-section) and 6 (lipped channel) (i) show the in-plane shapes of the first eight deformation modes and (ii) provide the corresponding \bar{C}_{kk} , \bar{D}_{kk} and \bar{B}_{kk} (diagonal) matrix components. The observation of the results displayed in Table 1 and Figs. 5 and 6 leads to the following remarks:

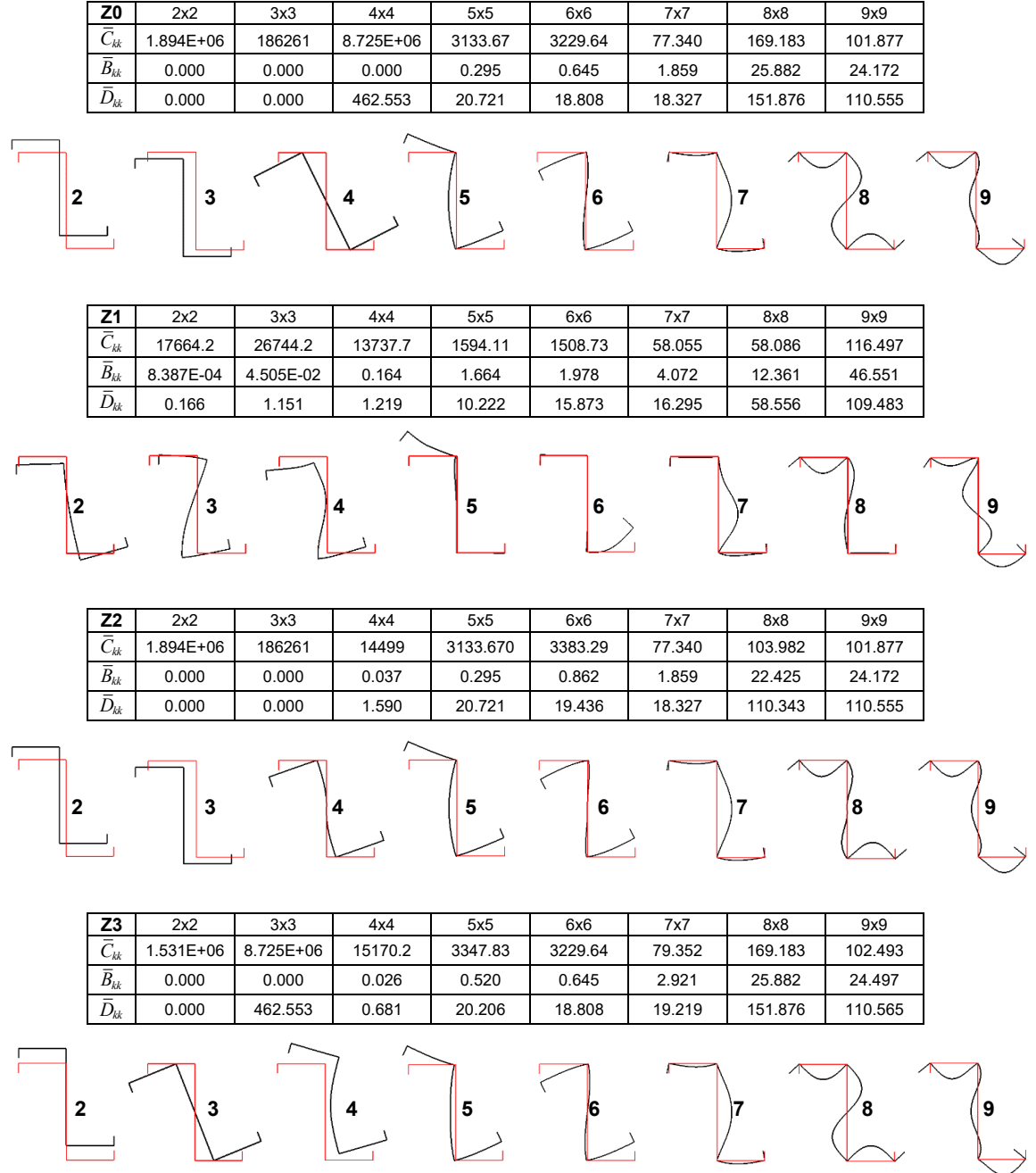


Figure 5: Z102 × 52 × 11 × 2.0: 8 most relevant deformation modes and their components \bar{C}_{kk} , \bar{B}_{kk} and \bar{D}_{kk} for unrestrained (**Z0**) and restrained (**Z1-Z3**) cross-sections – dimensions in *cm*, Young and shear moduli in *kN/cm²*.

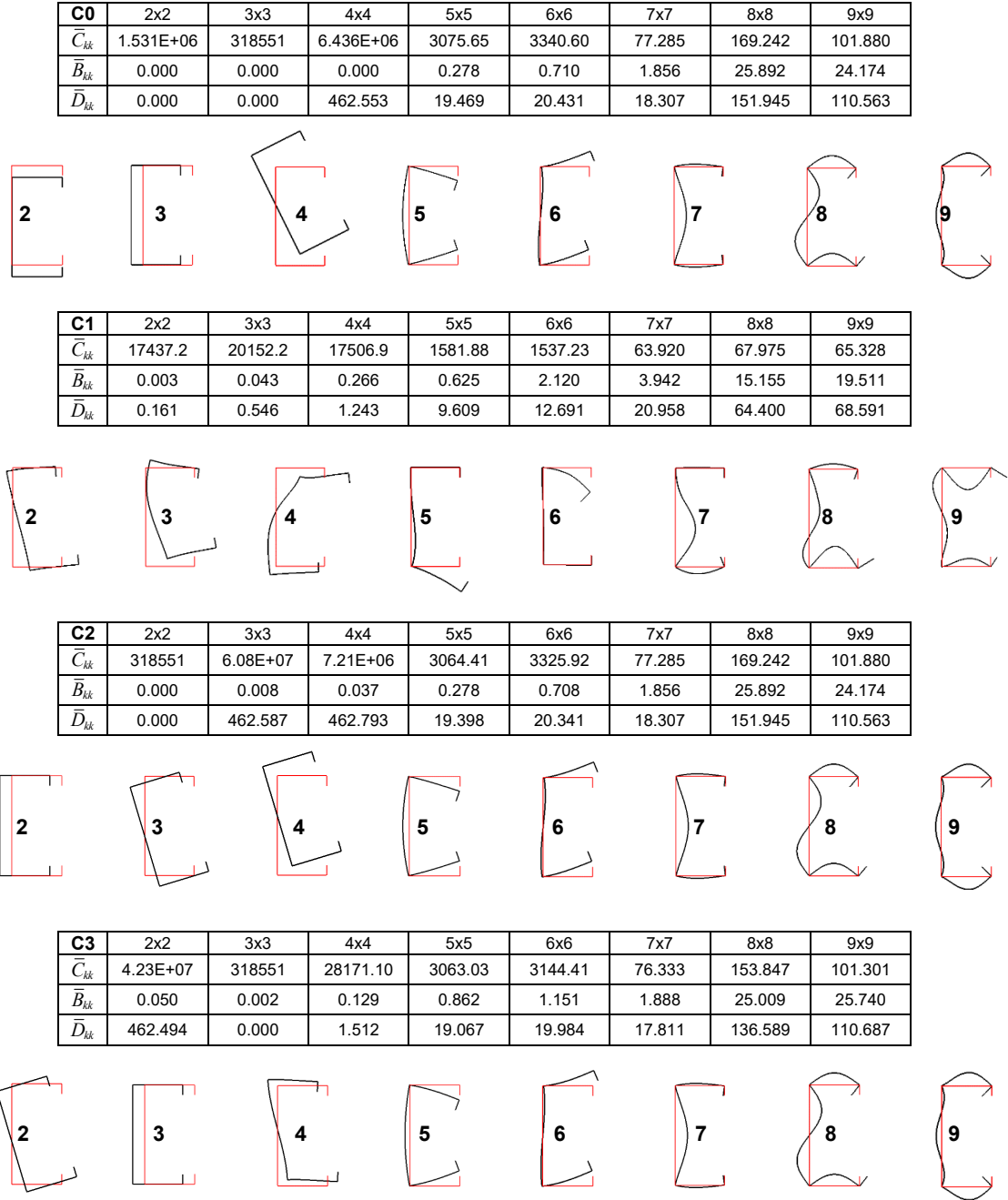


Figure 6: C 102 × 52 × 11 × 2.0: 8 most relevant deformation modes and their components \bar{C}_{kk} , \bar{B}_{kk} and \bar{D}_{kk} for unrestrained (**C0**) and restrained (**C1-C3**) cross-sections – dimensions in *cm*, Young and shear moduli in *kN/cm²*.

- (i) In the constrained cross-sections **Z1** and **C1**, all deformation modes are identified in Stage 1. On the other hand, in the unrestrained (**Z0** and **C0** – obviously) and restrained (**Z2**, **Z3** and **C2**) cross-sections, the three stages are required to identify all the deformation modes.
- (ii) Stage 2 is required for the restrained cross-sections **Z2**, **Z3** and **C2**. Only in the case of cross-section **Z3** is a torsion mode not involving spring deformation identified at this stage.

- (iii) The \bar{B}_{kk} values concerning the constrained rigid-body deformation modes are either null (like in their unconstrained counterparts) or positive, depending on whether they involve or not spring deformations. For instance, (iii₁) \bar{B}_{33} and \bar{B}_{44} of cross-section **C2** and (iii₁) \bar{B}_{22} and \bar{B}_{33} of cross-section **C3** stem from the elastic strain energy stored in the translational springs.
- (iv) It is possible to assess very clearly the influence of the constraints on the deformation mode shapes and corresponding mechanical properties. Indeed, one observes that:
 - (iv.1) In cross-section **Z3**, restraining bending about the centroidal axis normal to the web leads to a single bending mode (mode **2**), about the centroidal axis normal to the flanges, which corresponds to skew bending (B_{M+m}) – the value of \bar{C}_{22} / E is the cross-section moment of inertia about this same axis.
 - (iv.2) In cross-section **C2**, restraining torsion about the shear centre leads to two deformation modes combining major-axis bending (B_M) and torsion (T) – modes **3** and **4**. Each of these two B_M - T modes is expressed as a torsion mode about a point not coinciding with the shear centre – its \bar{C}_{kk} / E and \bar{D}_{kk} / G values are the warping constant calculated with the rotation centre as the pole of the sectorial area and the St. Venant torsion constant (obviously, identical for both B_M - T modes).
 - (iv.3) In cross-section **C3**, restraining torsion about the shear centre leads to one B_M - T deformation mode (mode **2**), similar to those addressed in the previous item – the other deformation mode involving B_M and T deformations also involves local and distortional deformations (mode **4**).
 - (iv.4) In cross-sections **C2** and **C3**, the minor-axis bending deformation mode (B_m) corresponds to mode **2** and mode **3**, respectively. This is because this deformation mode is identified in Stage 3, in the former case, and in Stage 1, in the latter case.
- (v) Cross-sections having constraints that restrain partially torsion and/or bending often exhibit deformation modes that combine global deformations with distortional and/or local ones. This is the case of modes **2**, **3** and **4** of cross-sections **Z1** and **C1**, and mode **4** of cross-sections **Z2**, **Z3** and **C3** (mode **4**).
- (vi) The constrained deformation modes provide much more meaningful information about the mechanical behavior of a restrained member than the conventional/unconstrained ones (before carrying out its structural analysis). Moreover, in general, less constrained deformation modes are necessary to obtain an accurate assessment of the restrained member structural behavior.

2.2 Member Analysis

After having performed the cross-section analysis, it is possible to cast the member GBT system of adjacent equilibrium equations in modal form as

$$\bar{C}_{ik} \bar{\varphi}_{k,xxxx} - \bar{D}_{ik} \bar{\varphi}_{k,xx} + \bar{B}_{ik} \bar{\varphi}_k - \lambda \bar{X}_{jik} \left(\bar{W}_j^0 \bar{\varphi}_{k,x} \right)_{,x} = 0 \quad (20)$$

Together with the appropriate end support conditions, this equation system defines the member buckling eigenvalue problem that it is necessary to solve. Note that \bar{C}_{ik} , \bar{D}_{ik} and \bar{B}_{ik} are the modal mechanical properties of the restrained cross-section – while \bar{C}_{ik} and \bar{D}_{ik} are related to the warping displacements and torsional rotations, \bar{B}_{ik} concern the cross-section in-plane deformation (transverse bending of the walls) and the elastic spring stiffness values. On the other hand, \bar{X}_{jik} are geometric stiffness components associated with the uniform normal stress resultants \bar{W}_j^0 – axial force, bending moments or bi-moment.

The methods commonly employed to solve the member GBT eigenvalue problem are standard in structural analysis: Galerkin's method and beam finite element models (Hermite cubic polynomials adopted for the longitudinal discretization) (e.g., Bebiano *et al.* 2010) – the latter are essential in members without standard end support conditions. At this stage, it is worth mentioning that all the GBT buckling results presented in this paper concern simply supported members (end cross-sections locally/globally pinned and free to warp)¹¹ and, therefore, obtained through the application of Galerkin's method, with sinusoidal approximation functions

$$\bar{\varphi}_k(x) = d_k \sin\left(\frac{\eta\pi x}{L}\right) \quad (21)$$

where d_k is the amplitude of deformation mode k (the problem unknown) and η is the number of longitudinal half-waves exhibited by this deformation mode.

Concerning the determination of the modal participation diagrams presented in the next section, it should be mentioned that the participation factor of deformation mode k to a member buckling mode is obtained as the ratio between (i) the strain energy associated with the contribution of this deformation mode and (ii) the sum of such strain energies associated with all the deformation modes participating in the buckling mode – this is the approach adopted in the program GBTUL (Bebiano *et al.* 2010). In previous works (e.g., Camotim *et al.* 2010), the participation factor of deformation mode k was the ratio between (i) the area under the $|\bar{\varphi}_k(x)|$ plot and (ii) the sum of the areas under such plots concerning all the deformation modes participating in the buckling mode.

3. Numerical Results

In order to validate and illustrate the application and capabilities of the proposed GBT cross-section analysis (constrained deformation modes), numerical results concerning the elastic buckling behavior of cold-formed steel ($E=205GPa$ and $\nu=0.3$) (i) purlins restrained by sheeting and (ii) studs braced by sheathing are presented and discussed next. The validation of the GBT-based buckling results (critical buckling loadings and mode shapes) is made through the comparison with values yielded by the programs CUFSM (Li & Schafer 2010) and GBTUL (Bebiano *et al.* 2010), and obtained through ANSYS SFEA (SAS 2013). In the last case, (i) the members are discretized by means of refined meshes of SHELL181 elements (isoparametric 4-node shell elements), employed with the “full integration” option, and (ii) the sheeting and sheathing restraints are modeled by means of elastic translational and rotational COMBIN39 spring 2-node elements. Fig. 4(a) shows the member cross-sections and GBT discretizations considered in these numerical illustrative examples.

3.1 Buckling Behavior of Continuously Restrained Simply Supported Purlins

The first illustrative example concerns the buckling behavior of simply supported purlins with a Z 200×75×25×2.5 cross-section, connected to sheeting and subjected to wind uplift loading – see Fig. 7(a). The pre-buckling (normal) stresses considered in all the purlins analyzed (GBT, FSM and SFEA) are those caused by uniform bending moments about the centroidal axis perpendicular to the web. Fig. 7(b) shows the ensuing normal stress cross-section distribution: the upper (connected)

¹¹ The extension to members with other standard support conditions (e.g., fixed-ended members) is straightforward – it is just necessary to apply Galerkin's method with the appropriate approximation functions. On the other hand, more complex support conditions require the use of beam finite element models – although no conceptual difficulties arise, it is no longer possible to derive analytical or semi-analytical formulae to determine buckling loads or moments.

and bottom (free) flanges are under uniform tensile and compressive stresses, respectively – this type of loading is often found in purlins restrained by sheeting placed parallel to the flanges.

It should be noted that, in practice, the wind uplift loading is applied at the purlin top flange mid-width region, as shown in Fig. 7(a). The authors are also aware that the load point of application plays a relevant role in the response of purlins subjected to wind uplift. Its effects must be included in more realistic models, which account for the pre-buckling states due to non-uniform bending and/or torsion combined with lateral-distortional deformation (see Fig. 7(c)) – such pre-buckling states involve longitudinal normal (σ_{xx}^0), transverse normal (σ_{ss}^0) and shear (τ_{xs}^0) stress distributions¹². Since routine design approaches require simple procedures, the current North American specification (AISI 2016) includes a DSM-based design methodology for purlin-sheeting systems that involves performing elastic buckling analyses of restrained purlins subjected to the longitudinal pre-buckling stress distribution considered in this work (see Fig. 7(b)). The effects stemming from non-uniform bending and initial torsion are included in the design approach by means of moment gradient (C_b) and reduction (R) factors, respectively.

In this work, the modeling of the restraint provided by the sheeting to the purlins comprises continuous translational (K_{TG}) and rotational (K_R) springs, which restrain the (i) horizontal/lateral displacements (diaphragm restraints) and (ii) upper flange rotations about the x -axis. Many purlin-sheeting system models adopted in the past assume that the sheeting completely restrains the lateral displacement at the upper flange-web junction (*e.g.*, Gao & Moen 2014, Ren *et al.* 2016, Ings & Trahair 1984, Soroushian & Peköz 1982). Others, such as those employed in Lucas *et al.* (1997) and Lendvai *et al.* (2018), do not adopt the above assumption and determine, either experimentally or numerically, the lateral/diaphragm stiffness for each individual case. Furthermore, the rotational springs are assumed to be located at either (i) the intersection of the upper flange and web (*i.e.*, at the cross-section rotation centre when through-fastened to the sheeting under wind uplift loading – see Fig. 5(c), *e.g.*, Gao & Moen 2014, Yuan *et al.* 2014), or (ii) the upper flange mid-point (where the sheeting is screw-connected, *e.g.*, Ren *et al.* 2016, Basaglia *et al.* 2013, Lucas *et al.* 1997) – the latter assumption is adopted in this illustrative example (see Fig. 7(d)¹³).

For comparison purposes, Figs. 8 and 9 show, respectively, (i) the first 10 (conventional) deformation modes of the unrestrained Z-section (termed **P0**), yielded by code GBTUL, and (ii) the constrained deformation modes **2-10** (mode **1** is axial extension) or four restrained cross-sections exhibiting continuous translational and rotational springs with null or infinite stiffness (*i.e.*, K_{TG} and K_R equal to 0 or ∞) – cross-sections **P1** ($K_{TG}=\infty$, $K_R=0$), **P2** ($K_{TG}=0$, $K_R=\infty$), **P3** ($K_{TG}=\infty$, $K_R=\infty$) and **P4** ($K_{TG}=\infty$, $K_R=1.285 \text{ kNm/cm/rad}$) – the **P4** stiffness values were reported by Gao and Moen (2012), using a typical metal sheeting and standard fastener locations. Table 2 shows the components of the $[\bar{C}_{ik}]$ (diagonal), $[\bar{B}_{ik}]$ (diagonal) and $[\bar{D}_{ik}]$ (almost diagonal) stiffness matrices concerning deformations modes **2-10** of the unrestrained cross-section **P0** and the restrained cross-sections **P1** and **P4**, which exhibit the constraints adopted in Ings & Trahair (1984), Zhu *et al.* (2017) and Gao & Moen (2012), respectively. The observation of the results presented in these two figures and table prompts the following remarks:

¹² Concerning the GBT-based buckling analysis of beams with conventional deformation modes and subjected to transverse loadings applied away from the cross-section shear centre, it is worth noting the recent work by Bebianio *et al.* (2018).

¹³ Using a GBT cross-section discretisation involving a very small wall segment adjacent to the upper flange-web junction, it would be possible to have a rotational spring very close to cross-section rotation centre when through-fastened to sheeting.

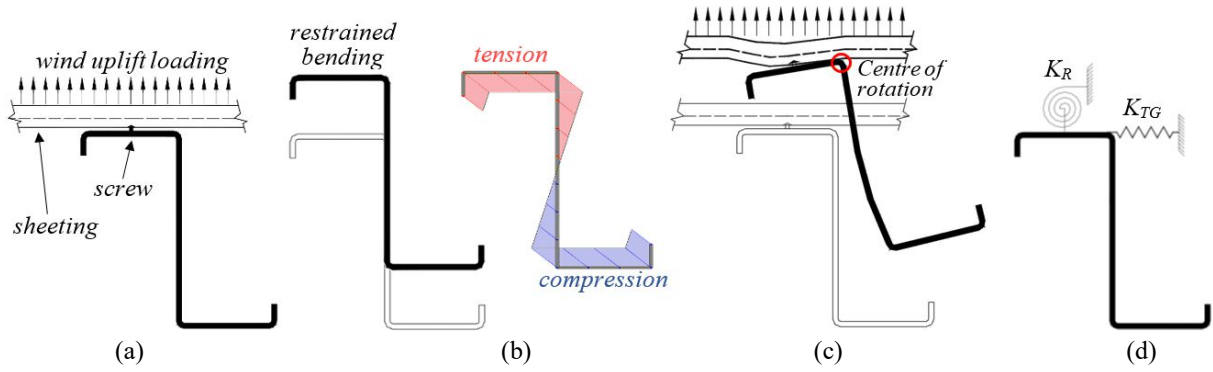


Figure 7: (a) Purlin-sheeting system under wind uplift loading, (b) pre-buckling longitudinal normal stresses, (c) lateral-distortional deformation and restrained purlin rotation centre, and (d) spring model restraining the purlin

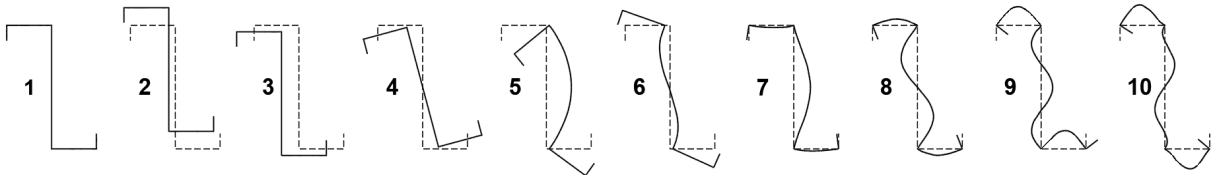


Figure 8: First 10 (conventional) deformation modes of the unrestrained (**P0**) purlin (yielded by GBTUL)

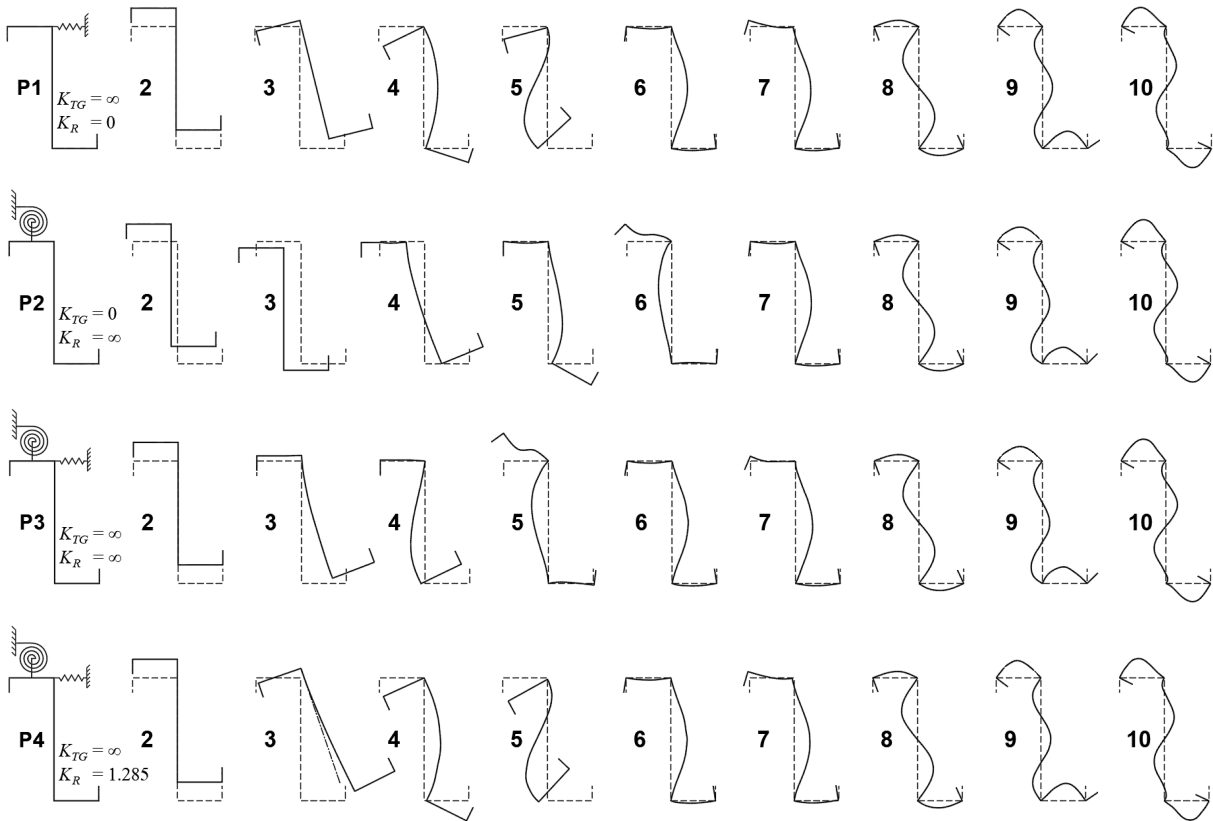


Figure 9: Constrained deformation modes 2-10 of the restrained purlins **P1**, **P2**, **P3**, and **P4**

Table 2: Components of stiffness matrices \bar{C}_{kk} , \bar{B}_{kk} and \bar{D}_{ik} concerning modes **2-10** for the unrestrained cross-section **P0** and the restrained cross-sections **P1** and **P4** – dimensions in *cm*, Young's and shear moduli in *kN/cm²*

$\bar{C}_{kk} \times 10^3$									P0								
									13934.6	1033.34	177747	9.30641	9.82262	0.28312	0.33175	0.18151	0.13908
P1									P4								
12385.9	291145	5.57659	6.58592	0.29231	7.65976	0.33178	0.18149	0.13908	12385.9	22.5030	6.74406	8.03015	0.29243	7.57781	0.33180	0.18084	0.13914
$\bar{B}_{kk} \times 10^{-2}$									P0								
									0.000	0.000	0.000	3.1044	7.7454	51.3104	472.591	634.075	613.563
P1									P4								
0.000	0.000	1.366	4.461	52.424	1727.950	472.642	634.033	613.545	0.000	0.017	2.211	5.772	52.454	1710.110	472.707	631.903	614.273
\bar{D}_{ik}									P0								
									0.0000	0.0000	0.0000	0.0000	0.0000	2.7766	0.0000	-11.5165	0.0000
									0.0000	0.0000	0.0000	-1.2154	0.0000	0.6322	0.0000	-1.1716	0.0000
									0.0000	0.0000	1601.51	0.0000	-51.3251	0.0000	56.1999	0.0000	-69.156
									0.0000	-1.2154	0.0000	7.0670	0.0000	-4.0450	0.0000	-3.9865	0.0000
									0.0000	0.0000	-51.3251	0.0000	6.3587	0.0000	2.1591	0.0000	7.1317
									2.7766	0.6322	0.0000	-4.0450	0.0000	16.5730	0.0000	-6.3886	0.0000
									0.0000	0.0000	56.1999	0.0000	2.1591	0.0000	78.9222	0.0000	-17.355
									-11.5165	-1.1716	0.0000	-3.9865	0.0000	-6.3886	0.0000	88.9156	0.0000
									0.0000	0.0000	-69.156	0.0000	7.1317	0.0000	-17.355	0.0000	71.6807
P1									P4								
0.0000	0.0000	0.2697	0.1111	-2.3539	2.9291	0.0000	10.3940	0.0000	0.0000	0.0000	0.3112	-0.0738	2.3545	-2.9321	0.0000	-10.3741	0.0149
0.0000	1601.51	-16.006	36.2946	-8.0981	-8.7523	-56.199	15.476	-69.133	0.0000	0.1127	0.0000	-0.3515	-0.0158	0.0953	-0.5087	-0.2205	-0.5453
0.2697	-16.0060	2.9844	0.7099	2.6575	-0.9751	-0.0959	2.6242	0.7989	0.3112	0.0000	3.8589	-0.9018	-3.0642	1.3820	0.1195	-3.0404	0.1658
0.1111	36.2946	0.7099	4.0834	1.0560	-2.0935	1.5339	1.0412	-5.3497	-0.0738	-0.3515	-0.9018	4.7082	0.6826	-2.1062	-1.6922	0.6623	6.0409
-2.3539	-8.0981	2.6575	1.0560	16.3931	-17.595	-0.0821	-6.2652	0.0940	2.3545	-0.0158	-3.0642	0.6826	16.3945	-17.5937	0.0843	-6.2560	-0.0855
2.9291	-8.7523	-0.9751	-2.0935	-17.595	20.7958	-2.0320	8.7469	2.0169	-2.9321	0.0953	1.3820	-2.1062	-17.5937	20.7831	2.0237	8.7699	-2.0804
0.0000	-56.1996	-0.0959	1.5339	-0.0821	-2.0320	78.9252	0.0000	17.3570	0.0000	-0.5087	0.1195	-1.6922	0.0843	2.0237	78.9416	0.0259	17.3708
10.3940	15.4765	2.6242	1.0412	-6.2652	8.7469	0.0000	88.9102	0.0000	-10.3741	-0.2205	-3.0404	0.6623	-6.2560	8.7699	0.0259	88.5652	0.0386
0.0000	-69.1339	0.7989	-5.3497	0.0940	2.0169	17.3570	0.0000	71.6788	0.0149	-0.5453	0.1658	6.0409	-0.0855	-2.0804	17.3708	0.0386	71.6807

- (i) Purlins **P3** and **P4** exhibit only one (skew) bending deformation mode, and no torsion deformation mode. Instead, they both exhibit a lateral-distortional deformation mode (mode **3**), which involves web transverse bending and is thus associated with $\bar{B}_{33} \neq 0$. In purlin **P4**, this deformation mode involves also bending and torsional deformations – due to the rigid horizontal restraint, they do not appear in purlin **P3**.
- (ii) Deformation mode **3** of purlin **P1** combines torsion and bending about the centroidal axis parallel to the web – the equivalent torsion mode has its rotation located at the top flange.
- (iii) The presence of the restraints makes matrix \bar{D}_{ik} “less diagonal” – indeed, matrix \bar{D}_{ik} is almost diagonal for the unrestrained purlin **P0** and nearly fully populated for the restrained purlins **P1** and **P4**.
- (iv) While all the restraints considered do not constrain the local deformation modes **8**, **9** and **10**, only in purlin **P2** are the major and minor-axis bending deformation modes not constrained.

Using a single half-wave sinusoidal function ($\eta=1$ in Eq. (23)) to approximate the mode amplitude functions $\bar{\varphi}_k(x)$ and performing buckling analyses for a wide range of lengths (L) leads to the purlin signature curves shown in Figure 10(a), providing the variation of the critical buckling moment M_{cr} with the beam length L (logarithmic scale), concerning the unrestrained (**P0** – dashed curve) and restrained (**P1** to **P4** – solid curves) purlins – the local minimum points of the signature curves correspond to critical moments associated with either local, distortional or lateral-distortional buckling (no local minimum exists associated with global buckling). Besides the results obtained by means of the constrained-mode GBT analyses (solid curves), Figs. 10(a) also displays critical buckling mode shapes yielded by the program CUFSM and, for validation and comparison purposes, buckling

moment values determined with the programs GBTUL (circles) and CUFSM (symbol \times). In order to assess the influence of the distortional deformations on the critical buckling moments, Fig. 10(b) shows the M_{cr} vs. L curves yielded by the program GBTUL concerning buckling analyses including either all conventional modes (L+D+G) or only the local and global ones (L+G) modes – the critical buckling mode shapes yielded by the latter analyses are also displayed. Figs. 11(a)-(b) provide modal participation diagrams, based on both the conventional and constrained deformation modes, concerning purlins **P1** to **P4**. Also shown are the buckled mid-span cross-sections associated with purlin lengths corresponding to either local minima of the signature curves or $L=424\text{ cm}$ (when no such minimum exists), obtained as combinations of the conventional (left side) and constrained (right side) deformation modes shown in Figs. 8 and 9, respectively. The observation of the buckling results presented in Figs. 10(a)-(b) and 11(a)-(b) prompts the following remarks:

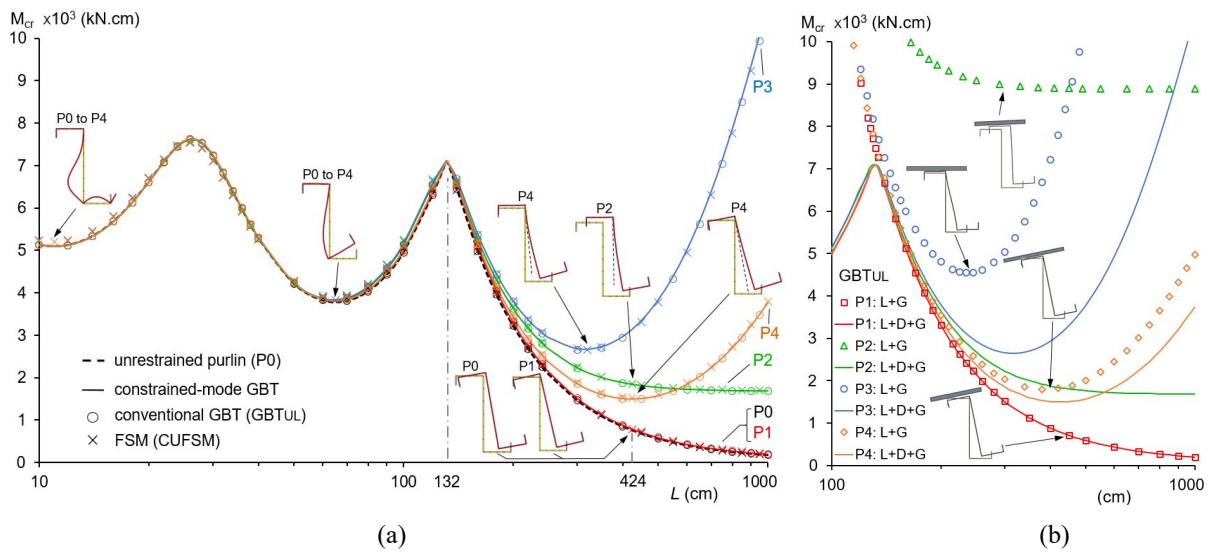


Figure 10: (a) Signature curves M_{cr} vs. L and critical buckling mode shapes of purlins **P0-P4**, and (b) buckling results yielded by GBTUL analyses including all conventional modes (L+D+G) and only local and global ones (L+G)

- (i) First of all, the buckling moments yielded by the FSM and the two GBT buckling analyses (including all deformation modes) virtually coincide – all differences are below 2.4%. Moreover, there is also an extremely close agreement between the buckling mode shapes obtained from the three analyses.
- (ii) For $L \leq 132\text{ cm}$, the buckling behavior is independent of the restraint conditions considered in this work (the solid and dashed curves virtually coincide). This is because the critical buckling modes combine local ($L=11\text{ cm}$) and/or distortional ($L=64 \pm 1\text{ cm}$) deformations that do not involve upper flange horizontal displacements or rotations and, therefore, are not affected by the restraints – see the buckled mid-span cross-sections.
- (iii) The purlins with the top flange restrained against rotation ($K_R \neq 0$) and $L > 132\text{ cm}$ clearly exhibit lateral-distortional buckling, an instability phenomenon investigated by several researchers (e.g., Gao & Moen 2012,2014, Basaglia *et al.* 2013, Soroushian & Peköz 1982).
- (iv) The unrestrained purlins ($K_R=K_{TG}=0$ – **P0**) and the purling with only top flange horizontal displacement restraint ($K_R=0$ and $K_{TG}=\infty$ – **P1**) have nearly coincident signature curve descending branches, associated with flexural-torsional buckling exhibiting steep slopes, a feature previously reported by other authors (e.g., Basaglia *et al.* 2013, Yuan *et al.* 2014). This is because, as shown

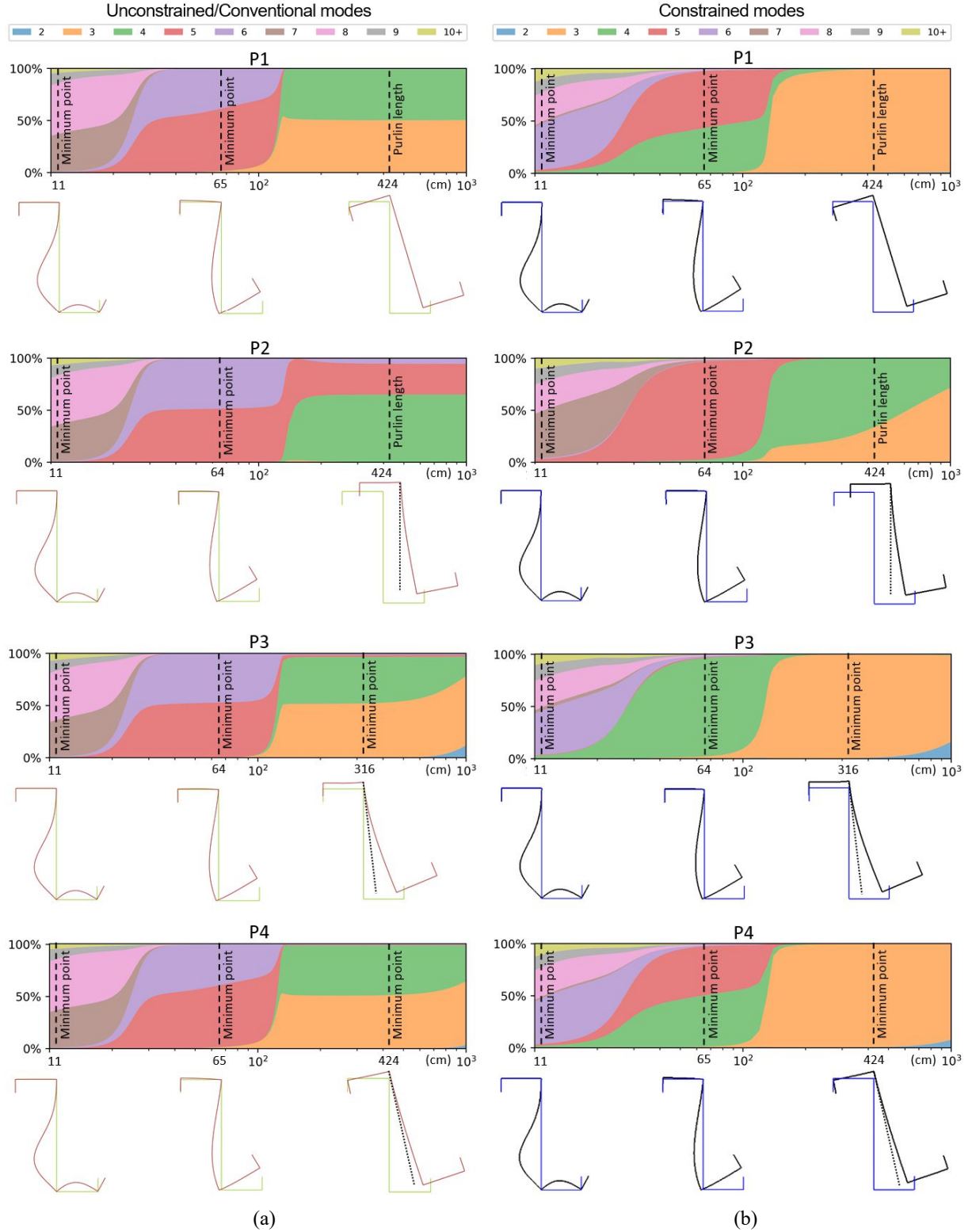


Figure 11: Modal participation diagrams and buckled mid-span cross-sections concerning purlins **P1-P4** obtained on the basis of (a) unconstrained and (b) constrained GBT deformation modes

by Basaglia *et al.* (2013), the unrestrained purlin buckling modes exhibit only a tiny horizontal displacement of the point where the lateral/horizontal restraint is located – see the **P0** purlin buckled mid-span cross-section showed in Figure 10(a).

- (v) By looking at the modal participation diagrams displayed in Figs. 11(a)-(b), it can be readily concluded that the constrained deformed modes are much efficient in assessing the purlin buckling behavior than their unconstrained/conventional counterparts. Indeed, it is possible to obtain accurate purlin buckling results by including in the GBT buckling analyses just one or two constrained deformation modes, regardless of whether buckling occurs in distortional, lateral-distortional or lateral-torsional modes. This feature plays a pivotal role in the development of semi-analytical buckling formulae, which is addressed ahead in the paper (see Section 4).
- (vi) It may be argued that using conventional cross-section deformation modes in the GBT buckling analysis of purlins restrained by sheeting somewhat “clouds” the structural interpretation of the results obtained. This assertion can be clearly attested by comparing the pairs of modal participation diagrams concerning purlins **P2**, **P3**, **P4** buckling in lateral-distortional modes. Indeed, these critical buckling modes combine contributions (vi₁) from just one (mode **3** in purlins **P3** and **P4**) or two (modes **3** and **4** in purlins **P2**) constrained modes, and (vi₂) from four (modes **3**, **4**, **5** and **6** in purlins **P2**, **P3** and **P4**) unconstrained modes. Although the contributions from modes **5** and **6** are always small, neglecting them leads to a highly significant loss of accuracy in the critical lateral-distortional buckling moments obtained – for instance, the errors can reach 400%, 68% and 19 %, respectively for purlins **P2**, **P3** and **P4** (see Fig. 10(b)).

Since members subjected to bending may buckle in modes exhibiting several longitudinal half-waves ($\eta > 1$), it should be noted that the curves shown in Figs. 10(a)-(b) may not provide the real purlin buckling behavior for some length ranges. For illustrative purposes, Fig. 12 shows the variation of the critical buckling moment M_{cr} and mode shape with the length L – the buckling mode half-wave numbers are given inside brackets. Besides the GBT-based results (solid and dashed curves) using $\eta > 1$ in Eq. (23), the figure also display, for validation and comparison purposes, critical buckling moments and 3D mode shapes obtained from ANSYS SFEA (SAS 2013). The analysis of the GBT and ANSYS buckling results presented leads to the following remarks:

- (i) The GBT and ANSYS M_{cr} values practically coincide, as the differences never exceed 3.1%. In addition, there is also very close agreement between the buckling mode shapes provided by both analyses.
- (ii) For $L \leq 185 \text{ cm}$, the buckling behavior is independent from the restraint conditions considered in this work, since the buckling curves are almost identical – recall that, for buckling analyses involving single half-wave buckling modes, this length limit was 132 cm (see Fig. 10(a)).
- (iii) For $L \leq 41 \text{ cm}$, all purlins buckle in local modes exhibiting half-wave numbers that increase with the length. For $L > 41 \text{ cm}$, buckling occurs in distortional modes exhibiting 1 to 3 half-waves – this buckling behavior occurs for purlins with lengths comprised between $L = 185 \text{ cm}$ (purlins **P0** and **P1**) and $L = 198 \text{ cm}$ (purlins **P3**) – for purlins **P2** and **P4**, the transition takes place for intermediate length values.
- (iv) For purlins longer than the values mentioned in the previous item, the curves M_{cr} vs. L correspond to two possible critical buckling mode natures: (iv₁) lateral-torsional buckling, for purlins **P0** (unrestrained) and **P1** (restrained) and (iv₂) lateral-distortional buckling, for the restrained purlins **P2**, **P3** and **P4** – while the former is single half-wave, the latter exhibit half-wave numbers ranging from 1 to 3.

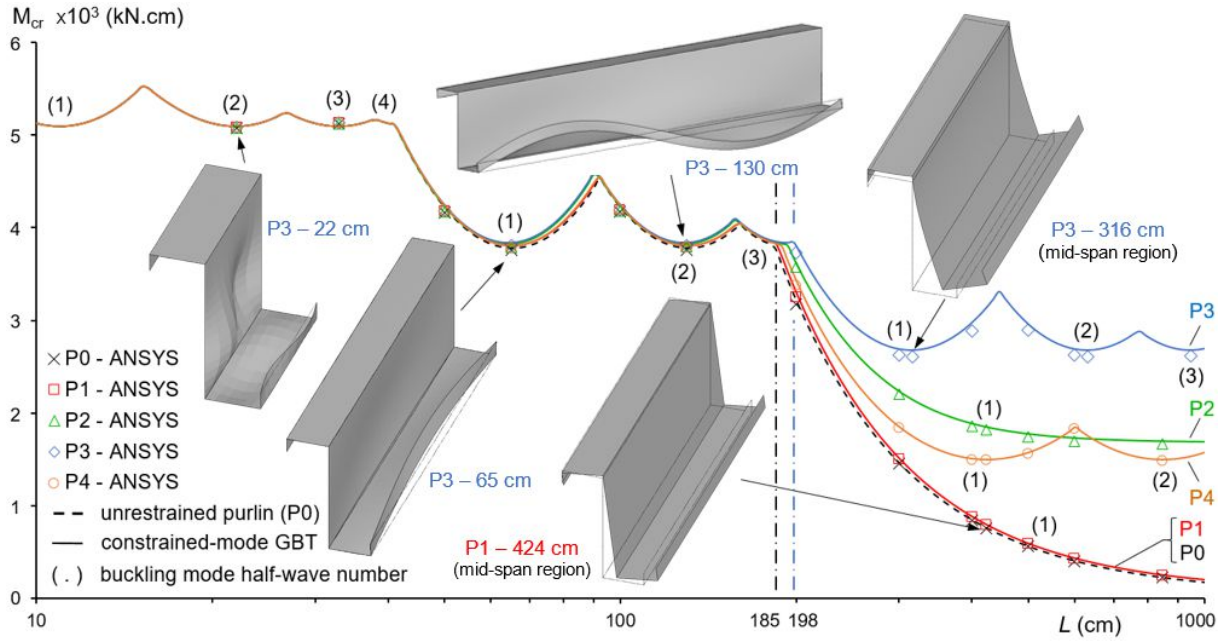


Figure 12: Variation of the critical buckling moment and mode shape with the purlin length

Finally, for a few purlins buckling in distortional, lateral-distortional or lateral-torsional modes, Tables 3 to 5 provide the critical buckling moments obtained by means of GBT analyses including all deformation modes and also either only the dominant (“constrained GBT”) or the two most relevant (GBTUL or “constrained GBT”) ones – the values yielded by ANSYS SFEA are also presented. The comparison between the various sets of critical buckling moments leads to the following conclusions:

- For purlins buckling in distortional modes (*i.e.*, purlins **P1** and **P4** with $L=50\text{ cm}$ and 100 cm), the GBT analyses including the two most relevant modes lead to average errors of 4.0%, using constrained modes **4** and **5**, and 5.1%, using conventional modes **5** and **6**.
- For purlins buckling in lateral-distortional modes (*i.e.*, purlins with **P3** or **P4** with $L \geq 200\text{ cm}$), GBT analyses with constrained deformation modes provide accurate buckling results with only deformation mode **3** – errors below 4.1%. On the other hand, the GBTUL analyses must include more than two conventional deformation modes to provide accurate buckling results – considering only the two most relevant modes (modes **3** and **4**) leads to errors that may reach 1756%, for purlins **P3** (fully restrained), and 31%, for purlins **P4** (partially restrained).

Table 3: GBT and ANSYS buckling results for purlins **P1**

L (cm)	ANSYS		Conventional Modes (GBTUL)							Constrained Modes (C-GBT)						
	$M_{cr,ANSYS}$ (kN.cm)	Half Wave	All Modes				Two Modes			All Modes				One/Two Modes		
			$M_{cr,GBTUL}$ (kN.cm)	Modal Participations			$M_{cr,GBTUL}$ (kN.cm)	Modes		$M_{cr,C-GBT}$ (kN.cm)	Modal Participations			$M_{cr,C-GBT}$ (kN.cm)	Mode(s)	
				5	6	Others		5	6		5	4	Others		4	5
50	4178.00	1	4238.59	56.1%	43.2%	0.7%	4395.98	50.0%	50.0%	4237.95	55.5%	39.3%	5.2%	4349.04	41.4%	58.6%
100	4186.10	2	4238.59	56.1%	43.2%	0.7%	4395.98	50.0%	50.0%	4237.98	55.5%	39.3%	5.2%	4349.60	41.4%	58.6%
200	3247.70	1	3301.20	50.6%	49.4%	0.001%	3317.40	50.0%	50.0%	3301.42	94.5%		5.5%	3335.78	100%	
300	1499.10	1	1511.91	50.3%	49.7%	0.001%	1514.44	50.0%	50.0%	1511.98	97.8%		2.2%	1522.99	100%	
400	877.60	1	882.53	50.2%	49.8%	0.001%	883.41	50.0%	50.0%	882.56	98.6%		1.4%	888.51	100%	
500	588.31	1	590.82	50.2%	49.8%	0.001%	591.33	50.0%	50.0%	590.85	98.8%		1.2%	594.84	100%	
600	430.73	1	432.28	50.2%	49.8%	0.001%	432.67	50.0%	50.0%	432.30	98.9%		1.1%	435.31	100%	

Table 4: GBT and ANSYS buckling results for purlins **P3**

L (cm)	ANSYS		Conventional Modes (GBTUL)										Constrained Modes (C-GBT)									
			All Modes					Two Modes					All Modes					One/Two Modes				
	M _{cr,GBTUL} (kN.cm)	Modal Participations			GBTUL ANSYS	M _{cr,GBTUL} (kN.cm)	Modes		GBTUL ANSYS	M _{cr,C-GBT} (kN.cm)	Modal Participations			C-GBT ANSYS	M _{cr,C-GBT} (kN.cm)	Mode(s)		C-GBT ANSYS				
		5	6	Others			5	6			4	6	Others			4						
50	4181.80	1	4242.06	52.1%	47.7%	0.2%	1.4%	4575.72	50.0%	50.0%	9.4%	4243.16	91.5%	2.5%	6.0%	1.5%	4358.54	100%	4	4.2%		
100	4189.80	2	4242.06	52.1%	47.7%	0.2%	1.2%	4575.72	50.0%	50.0%	9.2%	4243.20	91.5%	2.5%	6.0%	1.3%	4359.10	100%	4	4.0%		
200	3726.30	1	3790.71	53.1%	46.5%	0.4%	1.7%	49456.94	50.0%	50.0%	1227.2%	3803.91	98.4%		Others 1.6%	2.1%	3823.10	100%	3	2.6%		
300	2622.90	1	2663.68	53.4%	46.2%	0.4%	1.6%	48705.34	50.0%	50.0%	1756.9%	2685.85	99.2%		Others 0.8%	2.4%	2697.57	100%	3	2.8%		
400	2884.60	1	2939.32	54.1%	45.5%	0.4%	1.9%	49439.38	50.0%	50.0%	1613.9%	2974.02	98.9%		Others 1.1%	3.1%	3002.44	100%	3	4.1%		
500	2894.30	2	2933.73	53.2%	46.4%	0.4%	1.4%	48688.94	50.0%	50.0%	1582.2%	2950.99	99.1%		Others 0.9%	2.0%	2962.39	100%	3	2.4%		
600	2625.70	2	2663.68	53.4%	46.2%	0.4%	1.4%	48705.34	50.0%	50.0%	1754.9%	2685.87	99.2%		Others 0.8%	2.3%	2697.85	100%	3	2.7%		

Table 5: GBT and ANSYS buckling results for purlins **P4**

L (cm)	ANSYS			Conventional Modes (GBTUL)										Constrained Modes (C-GBT)									
				All Modes					Two Modes					All Modes					One/Two Modes				
	M _{cr,GBTUL} (kN.cm)	Modal Participations			GBTUL ANSYS	M _{cr,GBTUL} (kN.cm)	Modes		GBTUL ANSYS	M _{cr,C-GBT} (kN.cm)	Modal Participations			C-GBT ANSYS	M _{cr,C-GBT} (kN.cm)	Mode(s)		C-GBT ANSYS					
50	4178.20	1		4238.76	5	6	Others	1.4%	4396.60	5	6	5.2%	4239.23	4	5	Others	1.5%	4349.61	4	5	4.1%		
					56.0%	43.3%	0.7%			50.0%	50.0%			46.0%	48.1%	5.9%			48.8%	51.2%			
100	4186.30	2		4238.76	5	6	Others	1.3%	4396.60	5	6	5.0%	4239.27	4	5	Others	1.3%	4350.17	4	5	3.9%		
					56.0%	4.3%	0.7%			50.0%	50.0%			46.0%	48.1%	5.9%			48.8%	51.2%			
200	3375.40	1		3429.06	3	4	Others	1.6%	3551.76	3	4	5.2%	3431.69	3	Others	Others	1.7%	3453.69	3	Others	2.3%		
					51.3%	48.6%	0.1%			50.0%	50.0%			98.6%	1.4%	1.4%			100%				
300	1835.50	1		1851.64	3	4	Others	0.9%	2041.78	3	4	11.2%	1855.04	3	Others	Others	1.1%	1865.25	3	Others	1.6%		
					51.3%	48.6%	0.1%			50.0%	50.0%			99.4%	0.6%	0.6%			100%				
400	1495.20	1		1506.78	3	4	Others	0.8%	1820.89	3	4	21.8%	1511.36	3	Others	Others	1.1%	1522.95	3	Others	1.9%		
					51.6%	48.4%	0.001%			50.0%	50.0%			99.3%	0.7%	0.7%			100%				
500	1565.50	1		1572.28	3	4	Others	0.4%	2056.15	3	4	31.3%	1578.37	3	Others	Others	0.8%	1598.92	3	Others	2.1%		
					52.2%	47.8%	0.001%			50.0%	50.0%			99.1%	0.9%	0.9%			100%				
600	1829.90	1		1839.08	3	4	Others	0.5%	2041.78	3	4	11.6%	1846.96	3	Others	Others	0.9%	1865.54	3	Others	1.9%		
					53.2%	46.7%	0.1%			50.0%	50.0%			98.5%	1.5%	1.5%			100%				

- (iii) While the constrained-mode GBT analysis is able to capture accurately lateral-torsional buckling with only one deformation mode (mode **3** in purlins **P1**), the GBTUL analysis naturally requires modes **3** and **4**.

3.2 Buckling Behavior of Continuously Restrained Simply Supported Studs

Cold-formed steel stud walls are commonly sheathed with different boards, such as Gypsum Board (abbreviated as GB herein), Calcium-Silicate Board (CSB), Oriented-Strand Board (OSB), Magnesium Oxide Board (MOB) and Fiber-Cement Board (FCB). This work deals only with equally spaced (600 mm apart) simply supported cold-formed steel studs (i) exhibiting C 100×80×10×1.6 lipped channel cross-sections, (ii) with the structural sheathing continuously fastened on either one or both sides (*i.e.*, the studs are continuously restrained) and (ii) subjected to axial compression – see Fig. 1(b).

As proposed by Vieira Jr. & Schafer (2013) and Schafer (2013), the restraints provided by the sheathing to the studs are modeled by means of three continuous springs at each fastener-sheathing connection: two translational and one rotational springs. Their stiffness values are k_z (K_{TG} – lateral/tangential translational spring), k_y (K_{TN} – out-of-plane vertical/normal translational spring) and k_ϕ (K_R – rotational spring), as shown in Fig. 1(d). These stiffness values may be obtained experimentally (*e.g.*, Vieira Jr. 2011) or calculated/estimated on the basis of (i) the mechanical and geometrical properties of the sheathing and cold-formed steel stud, and (ii) the dimensions and spacing of the screws/fasteners (*e.g.*, Vieira Jr. & Schafer 2013, Schafer 2013) – the latter approach is adopted in this work.

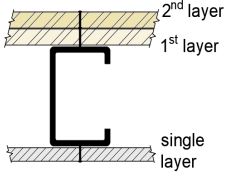
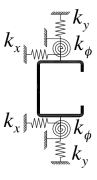
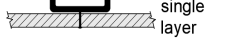
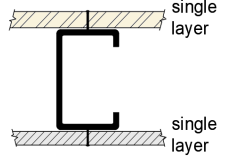

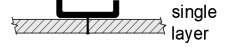
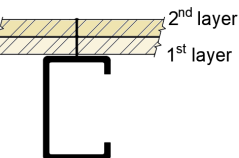
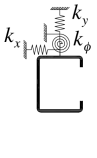

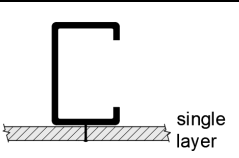

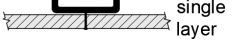
The four illustrative sheathing configurations depicted in Table 6 are considered in this work. They consist of (i) a single-layer or double-layer MOB attached to one side of the stud (height 2400 mm , thickness 20 mm and the mechanical properties reported by Sonkar *et al.* 2020) and a single-layer GB (height 2400 mm , thickness 12.5 mm and the mechanical properties given in the Gypsum Association GA-235-10 Report 2019) attached to the other side (studs **S1** and **S2** – single and double-layer MOB, respectively), or (ii) no sheathing board (termed Bare herein) on one side of the stud and either a double-layer MOB (stud **S3**) or a single-layer (stud **S4**) GB attached to the other side – the sheathing board dimensions and mechanical properties are those given for studs **S1** and **S2**. Concerning the MOB fastener spacing, 250 mm was chosen for the layer in contact with the stud flange – in the case of a double-layer MOB, the same spacing is used also for the second layer and, since the first and second layer fasteners are staggered, the first layer effective fastener spacing becomes 125 mm (as in Sonkar *et al.* 2020). As for the (single-layer) GB fastener spacing, it is always kept equal to 300 mm . Regardless of the sheathing configurations, all fasteners have a 4 mm diameter. The values of three sheathing-based spring stiffness values (k_z , k_y and k_ϕ – usual nomenclature) associated with the four sheathing configurations (sheathed studs **S1** to **S4**), calculated as proposed in Vieira Jr. & Schafer (2013) and Schafer (2013), are given in Table 6. It is still worth noting that, for comparison purposes, an unsheathed stud (both sides bare) is also considered – stud **S0**.

For each sheathed stud, Fig. 13 displays the 9 most relevant constrained deformation modes obtained by means of the proposed restrained cross-section analysis procedure (mode **1** stands for axial extension) – for comparison purposes, Fig. 14 depicts the (standard) deformation modes yielded by GBTUL for the unrestrained stud **S0**. Table 7 provides the sheathed stud (diagonal) matrix components \bar{C}_{kk} , \bar{D}_{kk} and \bar{B}_{kk} . The observation of the results presented in these two figures and table prompts the following remarks:

- (i) All the deformation modes of the sheathed studs are identified during Stage 1 of the simultaneous diagonalization procedure – in fact, all \bar{B}_{kk} ($k \geq 2$) components are non-null.
- (ii) While the restraints considered practically do not constrain the local deformation modes **7-10**, all sheathed studs exhibit several fully (minor-axis bending) or partially (major-axis bending, distortional and torsion) constrained deformation modes.
- (iii) Deformation mode **2** of studs **S1**, **S2** and **S4** involves major-axis bending with spring deformations and no transverse bending of the walls – indeed, the \bar{B}_{22} values concerning these studs stem from the elastic strain energy stored in the translational springs and the corresponding \bar{D}_{22} components are null.
- (iv) Deformation modes **3** and **4** of all sheathed studs combine torsion, bending about centroidal axes and transverse bending of the walls.
- (v) Constrained deformation modes provide valuable information about the sheathed stud mechanics prior to performing its structural analysis. For instance, an asymmetric distortional behavior is expected in all sheathed studs, due to presence of different rotational restraints on each side (in studs **S3** and **S4** such restraints are only on one side) – this behavioral feature is already embedded in the various deformation modes **5** (see the different flange rotations, particularly in studs **S3** and **S4**).

Next, Fig. 15 makes it possible to compare the signature curves P_{cr} vs. L (logarithmic scale) concerning the unsheathed (**S0**) and sheathed (**S1** to **S4**) studs. In order to validate the proposed approach, based on GBT constrained deformation modes, Fig. 15 also includes P_{cr} values yielded by the programs GBTUL (circles) and CUFSM (symbols \times). Figs. 16(a)-(b), on the other hand, show the modal

Table 6: Spring stiffness values of the four sheathed studs considered in this work (studs **S1** to **S4**)

Sheathed Studs		Restraints	k_z (K_{TG}) kN/cm/cm	k_y (K_{TN}) kN/cm/cm	k_θ (K_R) kNcm/rad/cm	Number of layers	Sheathing board
S1			0.16906	1.057E-03	1.03336	2	MOB
			0.10989	2.985E-05	0.35481	1	GB
S2			0.05746	5.285E-04	0.51668	1	MOB
			0.10989	2.985E-05	0.35481	1	GB
S3			0.16906	1.057E-03	1.03336	2	MOB
			-	-	-	0	Bare
S4			-	-	-	0	Bare
			0.10989	2.985E-05	0.35481	1	GB

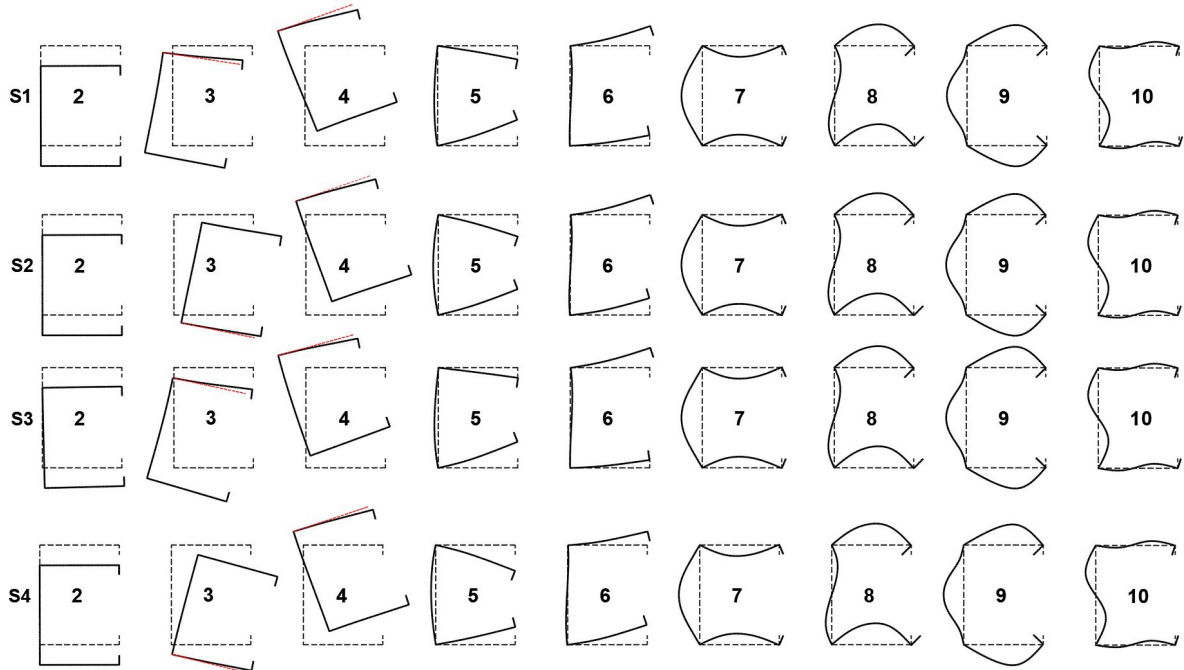


Figure 13: Constrained deformation modes **2-10** of the sheathed studs **S1**, **S2**, **S3**, and **S4**

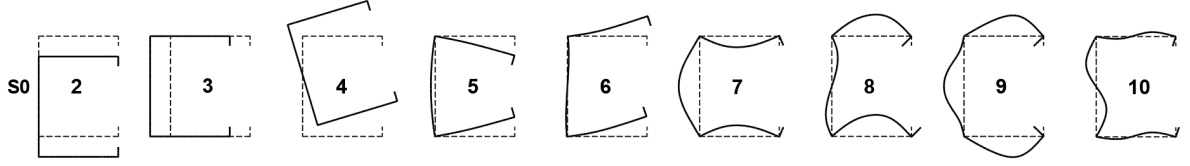


Figure 14: Constrained deformation modes **2-10** of the unsheathed (**S0**) stud (yielded by GBTUL)

Table 7: Stiffness matrix components \bar{C}_{kk} , \bar{B}_{kk} and \bar{D}_{kk} concerning modes **2-10** of the unsheathed (**S0**) and sheathed (**S1** to **S4**) – dimensions in *cm*, Young's and shear moduli in *kN/cm²*

$\bar{C}_{kk} \times 10^3$										S0									
										1625.96	734.317	14046.6	2.2079	2.36199	0.05741	0.07582	0.09002	0.04639	
S1										S2									
1637.2	13.128	11.2018	1.44268	1.47103	0.05746	0.07561	0.09045	0.04586		1636.57	12.5856	10.0572	1.90856	1.99341	0.05744	0.07584	0.09033	0.04608	
S3										S4									
1756.79	10.4718	10.605	1.31394	1.32522	0.05744	0.07535	0.09026	0.04595		1635.04	10.2058	10.0245	1.64993	1.71310	0.05743	0.07567	0.09014	0.04623	
$\bar{B}_{kk} \times 10^{-2}$										S0									
										0	0	0	5.2935	11.3008	96.8344	298.921	533.749	1133.84	
S1										S2									
0.10878	0.44553	0.66984	5.5647	10.2389	96.9745	298.455	538.042	1128.17		0.05587	0.23447	0.38622	6.63872	11.9878	96.9258	299.216	536.702	1130.81	
S3										S4									
0.10572	0.01825	0.58741	4.0699	8.9827	96.9336	297.37	536.459	1128.39		0.00299	0.00842	0.35328	4.54938	9.19403	96.8701	298.400	534.891	1131.85	
\bar{D}_{kk}										S0									
										0	0	294.5	5.493	5.922	14.92	31.44	35.33	43.67	
S1										S2									
0	0.03433	0.1662	3.597	3.696	14.94	31.33	35.39	42.98		0	0.04601	0.1437	4.755	5.004	14.94	31.44	35.38	43.25	
S3										S4									
0.02333	0.0765	0.1284	3.272	3.329	14.93	31.23	35.34	43.12		0	0.08103	0.1213	4.107	4.297	14.93	31.38	35.35	43.47	

participation diagrams of studs **S1-S4**, based on both the unconstrained (left side) and constrained (right side) deformation modes. As for Fig. 17, it displays the buckled mid-span cross-sections of studs lengths corresponding to either signature curve local minima or a selected length value (when no such minima exist), based on the GBT constrained deformation modes – they can be compared with the critical buckling mode shapes yielded by the program CUFSM that are shown in Fig. 15. Concerning these buckling results, it is worth pointing out that:

- (i) Once again, there is an excellent agreement between the critical loads provided by the FSM and two GBT buckling analyses. Indeed, the average difference between the three sets of P_{cr} values is 0.9%, with a maximum of 2.3%, occurring for stud **S1** with $L=19.3\text{ cm}$. Moreover, the buckling mode shapes yielded by the FSM and constrained GBT analyses virtually coincide.
- (ii) For $L \leq 16.7\text{ cm}$, the studs buckle in local modes (with a 95% participation of deformation mode **7** in both GBT analyses) that are identical for all the studs analyzed in this work – as anticipated from the coincidence of their local deformation modes. The solid and dashed curves are virtually identical, as well as the critically buckled mid-span cross-sections – as observed by Schafer (2013), this is because k_x and k_ϕ do not influence local buckling, and the determination of k_y is base on the global bending resistance (not the local one).
- (iii) Sheathing provides a beneficial rotational restraint against distortional buckling – indeed, the GBT-based (with constrained deformation modes) critical distortional buckling loads are 67.07 kN (**S0**), 71.14 kN (**S4**), 74.80 kN (**S3**), 77.52 kN (**S2**) and 81.08 kN (**S1**) – *i.e.*, the critical buckling load increases up to 20.9%. While the unsheathed stud distortional buckling mode is symmetrical, all the sheathed stud ones are asymmetric – this was also anticipated from the distortional constrained deformation mode shapes.

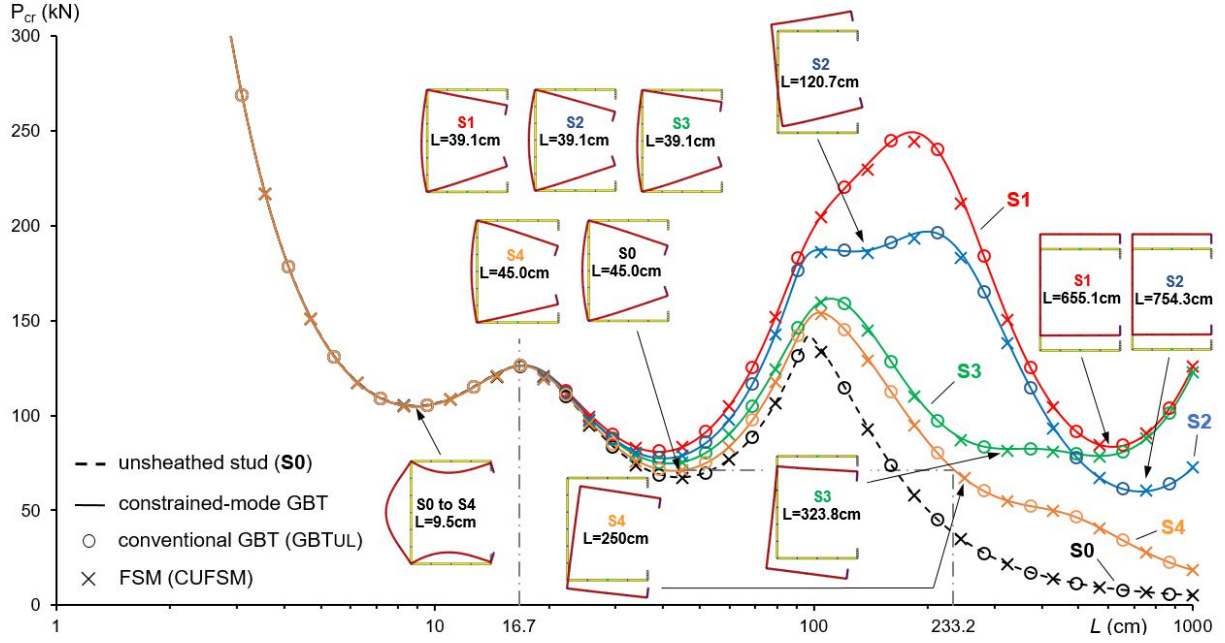


Figure 15: Signature curves P_{cr} vs. L and critically buckled mid-span cross-sections of studs **S0-S4**

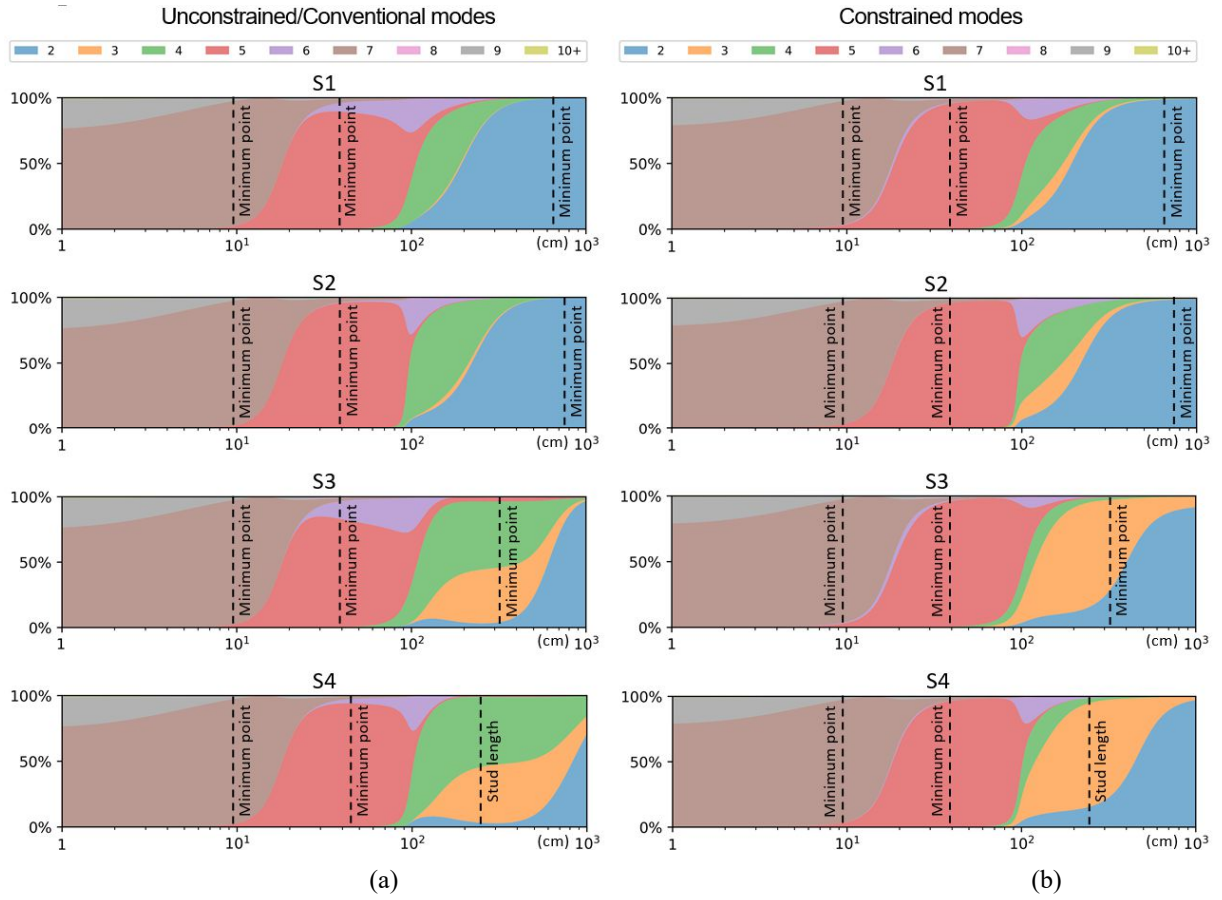


Figure 16: Modal participation diagrams of studs **S1-S4** based on (a) unconstrained and (b) constrained GBT deformation modes

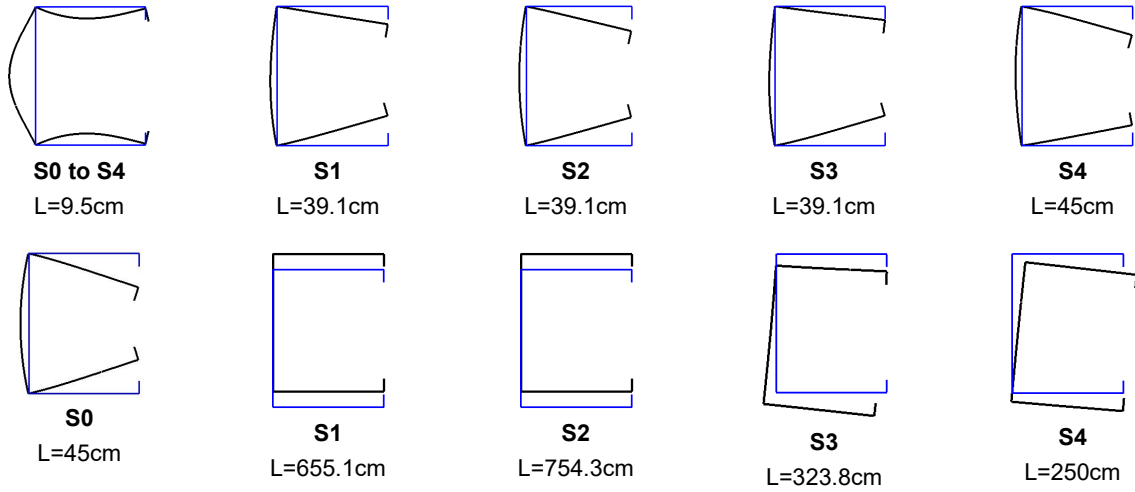


Figure 17: Critically buckled mid-span cross-sections of studs **S0-S4** based on GBT constrained deformation modes

- (iv) The unconstrained modal participation diagrams displayed in Fig. 16(a) clearly show that the sheathed stud distortional buckling modes shapes are obtained as combinations of the symmetric (mode **5** – contributions ranging from 83.8% to 95.6%) and anti-symmetric (mode **6** – contributions ranging from 0.5% to 13.4%) distortional modes. The same distortional buckling shapes practically coincide with the constrained deformation modes **5** (contributions ranging from 95.4% to 97.2%), as shown in Fig. 16(b). In other words, accurate buckling results may be obtained with just one constrained deformation mode included in the GBT analyses (two unconstrained modes would be indispensable to match this accuracy).
- (v) The signature curves of studs **S1** and **S2** exhibit local minima, corresponding to critical buckling loads associated with major-axis global buckling, at $L=656.1\text{ cm}$ and $L=754.3\text{ cm}$, respectively.
- (vi) The buckling modes of studs **S4** with $L \geq 233.2\text{ cm}$ involve predominantly a combination of bending and torsion deformations (combinations of unconstrained deformation modes **2**, **3** and **4** or constrained deformation modes **2** and **3** – see Figs. 14 and 13, respectively).

In order to enable a more in-depth understanding about the stud buckling behavior, Fig. 18 shows the variation of the critical buckling load P_{cr} and mode shape with the length L (logarithmic scale) provided by ANSYS SFE and constrained-mode GBT analyses (solid and dashed curves – $\eta > 1$ in Eq. (21)). This figure also displays several critical buckling mode shapes provided by the ANSYS SFEA and the associated half-wave numbers (given inside brackets). The close observation of the buckling results displayed in this figure prompts the following remarks:

- (i) The GBT and ANSYS critical buckling loads are again extremely close – all differences below 1%. In addition, there is also very close agreement between the buckling mode shapes provided by both analyses.
- (ii) For $L \lesssim 23.5\text{ cm}$, buckling occurs in local modes with 1 to 3 half-waves. For $L \gtrsim 23.5\text{ cm}$, the studs buckle in distortional modes with increasing half-wave numbers up to the following lengths: $L=168.4\text{ cm}$ (**S0** – 4 half-waves), $L=233.2\text{ cm}$ (**S4** – 5 half-waves), $L=495.4\text{ cm}$ (**S2** – 12 half-waves) and at least $L=800\text{ cm}$ (**S1** and **S3** – 21 and 19 half-waves, respectively).
- (iii) While studs **S4** with $L > 233.2\text{ cm}$ buckle in major-axis flexural-torsional modes, studs **S2** with $L > 495.4\text{ cm}$ buckle in minor-axis flexural modes – in both cases, P_{cr} decreases very rapidly with L .

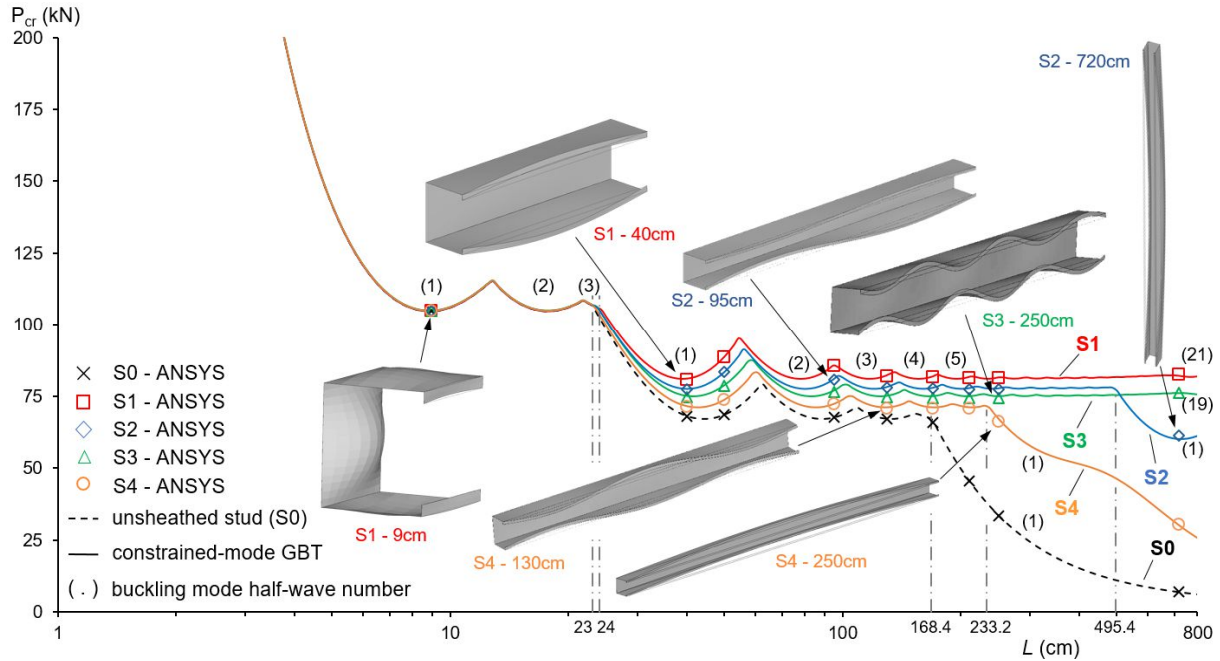


Figure 18: Variation of the stud critical buckling load and mode shape with the length – studs **S0-S4**

Finally, an assessment of the critical distortional buckling loads of sheathed studs is presented next, following the approach employed previously for the restrained purlins. Tables 8 to 11 show the stud critical distortional buckling loads provided by (i) ANSYS SFEA, (ii) constrained-mode GBT analyses including all deformation modes, only the two most relevant ones or just the dominant one, and (iii) conventional-mode (GBTUL) GBT analyses including all deformation modes or only the two most relevant ones. The tables also include values yielded by constrained Finite Stripe Method (cFSM) analyses, available in the program CUFSM^{14 15}. The observation of the distortional buckling results presented prompts the following remarks:

- (i) First, and as expected, the critical buckling load values yielded by cFSM analyses that include all the modal subspaces (*i.e.*, L+D+G+other) are virtually identical to those provided by the ANSYS SFEA and by both GBT analyses that include all the (conventional or constrained) deformation modes.
- (ii) The conventional-mode GBT analyses including the two most relevant deformation modes (**5** and **6**) and constrained-mode GBT analyses including the dominant deformation mode (**5**) provide P_{cr} approximations with practically identical error averages: 3.8% (maximum: 4.6%) vs. 3.9% (maximum: 5.1%). On the other hand, cFSM analyses including only the distortional subspace (D) yield P_{cr} approximations with errors averaging 7.8% (maximum: 11.1%).

¹⁴ The cFSM was originally derived from the semi-analytical FSM by Ádány and Schafer (2008) and can be viewed as an approach to separate the overall deformation of a thin-walled member into various components that exhibit global (G), distortional (D), local (L) and other (*e.g.*, shear or transverse extension) kinematic characteristics.

¹⁵ The distortional buckling mode may be difficult to identify in a conventional finite strip analysis. In such cases, Schafer (2013), Vieira Jr. (2011) and Sonkar *et al.* (2020) recommended using the cFSM to obtain the critical distortional buckling mode determine the associated critical buckling load, in the context of predicting ultimate strengths of sheathed studs by means of a DSM-based approach.

Table 8: GBT, cFSM and ANSYS critical distortional buckling results for stud **S1**

L (cm)	ANSYS		Conventional Modes (GBTUL)							Constrained Finite Strip Method (CUFSM)							Constrained Modes (C-GBT)						
	P _{cr,ANSYS} (kN)	Half Wave	All Modes				Two Modes			All Modal Subspaces				One Modal Subspace			All Modes				One/Two Modes		
			P _{cr,GBTUL} (kN)	Modal Participations			P _{cr,GBTUL} (kN)	Modes		P _{cr,cFSM} (kN)	Modal Participations			P _{cr,cFSM} (kN)	Subspace	cFSM ANSYS	P _{cr,C-GBT} (kN)	Modal Participations			P _{cr,C-GBT} (kN)	Mode(s)	C-GBT ANSYS
40	80.788	1	81.201	5	6	Others	84.521	5	6	80.704	D	L	Others	88.000	D	8.9%	81.158	5	7	Others	84.469	5	4.6%
			89.11%	6.87%	4.02%	0.5%	92.99%	7.01%	4.6%		92.30%	6.30%	1.40%		100%			95.62%	2.74%	1.63%		100%	
50	88.635	1	88.981	5	6	Others	92.095	5	6	88.563	D	L	Others	94.350	D	6.4%	88.886	5	7	Others	91.813	5	3.6%
			87.63%	9.05%	3.32%	0.4%	91.25%	8.75%	3.9%		92.90%	4.60%	2.50%		100%			96.66%	1.91%	1.44%		100%	
95	85.456	3	86.015	5	6	Others	89.060	5	6	85.351	D	L	Others	91.584	D	7.2%	85.743	5	7	Others	88.838	5	4.0%
			86.01%	8.56%	5.43%	0.7%	91.60%	8.40%	4.2%		88.70%	10.40%	0.90%		100%			96.53%	2.05%	1.42%		100%	
130	82.034	3	82.492	5	6	Others	85.582	5	6	82.049	D	L	Others	88.573	D	8.0%	82.864	5	7	Others	85.479	5	4.2%
			88.69%	7.68%	3.63%	0.6%	92.30%	7.70%	4.3%		92.80%	5.50%	1.70%		100%			96.24%	2.29%	1.47%		100%	
170	81.550	4	82.030	5	6	Others	85.158	5	6	81.577	D	L	Others	88.260	D	8.2%	81.910	5	7	Others	85.139	5	4.4%
			82.03%	7.48%	10.49%	0.6%	92.46%	7.54%	4.4%		92.70%	5.70%	1.60%		100%			96.03%	2.45%	1.52%		100%	
210	81.301	5	81.795	5	6	Others	84.952	5	6	81.335	D	L	Others	88.124	D	8.4%	81.894	5	7	Others	85.073	5	4.6%
			88.87%	7.37%	3.76%	0.6%	92.56%	7.44%	4.5%		92.70%	5.80%	1.50%		100%			96.02%	2.46%	1.52%		100%	
250	81.153	6	81.658	5	6	Others	84.836	5	6	81.192	D	L	Others	88.056	D	8.5%	81.624	5	7	Others	85.177	5	5.0%
			88.92%	7.29%	3.79%	0.6%	92.63%	7.37%	4.5%		92.60%	5.90%	1.50%		100%			95.91%	2.53%	1.55%		100%	

Table 9: GBT, cFSM and ANSYS critical distortional buckling results for stud **S2**

L (cm)	ANSYS		Conventional Modes (GBTUL)							Constrained Finite Strip Method (cFSM - CUFSM)							Constrained Modes (C-GBT)						
	P _{cr,ANSYS} (kN)	Half Wave	All Modes				Two Modes			All Modal Subspaces				One Modal Subspace			All Modes				One/Two Modes		
			P _{cr,GBTUL} (kN)	Modal Participations			P _{cr,GBTUL} (kN)	Modes		P _{cr,cFSM} (kN)	Modal Participations			P _{cr,cFSM} (kN)	Subspace	cFSM ANSYS	P _{cr,C-GBT} (kN)	Modal Participations			P _{cr,C-GBT} (kN)	Mode(s)	C-GBT ANSYS
40	77.271	1	77.589	5	6	Others	80.351	5	6	77.216	D	L	Others	83.805	D	8.5%	77.5211	5	7	Others	80.237	5	3.8%
			95.78%	0.55%	3.67%	0.4%	99.48%	0.52%	4.0%		93.30%	6.00%	0.70%		100%			95.48%	3.38%	1.14%		100%	
50	83.379	1	83.583	5	6	Others	85.821	5	6	83.345	D	L	Others	88.096	D	5.7%	83.4643	5	7	Others	85.574	5	2.6%
			96.49%	0.78%	2.73%	0.2%	99.32%	0.68%	2.9%		94.70%	4.30%	1.00%		100%			96.84%	2.31%	0.86%		100%	
95	80.806	2	81.086	5	6	Others	83.359	5	6	80.833	D	L	Others	85.858	D	6.3%	80.8248	5	7	Others	83.152	5	2.9%
			96.41%	0.72%	2.87%	0.3%	99.35%	0.65%	3.2%		94.60%	4.60%	0.80%		100%			96.61%	2.49%	0.90%		100%	
130	77.969	3	78.314	5	6	Others	80.767	5	6	78.013	D	L	Others	83.733	D	7.4%	78.0228	5	7	Others	80.639	5	3.4%
			96.16%	0.63%	3.21%	0.4%	99.42%	0.58%	3.6%		94.00%	5.30%	0.70%		100%			96.21%	2.80%	0.99%		100%	
170	77.628	4	77.996	5	6	Others	80.510	5	6	77.681	D	L	Others	83.587	D	7.7%	77.8806	5	7	Others	80.458	5	3.6%
			96.08%	0.61%	3.31%	0.5%	99.43%	0.57%	3.7%		93.90%	5.40%	0.70%		100%			95.95%	3.01%	1.04%		100%	
210	77.463	5	77.848	5	6	Others	80.402	5	6	77.522	D	L	Others	83.549	D	7.9%	77.8735	5	7	Others	80.484	5	3.9%
			96.03%	0.60%	3.37%	0.5%	99.44%	0.56%	3.8%		93.80%	5.50%	0.70%		100%			95.94%	3.01%	1.04%		100%	
250	77.371	6	77.767	5	6	Others	80.351	5	6	77.434	D	L	Others	83.546	D	8.0%	77.7178	5	7	Others	80.649	5	4.2%
			95.99%	0.59%	3.42%	0.5%	99.45%	0.55%	3.9%		93.70%	5.60%	0.70%		100%			95.82%	3.11%	1.07%		100%	

Table 10: GBT, cFSM and ANSYS critical distortional buckling results for stud **S3**

L (cm)	ANSYS		Conventional Modes (GBTUL)								Constrained Finite Strip Method (cFSM - CUFSM)								Constrained Modes (C-GBT)								
	P _{cr,ANSYS} (kN)	Half Wave	All Modes				Two Modes				All Modal Subspaces				One Modal Subspace				All Modes				One/Two Modes				
			P _{cr,GBTUL} (kN)	Modal Participations			GBTUL ANSYS	P _{cr,GBTUL} (kN)	Modes			GBTUL ANSYS	P _{cr,cFSM} (kN)	Modal Participations			cFSM ANSYS	P _{cr,cFSM} (kN)	Subspace	cFSM ANSYS	P _{cr,C-GBT} (kN)	Modal Participations			C-GBT ANSYS	P _{cr,C-GBT} (kN)	Mode(s)
40	74.595	1	74.935	5 82.46%	6 13.94%	Others 3.60%	0.5%	77.862	5 86.02%	6 13.98%	4.4%	74.566	D 92.60%	L 5.60%	Others 1.80%	0.0%	81.352	D 100%	9.1%	74.9387	5 96.23%	7 1.92%	Others 1.86%	0.5%	78.013	5 100%	4.6%
50	78.491	1	78.710	5 79.56%	6 17.43%	Others 3.01%	0.3%	81.431	5 82.97%	6 17.03%	3.7%	78.494	D 92.90%	G 3.80%	Others 3.30%	0.0%	83.728	D 100%	6.7%	78.7115	5 97.04%	7 1.20%	Others 1.76%	0.3%	81.456	5 100%	3.8%
95	76.528	2	76.827	5 80.27%	6 16.70%	Others 3.03%	0.4%	79.476	5 83.58%	6 16.42%	3.9%	76.591	D 93.10%	L 4.10%	Others 2.80%	0.1%	82.000	D 100%	7.2%	76.7172	5 96.98%	7 1.32%	Others 1.70%	0.2%	79.531	5 100%	3.9%
130	74.616	3	74.986	5 81.48%	6 15.29%	Others 3.23%	0.5%	77.681	5 84.80%	6 15.20%	4.1%	74.694	D 93.00%	L 4.80%	Others 2.20%	0.1%	80.679	D 100%	8.1%	75.1708	5 96.76%	7 1.53%	Others 1.71%	0.7%	77.810	5 100%	4.3%
170	74.448	4	74.842	5 81.72%	6 14.97%	Others 3.31%	0.5%	77.577	5 85.09%	6 14.91%	4.2%	74.534	D 93.00%	L 4.90%	Others 2.10%	0.1%	82.686	D 100%	11.1%	74.8433	5 96.58%	7 1.67%	Others 1.75%	0.5%	77.783	5 100%	4.5%
210	74.387	5	74.796	5 81.87%	6 14.78%	Others 3.35%	0.6%	77.559	5 85.26%	6 14.74%	4.3%	74.478	D 92.90%	L 5.10%	Others 2.00%	0.1%	80.740	D 100%	8.5%	74.8468	5 96.58%	7 1.67%	Others 1.75%	0.6%	77.904	5 100%	4.7%
250	74.363	6	74.783	5 81.97%	6 14.64%	Others 3.39%	0.6%	77.568	5 85.38%	6 14.62%	4.3%	74.457	D 92.90%	L 5.10%	Others 2.00%	0.1%	80.796	D 100%	8.7%	74.8247	5 96.49%	7 1.74%	Others 1.78%	0.6%	78.137	5 100%	5.1%

Table 11: GBT, cFSM and ANSYS critical distortional buckling results for stud **S4**

L (cm)	ANSYS		Conventional Modes (GBTUL)							Constrained Finite Strip Method (cFSM - CUFSM)							Constrained Modes (C-GBT)											
	P _{cr,ANSYS} (kN)	Half Wave	All Modes				GBTUL ANSYS	Two Modes			All Modal Subspaces				One Modal Subspace			All Modes				One/Two Modes						
			P _{cr,GBTUL} (kN)	Modal Participations				P _{cr,GBTUL} (kN)	Modes		GBTUL ANSYS	P _{cr,cFSM} (kN)	Modal Participations			cFSM ANSYS	P _{cr,cFSM} (kN)	Subspace	cFSM ANSYS	P _{cr,C-GBT} (kN)	Modal Participations			C-GBT ANSYS	P _{cr,C-GBT} (kN)	Mode(s)		C-GBT ANSYS
40	71.185	1	71.453	5 93.94%	6 2.77%	Others 3.29%	0.4%		5 97.43%	6 2.57%	3.6%	71.178	D 93.70%	L 5.40%	Others 0.90%	0.0%	77.228	D 100%	8.5%	71.428	5 96.53%	7 2.35%	Others 1.12%	0.3%	73.787	5 100%		3.7%
50	73.624	1	73.734	5 93.78%	6 3.86%	Others 2.36%	0.1%		5 96.58%	6 3.42%	2.5%	73.653	D 94.80%	L 3.70%	Others 1.50%	0.0%	77.738	D 100%	5.6%	73.700	5 97.70%	7 1.44%	Others 0.86%	0.1%	75.438	5 100%		2.5%
95	72.044	2	72.239	5 93.91%	6 3.61%	Others 2.48%	0.3%		5 96.76%	6 3.24%	2.8%	72.128	D 94.80%	L 4.00%	Others 1.20%	0.1%	76.524	D 100%	6.2%	72.125	5 97.52%	7 1.60%	Others 0.89%	0.1%	74.013	5 100%		2.7%
130	70.748	3	71.026	5 94.01%	6 3.17%	Others 2.82%	0.4%		5 97.11%	6 2.89%	3.2%	70.842	D 94.40%	L 4.60%	Others 1.00%	0.1%	75.988	D 100%	7.4%	71.085	5 97.18%	7 1.98%	Others 0.84%	0.5%	73.050	5 100%		3.3%
170	70.700	4	71.004	5 94.00%	6 3.07%	Others 2.93%	0.4%		5 97.18%	6 2.82%	3.4%	70.801	D 94.20%	L 4.80%	Others 1.00%	0.1%	76.142	D 100%	7.7%	71.000	5 96.95%	7 2.03%	Others 1.02%	0.4%	73.162	5 100%		3.5%
210	70.709	5	71.031	5 94.00%	6 3.01%	Others 2.99%	0.5%		5 97.23%	6 2.77%	3.4%	70.815	D 94.10%	L 4.90%	Others 1.00%	0.1%	76.282	D 100%	7.9%	71.011	5 96.94%	7 2.04%	Others 1.02%	0.4%	73.364	5 100%		3.8%
250	66.250	1	66.813	3 42.59%	4 53.31%	Others 4.10%	0.8%		3 45.22%	4 54.78%	23.2%	66.522	G 95.20%	D 4.70%	Others 0.10%	0.4%	74.520	G 100%	12.5%	66.918	2 1.37%	3 98.02%	Others 0.61%	1.0%	70.044	2 1.42%	3 98.58%	5.7%

- (iii) Stud **S4** with $L=250\text{ cm}$ is the sole one not buckling in a distortional mode. In this particular case, the GBTUL and cFSM analyses only provide accurate buckling results if more than two conventional deformation modes (GBTUL) or one modal subspace (cFSM) are included. Indeed, the inclusion of only the most relevant two deformation modes (**3** and **4** – 95.9% joint participation) or modal subspace (G subspace – 95.2% participation) leads to 23.2% and 12.5% errors, respectively. On the other hand, a GBT analysis including the most relevant two constrained deformation modes (**2** and **3** – 99.4% joint participation) leads to just a 5.7% error.

4. Semi Analytical Formulae

A very relevant GBT feature, stemming from its folded-plate theory origin, consists of the fact that it is possible to define mechanical properties associated with each cross-section deformation mode (modal mechanical properties). In order to obtain such properties and take full advantage of the GBT potential, it is necessary (i) to diagonalize matrices **C** and **B**, and (ii) to identify a set of orthogonal warping functions u_k – these procedures involve solving an auxiliary eigenvalue problem. In the case of the symmetric and anti-symmetric distortional deformation modes of unrestrained zed and lipped channel cross-sections, such task can be performed analytically, which enables the derivation of fully analytical distortional buckling formulae for members exhibiting those cross-sections (Silvestre & Camotim 2004a,b)¹⁶. This is no longer possible for restrained members, due to the fact that the cross-section analysis leads to asymmetric distortional (constrained) deformation modes – the above eigenvalue problem can only be solved numerically. Although this fact practically precludes the derivation of fully analytical distortional buckling formulae (very long, cumbersome and hard-to-handle expressions are obtained), it is still possible to derive semi-analytical distortional buckling formulae for restrained zed-section and lipped channel members. The designation “semi-analytical” stems from the fact that the formulae include parameters obtained from the numerical solution of fully analytically defined eigenvalue problems – this methodology was used by Silvestre & Camotim (2004c) to derive distortional buckling formulae for unrestrained rack-section members (the presence of seven walls precluded fully analytical formulae). This work addresses the derivation of GBT-based semi-analytical formulae intended to estimate the following simply supported member buckling loadings: (i) lateral-distortional (LD) buckling moments of purlins restrained by sheeting and (ii) distortional (D) buckling loads of sheathed studs – the various concepts and procedures involved in their derivation are presented next. Concerning the loadings, restraints conditions and deformation modes considered in the derivation of the formulae, it should be noted that:

- (i) The restraint provided by the sheeting to the purlins is modeled by means of continuous translational (K_{TG}) and rotational (K_R) springs with non-null stiffness values – see Fig. 7(d).
- (ii) The restraint provided by the sheathing to the studs is modeled by means of a set of three continuous springs at each restrained flange, with stiffness values equal to K_{TG} (k_z – lateral/tangential translational spring), K_{TN} (k_y – out-of-plane vertical/normal translational spring) and K_R (k_ϕ – rotational spring) – see Figs. 1(d) and 2(a).
- (iii) The purlins are acted by uniform bending moments about the centroidal axis perpendicular to the web. The ensuing pre-buckling (normal) stress distribution is displayed in Fig. 7(b): upper (connected) and bottom (free) flanges under uniform tensile and compressive stresses, respectively. As for the studs analyzed, they are all uniformly compressed.

¹⁶ Note that Schardt himself exploited the use of GBT to derive distortional buckling formulae (Schardt 1994).

- (iv) The LD buckling modes occurring in restrained purlins involves web transverse bending and strongly resemble the restrained purlin **P4** ($K_{TG} = \infty$ and $K_R > 0$) constrained GBT deformation mode **3** – see Fig. 9.
- (v) In the sheathed studs, the asymmetric (different sheathing in each side) and symmetric (equal sheathing in both sides) D buckling modes virtually coincide with the constrained and unconstrained GBT deformation modes **5** – see Figs. 13 (sheathed studs **S1-S4**) and 14 (unsheathed stud **S0**).

The bifurcation moment/load parameter estimates are provided by the general expression

$${}^j\lambda_{b-k} = \frac{1}{{}^jX_k} \left(C_k \left(\frac{\eta \pi}{L} \right)^2 + B_k \left(\frac{L}{\eta \pi} \right)^2 + D_k \right) \quad (22)$$

where (i) j identifies the member (purlin P or stud S), (ii) k identifies the buckling mode nature (LD or D), (ii) C_k , B_k and D_k are the cross-section modal mechanical properties of the constrained GBT deformation mode involved and (ii) jX_k is the corresponding cross-section geometric stiffness. After solving the equation $d {}^j\lambda_{b-k} / dL = 0$, one readily obtains the purlin/stud minimum LD/D bifurcation moment/load parameter ${}^j\lambda_{b-k}^{\min.}$, as well as the corresponding purlin/stud length L_{cr} – they read, respectively

$${}^j\lambda_{b-k}^{\min.} = \frac{2\sqrt{C_k B_k} + D_k}{{}^jX_k} \quad L_{cr-k} = \eta \pi \sqrt[4]{\frac{C_k}{B_k}} \quad (23)$$

Consider the restrained lipped channel and zed cross-sections with arbitrarily inclined lips depicted in Fig. 19, each discretized into six natural nodes and five walls (no intermediate nodes considered) – the figure also shows (i) the cross-section dimensions (t , ϕ , b_w , b_f , b_ℓ – thickness, lip-flange angle and web, flange, lip mid-line widths) and (ii) the top and bottom mid-flange restraint/spring stiffness values K_{TN}^i , K_{TG}^i , K_R^i ($i=I$ or $i=II$).

The derivation of the semi-analytical formulae involves three major tasks, namely (I) obtaining analytical expressions, written in terms of cross-section geometrical and material parameters, that provide the components of the matrices involved in the 6th-order auxiliary eigenvalue problem defined in Eq. (11), (II) solving numerically this eigenvalue problem (for the particular case under

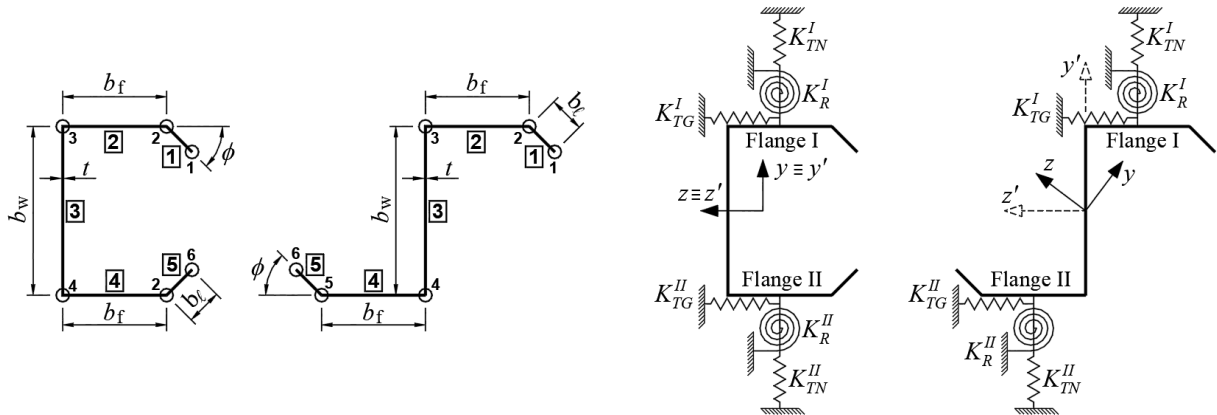


Figure 19: Lipped channel and zed cross-section dimensions, GBT discretizations (nodes + walls) and flange restraints

consideration) and (III) obtain expressions to estimate $^j\lambda_{b-k}^{\min.}$ and L_{cr} on the basis of the above numerical solution. For the sake of clarity, the steps involved in the performance of Tasks I, II and III are only briefly described next – most of the expressions required to perform the steps in Tasks I and III are given in Annexes A and B, respectively. Task I, aimed at defining the auxiliary eigenvalue problem, involves the following steps:

- (i) Define the geometrical and mechanical parameters

$$\alpha_\ell = \frac{b_\ell}{b_w} \quad \alpha_f = \frac{b_f}{b_w} \quad \beta_\ell = \alpha_\ell \sin(\phi) \quad \beta_f = \alpha_f \tan(\phi) \quad K = \frac{E t^3}{12(1-\nu^2)} \quad (24)$$

- (ii) Determine the transverse bending moment matrix

$$\mathbf{M} = -\mathbf{F}^{-1} \ddot{\mathbf{w}} \quad (25)$$

where the components of matrices \mathbf{F}^{-1} (wall transverse stiffness matrix) and $\ddot{\mathbf{w}}$ (wall relative rotation matrix – relative rotations between adjacent walls), given in Annex A, depend on the cross-section geometrical and material properties.

- (iii) Determine matrix \mathbf{B}^f , associated with the wall transverse bending stiffness and given by

$$\mathbf{B}^f = -\ddot{\mathbf{w}}^T \mathbf{M} \quad (26)$$

- (iv) Determine matrices \mathbf{B}^s (associated with the restraints/springs) and \mathbf{B} , expressed as

$$\mathbf{B}^s = \mathbf{K}_Z + \mathbf{K}_Y + \mathbf{K}_R \quad \mathbf{B} = \mathbf{B}^f + \mathbf{B}^s \quad (27)$$

where the components of the matrices \mathbf{K}_Z , \mathbf{K}_Y and \mathbf{K}_R , also given in Annex A, depend on the cross-section geometry and stiffness values K_{TN}^i , K_{TG}^i and K_R^i .

Task II begins by solving numerically the 6th-order eigenvalue problem

$$(\mathbf{B} - \lambda_k \mathbf{C}) \mathbf{u}_k = 0 \quad (k=1, \dots, 6) \quad (28)$$

where the expressions providing the components of matrix \mathbf{C} are also given in Annex A – the solution includes six eigenvectors of the form

$$\mathbf{u}_k = \{u_1 \ u_2 \ u_3 \ u_4 \ u_5 \ u_6\}^T \quad (29)$$

whose components are axial (warping) displacements at the cross-section (natural) nodes. Then, it is necessary to carry out the following procedures:

- (i) Identify the nodal warping displacements associated with the LD or D deformation modes:
- (i.1) In the restrained purlins (null K_{TN}^I , K_{TN}^{II} , K_{TG}^{II} , K_R^{II} values and $K_{TG}^I = \infty$), the eigenvector components associated with the smallest non-null eigenvalue provide the nodal warping displacements of the LD deformation mode (\mathbf{u}_{LD}).
 - (i.2) In the sheathed studs, the \mathbf{u}_5 eigenvector components correspond to the nodal warping displacements of the D deformation mode (\mathbf{u}_D).
- (ii) Determine the transverse bending moment vector concerning the LD or D deformation modes, given by

$$\mathbf{m}_{LD} = \mathbf{M} \mathbf{u}_{LD} = \{0 \ 0 \ m_3 \ m_4 \ 0 \ 0\}^T \quad \mathbf{m}_D = \mathbf{M} \mathbf{u}_D = \{0 \ 0 \ m_3 \ m_4 \ 0 \ 0\}^T \quad (30)$$

Finally, once the \mathbf{u}_{LD} , \mathbf{m}_{LD} or \mathbf{u}_D , \mathbf{m}_D components are known, Task III uses them to obtain the sought formulae to estimate $^j\lambda_{b-k}^{\min.}$ and L_{cr} – it comprises the following steps:

- (i) Determine the cross-section in-plane displacements ($v_{p,r-LD}$ or $v_{p,r-D}$), rotations ($\theta_{p,r-LD}$ or $\theta_{p,r-D}$) and flexural displacements ($w_{p,r-LD}$ or $w_{p,r-D}$) at each wall mid-point – the expressions providing these quantities are given in Annex B.
- (ii) Determine the cross-section modal mechanical (C_{LD} , B_{LD} , D_{LD} or C_D , B_D , D_D – warping, transverse bending and torsion stiffness constants) and geometrical ($^P X_{LD}$ or $^S X_D$) properties, by means of expressions also given in Annex B.

Fig. 20 shows the flowchart concerning the implementation of the above GBT-based purlin lateral-distortional and stud distortional buckling formulae, providing an overall view of all the steps and operations involved. The numbers inside the boxes identify the equations appearing either in this section or in Annexes A and B. This flowchart makes it easy to understand the approach followed to write a very small Python program that computes the buckling moment/load parameter estimates and may be implemented even in a pocket graphic calculator – the listing of the Python program written is given in Annex C. It is worth noting that the relative complexity of some of the expressions stems from the fact that they (i) incorporate genuine folded-plate theory, (ii) take into account the presence of the elastic springs modeling the member restraints and (iii) are written in a fully general and very compact form. However, note also that the input of the program merely consists of (i) identifying the formula used (purlin or stud), (ii) the zed-section or lipped channel dimensions (b_w, b_f, b_t, t, ϕ) and material properties (E, ν), and (iii) the spring stiffness values (K_{TN}, K_{TG}, K_R).

3.2 Illustration, Validation and Accuracy

In order to illustrate the application, validate and assess the accuracy of the derived GBT-based formulae to estimate purlin lateral-distortional and stud distortional buckling moments/loads, they are applied next to restrained purlins **P4** and sheathed studs **S1** with several lengths. The bifurcation moment/load estimates are compared with “exact” results provided by constrained-mode GBT analyses including all deformation modes.

The sequence of the most relevant parameters and results involved in calculating the **P4** purlin lateral-distortional and **S1** stud distortional buckling moment/load estimates is the following:

- (i) Geometrical and mechanical parameters

- Purlin **P4**

$$b_w = 19.75 \text{ cm}, b_f = 7.25 \text{ cm}, b_t = 2.375 \text{ cm}, t = 0.25 \text{ cm}, \phi = 90^\circ \text{ (zed-section)}$$

$$\rho = -1$$

$$E = 20500 \text{ kN/cm}^2, \nu = 0.3, G = 7884.615 \text{ kN/cm}^2$$

$$\alpha_t = \beta_t = 0.12025 \quad \alpha_f = 0.36709 \quad K = 29.33265 \text{ kNcm}$$

- Stud **S1**

$$b_w = 9.84 \text{ cm}, b_f = 7.84 \text{ cm}, b_t = 0.92 \text{ cm}, t = 0.16 \text{ cm}, \phi = 90^\circ \text{ (lipped channel)}$$

$$\rho = 1$$

$$E = 20500 \text{ kN/cm}^2, \nu = 0.3, G = 7884.615 \text{ kN/cm}^2$$

$$\alpha_t = \beta_t = 0.09350 \quad \alpha_f = 0.79675 \quad K = 7.68938 \text{ kNcm}$$

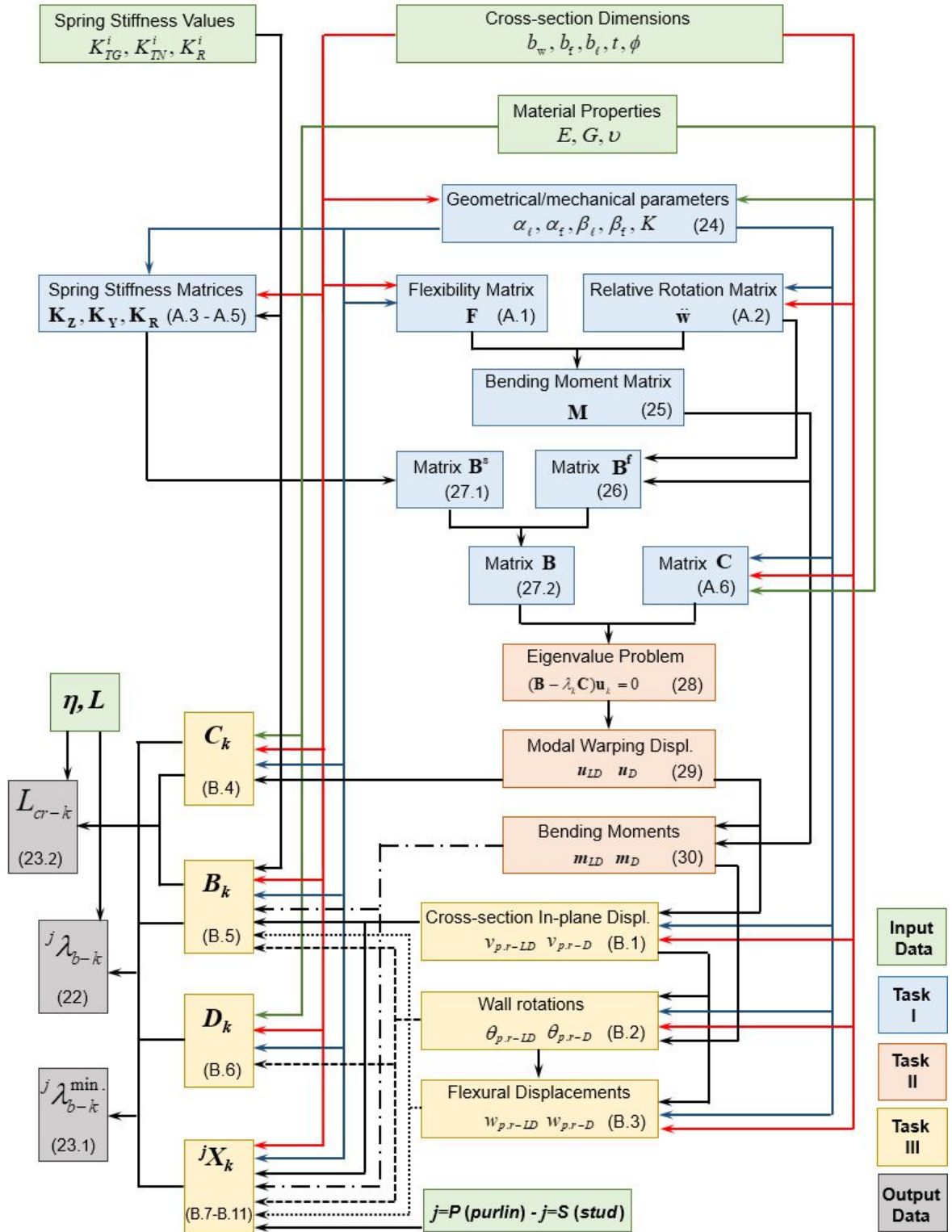


Figure 20: Flowchart of the steps and procedures involved in the application of the LD and D buckling formulae

(ii) Spring stiffness matrices

- Purlin **P4**

$$K_{TG}^I = \infty, K_R^I = 1.285 \text{ kNcm/cm/rad}$$

$$\mathbf{K}_Z = \begin{bmatrix} 0 & 0 & 0 & 0 & 0 & 0 \\ & 19.02 & -19.02 & 0 & 0 & 0 \\ & & 19.02 & 0 & 0 & 0 \\ & & & 0 & 0 & 0 \\ & sym & & & 0 & 0 \\ & & & & & 0 \end{bmatrix} \quad \mathbf{K}_R = 10^{-3} \begin{bmatrix} 4.33 & -4.33 & 0.52 & -0.52 & 0 & 0 \\ & 4.33 & -0.52 & 0.52 & 0 & 0 \\ & & 0.06 & -0.06 & 0 & 0 \\ & & & 0.06 & 0 & 0 \\ & sym & & & 0 & 0 \\ & & & & & 0 \end{bmatrix}$$

- Stud **S1**

$$K_{TG}^I = 0.16906 \text{ kN/cm/cm}, K_{TG}^{II} = 0.10989 \text{ kN/cm/cm},$$

$$K_{TN}^I = 1.057 \cdot 10^{-3} \text{ kN/cm/cm}, K_{TN}^{II} = 2.985 \cdot 10^{-5} \text{ kN/cm/cm},$$

$$K_R^I = 1.03336 \text{ kNcm/rad/cm}, K_R^{II} = 0.35481 \text{ kNcm/rad/cm}$$

$$\mathbf{K}_Z = 10^{-3} \begin{bmatrix} 0 & 0 & 0 & 0 & 0 & 0 \\ & 2.75 & -2.75 & 0 & 0 & 0 \\ & & 2.75 & 0 & 0 & 0 \\ & & & 1.79 & -1.79 & 0 \\ & sym & & & 1.79 & 0 \\ & & & & & 0 \end{bmatrix} \quad \mathbf{K}_Y = 10^{-4} \begin{bmatrix} 3.12 & -3.12 & -0.29 & 0.29 & 0 & 0 \\ & 3.12 & 0.29 & -0.29 & 0 & 0 \\ & & 0.03 & -0.03 & -0.01 & 0.01 \\ & & & 0.03 & 0.01 & -0.01 \\ & sym & & & 0.09 & -0.09 \\ & & & & & 0.09 \end{bmatrix}$$

$$\mathbf{K}_R = 10^{-2} \begin{bmatrix} 1.99 & -1.99 & 0.19 & -0.19 & 0 & 0 \\ & 1.99 & -0.19 & 0.19 & 0 & 0 \\ & & 0.02 & -0.02 & 0.06 & -0.06 \\ & & & 0.02 & -0.06 & 0.06 \\ & sym & & & 0.68 & -0.68 \\ & & & & & 0.68 \end{bmatrix}$$

(iii) Eigenvalue problems

- Purlin **P4**

$$\left[\underbrace{\begin{bmatrix} 1.70 & -1.91 & 3.57 & 0.06 & -0.67 & 0.46 \\ & 1904.67 & -1902.90 & -0.11 & 0.93 & -0.67 \\ & & 1902.58 & 0.02 & -0.16 & 0.11 \\ & & & 0.08 & -0.36 & 0.31 \\ & sym & & & 1.74 & -1.48 \\ & & & & & 1.27 \end{bmatrix}}_{\mathbf{B}} \right] - \lambda_k 10^3 \left[\underbrace{\begin{bmatrix} 4.06 & 2.03 & 0 & 0 & 0 & 0 \\ & 16.44 & 6.19 & 0 & 0 & 0 \\ & & 46.13 & 16.87 & 0 & 0 \\ & & & 46.13 & 6.19 & 0 \\ & sym & & & 16.44 & 2.03 \\ & & & & & 4.06 \end{bmatrix}}_{\mathbf{C}} \right] \cdot \underbrace{\begin{Bmatrix} u_1 \\ u_2 \\ u_3 \\ u_4 \\ u_5 \\ u_6 \end{Bmatrix}}_{\mathbf{u}_k} = \begin{Bmatrix} 0 \\ 0 \\ 0 \\ 0 \\ 0 \\ 0 \end{Bmatrix}$$

- Stud **S1**

$$10^{-2} \begin{bmatrix} 4.74 & -5.06 & 0.83 & -0.83 & 1.08 & -0.76 \\ & 5.72 & -1.23 & 0.95 & -1.47 & 1.08 \\ & & 0.54 & -0.27 & 0.83 & -0.71 \\ & & & 0.45 & -1.01 & 0.71 \\ & sym & & & 4.29 & -3.72 \\ & & & & & 3.40 \end{bmatrix} - \lambda_k 10^3 \begin{bmatrix} 1.01 & 0.50 & 0 & 0 & 0 & 0 \\ & 9.58 & 4.29 & 0 & 0 & 0 \\ & & 19.33 & 5.38 & 0 & 0 \\ & & & 19.33 & 4.29 & 0 \\ & sym & & & 9.58 & 0.50 \\ & & & & & 1.01 \end{bmatrix} \cdot \begin{Bmatrix} u_1 \\ u_2 \\ u_3 \\ u_4 \\ u_5 \\ u_6 \end{Bmatrix} = \begin{Bmatrix} 0 \\ 0 \\ 0 \\ 0 \\ 0 \\ 0 \end{Bmatrix}$$

B **C** **u_k**

(iv) Eigenvalue problem solution: nodal axial (warping) displacements

- Purlin **P4**

$$u_{LD} = \{-0.12811 \quad -0.09032 \quad -0.09032 \quad 0.49331 \quad -0.76178 \quad -1.00000\} \text{ cm}$$

- Stud **S1**

$$u_D = \{0.54235 \quad -0.07717 \quad 0.00073 \quad 0.04346 \quad -0.17400 \quad 1.00000\} \text{ cm}$$

(v) Nodal transverse bending moments

- Purlin **P4**

$$m_{LD} = \{0 \quad 0 \quad -0.00802 \quad -0.00030 \quad 0 \quad 0\} \text{ kNcm/cm}^2$$

- Stud **S1**

$$m_D = \{0 \quad 0 \quad -0.05314 \quad -0.20066 \quad 0 \quad 0\} \text{ kNcm/cm}^2$$

(vi) Modal displacements and rotations

- Purlin **P4**

$$\begin{array}{lll} v_{p.1} = -0.01591 \text{ cm/cm} & \theta_{p.1} = 0.00594 \text{ rad/cm} & w_{p.1} = -0.00705 \text{ cm/cm} \\ v_{p.3} = -0.02955 \text{ cm/cm} & \theta_{p.3} = 0.00877 \text{ rad/cm} & w_{p.3} = 0.08656 \text{ cm/cm} \\ v_{p.5} = 0.10030 \text{ cm/cm} & \theta_{p.5} = 0.00977 \text{ rad/cm} & w_{p.5} = -0.16151 \text{ cm/cm} \end{array}$$

- Stud **S1**

$$\begin{array}{lll} v_{p.1} = 0.67339 \text{ cm/cm} & \theta_{p.1} = -0.09437 \text{ rad/cm} & w_{p.1} = 0.05335 \text{ cm/cm} \\ v_{p.3} = -0.00434 \text{ cm/cm} & \theta_{p.3} = -0.00181 \text{ rad/cm} & w_{p.3} = -0.01884 \text{ cm/cm} \\ v_{p.5} = -1.27608 \text{ cm/cm} & \theta_{p.5} = 0.19742 \text{ rad/cm} & w_{p.5} = 0.11855 \text{ cm/cm} \end{array}$$

(vii) Cross-section modal mechanical properties

- Purlin **P4**

$$C_{LD} = 22482.24277 \text{ kNcm}^2 \quad B_{LD} = 7.08369 \cdot 10^{-5} \text{ kN/cm}^2 \quad D_{LD} = 0.11513 \text{ kN}$$

- Stud **S1**

$$C_D = 1403.17573 \text{ kNcm}^2 \quad B_D = 0.05480 \text{ kN/cm}^2 \quad D_D = 3.34037 \text{ kN}$$

(viii) Cross-section modal geometrical properties

- Purlin **P4**

$$^P X_{LD} = 0.00172 \text{ cm}^{-1}$$

$$I_{Z'} = 604.1706 \text{ cm}^4$$

- Stud **S1**

$$^S X_D = 0.25495$$

$$A = 4.3776 \text{ cm}^2$$

Incorporating the above values in Eqs. (23) leads to the minimum (i) purlin **P4** lateral-distortional bifurcation moment ($^P M_{b-LD}^{\min.}$ – LD buckling moment) estimate or (i) stud **S1** distortional bifurcation load ($^S P_{b-D}^{\min.}$ – D buckling load) estimate, as well as the associated purlin/stud critical half-wave lengths $L_{cr-k}^{\min.}$ (with $\eta=1$). Such estimates are given in Table 12, together with the GBT-based results including all constrained deformation modes. Finally, Figs. 21 and 22 show the variation of the bifurcation moment M_{b-LD} and load P_{b-D} with the length L (logarithmic scale) provided by semi-analytical formulae (solid curves – with $\eta \geq 1$ in Eq. (22)), for purlins **P4** and studs **S1**, respectively. In order to enable a more in-depth assessment of the potential of the proposed formulae, M_{b-LD} vs. L curves for purlins with different K_R^I stiffness values (ranging from 0.001

Table 12: **P4/S1** minimum LD/D bifurcation moments/loads and associated critical half-wave lengths

	Lateral-distortional buckling		Distortional buckling	
	Purlin P4		Stud S1	
	$^P M_{b-LD}^{\min.}$ (kNm)	$L_{cr-LD}^{\min.}$ (cm)	$^S P_{b-D}^{\min.}$ (kN)	$L_{cr-D}^{\min.}$ (cm)
Semi-analytical formulae	1533.83	419.32	81.89	39.74
Constrained-mode GBT	1496.87	423.89	81.13	39.10
Difference (%)	2.5	-1.1	0.9	1.6

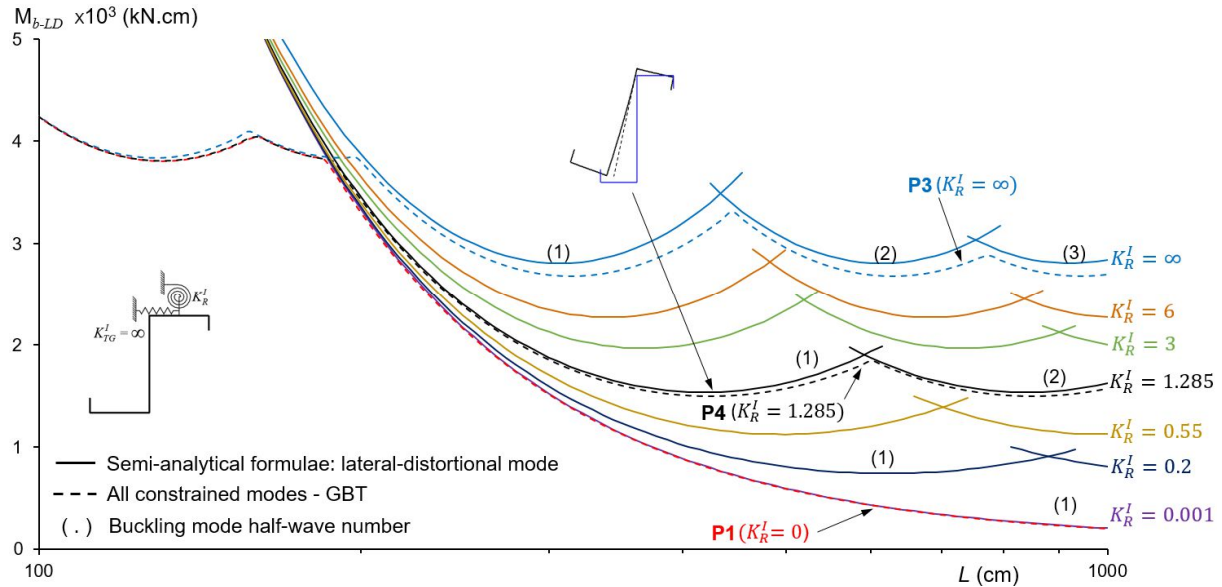


Figure 21: Purlin lateral-distortional buckling moment curves yielded by the semi-analytical formulae and GBT analyses

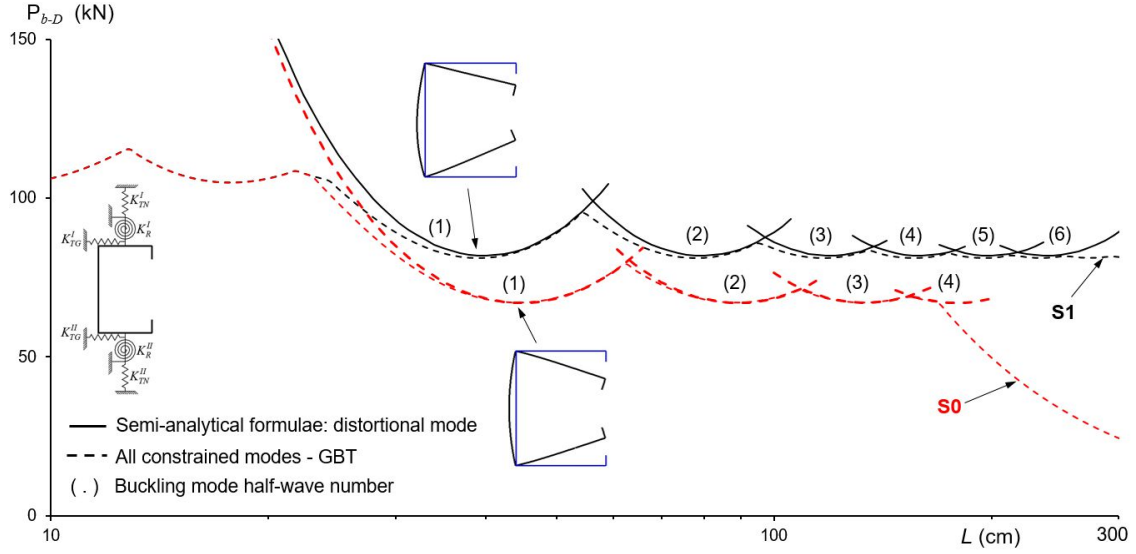


Figure 22: Stud distortional buckling loads yielded by the semi-analytical formulae and GBT analyses

to 1000 – the latter is deemed infinite, *i.e.*, concerns purlins **P3**) and P_{b-D} vs. L curves of unsheathed studs (**S0**) are also shown in each figure. Besides values yielded by the semi-analytical formulae, the figures also include, for validation and comparison purposes, critical buckling moment/load curves obtained from GBT-based analyses including all constrained deformation modes (dashed curves – $\eta \geq 1$ in Eq. (21)). The observation of this set of results prompts the following remarks:

- (i) The GBT-based formulae yield accurate $^P M_{b-LD}^{\min.}$, L_{cr-LD} , $^S P_{b-D}^{\min.}$ and L_{cr-D} estimates for the purlins **P4** and studs **S1** – the error never exceeds 2.5%..
- (ii) The values below the intersection points of the individual bifurcation curves (*i.e.*, curves with $\eta=1, 2 \dots$) represent the critical buckling moment/load estimates – note that the curves provided by the formulae are very close to the “exact” ones provided by the GBT-based buckling analyses. Indeed, the average and maximum errors are (ii₁) 2.7% and 4.6%, for **P4** with $L_{cr-LD}^{\min.}=424.7 < L < 1000cm$, (ii₂) 5.0% and 8.1%, for **P3** with $L_{cr-LD}^{\min.}=314.4 < L < 1000cm$, (ii₃) 1.3% and 5.5%, for **S1** with $L_{cr-D}^{\min.}=38.9 < L < 300cm$ and (ii₄) 0.1% and 2.2%, for **S0** with $L_{cr-D}^{\min.}=44.7 < L < 169.4cm$.
- (iii) The GBT-based formulae are shown to be accurate for purlins with $K_{TG}^I = \infty$ and $0 \lesssim K_R^I \leq \infty$, and for studs with $K_{TG}^I, K_{TN}^I, K_R^I \geq 0$. However, it is also possible to capture adequately quite the lateral-torsional buckling behavior of purlins **P1** using restraints $K_{TG}^I = \infty$ and $K_R^I \cong 0$ (*e.g.*, 0.001) – as shown in Fig. 21, the average error is 1.1% (recall that, for $K_{TG}^I = \infty$ and $K_R^I = 0$, the lateral-torsional mode is not defined by the eigenvalue problem given in Eq. (28)).

5. Conclusion

This paper reported the development, numerical implementation and practical application of a novel/improved approach to perform GBT-based buckling analyses of restrained cold-formed steel members. This approach differs from the conventional one in the characteristics of the cross-section analysis, which incorporates the elastic restraints – therefore, its output is a set of constrained deformation modes.

After deriving the GBT equilibrium equation system incorporating the elastic restraints/springs), the concepts and procedures involved in determining the constrained deformation modes were described and illustrated. Next, the capabilities and potential of the proposed GBT-based to analyze the buckling behavior of (i) purlins restrained by sheeting and (ii) studs sheathed by panels were illustrated in great detail – for various restraint arrangements, it was investigated how the critical buckling moment/load and mode shape vary with the purlin/stud length. For validation and assessment purposes, several results obtained with the proposed GBT-based approach were compared with values yielded by the programs GBTUL2.0 (conventional GBT), CUFSM (finite strip method) and/or ANSYS (shell finite elements) – an excellent agreement was invariably found.

Finally, it was also shown that using constrained deformation modes makes it possible to derive semi-analytical formulae that provide very accurate estimates of the critical lengths and bifurcation moments/loads of (i) restrained purlins buckling in lateral-distortional modes and (ii) sheathed studs buckling in distortional modes. The accuracy assessment of the semi-analytical formulae was made by comparing their estimates with the “exact” results yielded by GBT buckling analyses based on constrained deformation modes.

Out of the various findings reported in this work, the following ones deserve to be highlighted:

- (i) The proposed GBT-based approach to analyze the buckling behavior of restrained cold-formed steel members was found to be computationally more efficient than the conventional one. In particular, it is possible to obtain accurate buckling results with less deformation modes (often just a single one).
- (ii) The constrained deformation modes provide much more insightful information about the restrained member mechanics than their unconstrained counterparts – this is true even before the member buckling analysis is performed.
- (iii) GBT-based semi-analytical formulae were derived to estimate the lateral-distortional buckling behavior of restrained purlins and the distortional buckling behavior of sheathed studs. These formulae were found to consistently yield accurate critical length and bifurcation moment/load estimates – indeed, in the overwhelming majority of cases analyzed, the error did not exceed 2.5%.

Acknowledgements

The first two authors acknowledge the financial support provided by (i) the CAPES Foundation, Ministry of Education of Brazil, through scholarship n° 88887.597170/2021-00 (Heitor Araujo), and (ii) Conselho Nacional de Desenvolvimento Científico e Tecnológico (CNPq – Ministry of Science, Technology and Innovation of Brazil), through project n° 309963/2019-2 (Cilmar Basaglia).

References

- Ádány S, Schafer BW (2008). A full modal decomposition of thin-walled, singlebranched open cross-section members via the constrained Finite Strip Method, *Journal of Constructional Steel Research*, **64**(1), 12-29.
- AIISI (American Iron and Steel Institute) (2016). *North American Specification (NAS) for the Design of Cold-Formed Steel Structural Members* (AIISI-S100-16) + respective *Commentary*, Washington DC.

- Basaglia C, Camotim D, Gonçalves R, Graça A (2013). GBT-based assessment of the buckling behaviour of cold-formed steel purlins restrained by sheeting, *Thin Walled Structures*, **72**(November), 217-229.
- Bebiano R, Camotim D, Gonçalves R (2010). GBTUL 2.0 – A second-generation code for the GBT-based buckling and vibration analysis of thin-walled members, *Thin Walled Structures*, **124** (March), 235-257.
- Bebiano R, Gonçalves R, Camotim D (2015). A cross-section analysis procedure to rationalise and automate the performance of GBT-based structural analyses, *Thin Walled Structures*, **92**(July), 29-47.
- Bebiano R, Eisenberger M, Camotim D, Gonçalves R (2018a). GBT-based vibration analysis using the Exact Element Method, *International Journal of Structural Stability and Dynamics*, **18**(5), paper 1850068 (31 pages).
- Bebiano R, Basaglia C, Camotim D, Gonçalves R (2018b). GBT buckling analysis of generally loaded thin-walled members with arbitrary flat-walled cross-sections, *Thin Walled Structures*, **123**(February), 11-24.
- Cai J, Moen CD (2016). Elastic buckling analysis of thin-walled structural members with rectangular holes using Generalized Beam Theory, *Thin Walled Structures*, **107**(October), 274-286.
- Camotim D, Silvestre N, Basaglia C, Bebiano R (2008). GBT-based buckling analysis of thin-walled members with non-standard support conditions, *Thin Walled Structures*, **46**(7-9), 800-815.
- Camotim D, Basaglia C, Bebiano R, Gonçalves R, Silvestre N (2010). Latest developments in the GBT analysis of thin-walled steel structures, *Proceedings of International Colloquium on Stability and Ductility of Steel Structures Stability (SDSS'Rio – Rio de Janeiro, 8-10/9)*, E. Batista, P. Vellasco, L. Lima (eds.), 33-58.
- Camotim D, Basaglia C (2013). Buckling analysis of thin-walled structures using Generalised Beam Theory (GBT): state-of-the-art report, *Steel Construction*, **6**(2), 117-131.
- Camotim D., Dinis P.B., Martins A.D. (2016). Direct Strength Method (DSM) – a general approach for the design of cold-formed steel structures, *Recent Trends in Cold-Formed Steel Construction*, C. Yu (ed.), Woodhead Publishing (Series in Civil and Structural Engineering), Amsterdam, 69-105.
- Casafont M, Marimon F, Pastor MM, Ferrer M (2011). Linear buckling analysis of thin-walled members combining the Generalised Beam Theory and the Finite Element Method, *Computers and Structures*, **89**(21-22), 1982-2000.
- Dinis PB, Camotim D, Silvestre N (2006). GBT formulation to analyse the buckling behaviour of thin-walled members with arbitrarily “branched” open cross-sections, *Thin Walled Structures*, **44**(1), 20-38.
- Duan L, Zhao J (2019). GBT deformation modes for thin-walled cross-sections with circular rounded corner, *Thin Walled Structures*, **136**(March), 64-89.
- Gao T, Moen CD (2012). Predicting rotational restraint provided to wall girts and roof purlins by through-fastened metal panels, *Thin Walled Structures*, **61**(December), 145-153.
- Gao T, Moen CD (2014). Extending the Direct Strength Method for cold-formed steel design to through-fastened simple span girts and purlins with laterally unbraced compression flanges, *Journal of Structural Engineering (ASCE)*, **140**(6), paper 04014010 (12 pages).
- Gonçalves R, Ritto-Corrêa M, Camotim D (2010). - A new approach to the calculation of cross-section deformation modes in the framework of Generalized Beam Theory, *Computational Mechanics*, **46**(5), 759-781
- Gypsum Association (2019). *Gypsum Board Typical Mechanical and Physical Properties*, Report GA-235-2019, Silver Spring, MD.
- Heinz DA (1994). Application of Generalized Beam Theory to the design of thin-walled purlins, *Thin Walled Structures*, **19**(2-4), 311-335.
- Jiang C, Davies JM (1997). Design of thin-walled purlins for distortional buckling, *Thin Walled Structures*, **29**(1-4), 189-202.
- Jiang C, Leach P, Davies JM (1994). The analysis of restrained purlins using Generalised Beam Theory, *Proceedings of 12th International Specialty Conference on Cold-Formed Steel Structures* (St. Louis, 18-19/10), W.W. Yu, R. LaBoube (eds.), 109-120.
- Ings NL, Trahair NS (1984). Lateral buckling of restrained roof purlins, *Thin Walled Structures*, **2**(4), 285-306.
- Li Z, Schafer BW (2010). Application of the finite strip method in cold-formed steel member design, *Journal of Constructional Steel Research*, **66**(8-9), 971-980.
- Lucas RM, Al-Bermani A, Kitipornchai S (1997). Modelling of cold-formed purlin-sheeting systems – Part 2: simplified model, *Thin Walled Structures*, **27**(4), 263-286.
- Lendvai A, Joó A, Dunai L (2018). Experimental full-scale tests on steel portal frames for development of diaphragm action – Part I: experimental results, *Thin Walled Structures*, **132**(November), 729-739.
- Miranda S, Madeo A, Melchionda D, Ubertini F (2015). A high-performance flexibility based GBT finite element, *Computers and Structures*, **158**(October), 285-307.
- Muresan A, Nedelcu M, Gonçalves R (2019). GBT-based FE formulation to analyse the buckling behaviour of isotropic conical shells with circular cross-sections, *Thin Walled Structures*, **134**(January), 84-101.
- Ren C, Zhao X, Chen Y (2016). Buckling behaviour of partially restrained cold-formed steel zed purlins subjected to transverse distributed uplift loading, *Engineering Structures*, **114**(May), 14-24.

- SAS (Swanson Analysis Systems Inc.) (2013). *ANSYS Reference Manual* (version 15).
- Schafer BW (2013). *Sheathing Braced Design of Wall Studs*, Research Report RP13-1, American Iron and Steel Institute (AISI), Washington, DC.
- Schafer B.W. (2019). Advances in the Direct Strength Method of cold-formed steel design, *Thin-Walled Structures*, **140**(July), 533-541.
- Schardt R. (1989). *Verallgemeinerte Technische Biegetheorie*, Springer-Verlag, Berlin. (German).
- Schardt R (1994). Generalized beam theory – an adequate method for coupled stability problems, *Thin Walled Structures*, **19**(2-4), 161-180.
- Selvaraj S, Madhavan M (2018). Improvements in AISI design methods for gypsum-sheathed cold-formed steel wall panels subjected to bending, *Journal of Structural Engineering* (ASCE), **145**(2), paper 04018243 (18 pages).
- Silva TG, Basaglia C, Camotim D (2019). On the incorporation of cross-section restraints in Generalised Beam Theory (GBT), *USB Proceedings of the International Colloquium on Stability and Ductility of Steel Structures* (SDSS 2019 – Prague, 11-13/9), F. Wald, M. Jandera (eds.), paper 213.
- Silvestre N, Camotim D (2002). First-order generalised beam theory for arbitrary orthotropic materials, *Thin Walled Structures*, **40**(9), 755-789.
- Silvestre N, Camotim D (2003). GBT buckling analysis of pultruded FRP lipped channel members, *Computers and Structures*, **81**(18-19), 1889-1904.
- Silvestre N, Camotim D (2004a). Distortional buckling formulae for cold-formed steel C and Z-section members: Part I – derivation, *Thin Walled Structures*, **42**(11), 1567-1597.
- Silvestre N, Camotim D (2004b). Distortional buckling formulae for cold-formed steel C and Z-section members: Part II – validation and application, *Thin Walled Structures*, **42**(11), 1599-1629.
- Silvestre N, Camotim D (2004c). Distortional buckling formulae for cold-formed steel rack-section members, *Steel & Composite Structures*, **4**(1), 49-75.
- Sonkar C, Mittal AK, Brattacharyya SK (2020). Comparative study on cold-formed steel single-stud and multiple-studs wall panels with magnesium oxide sheathing under axial loading: experimental and analytical, *Journal of Structural Engineering* (ASCE), **146**(11), paper 04020224 (22 pages).
- Soroushian P, Peköz T (1982). Behavior of C- and Z-purlins under wind uplift, *Proceedings of 6th International Specialty Conference on Cold-Formed Steel Structures* (St. Louis, 16-17/11), University of Missouri-Rolla, 409-429.
- Taig G, Ranzi G (2014). Generalised Beam Theory (GBT) for stiffened sections, *International Journal of Steel Structures*, **14**(July), 381-397.
- Taig G, Ranzi G (2015). Generalised Beam Theory (GBT) for composite beams with partial shear interaction, *Engineering Structures*, **99**(September), 582-602.
- Vieira Jr. LCM (2011). *Behavior and Design of Sheathed Cold-Formed Steel Stud Walls under Compression*, Ph.D. Thesis in Civil Engineering, Johns Hopkins University, Baltimore, Maryland.
- Vieira Jr. LCM, Schafer BW (2013). Behavior and design of sheathed cold-formed steel stud walls under compression, *Journal of Structural Engineering* (ASCE), **139**(5), 772-786.
- Yuan W, Cheng S, Li L, Kim B (2014). Web-flange distortional buckling of partially restrained cold-formed steel purlins under uplift loading, *International Journal of Mechanical Sciences*, **89**(December), 476-481.
- Zhu J, Qian S, Li L (2017). Dynamic instability of laterally-restrained zed-purlin beams under uplift loading, *International Journal of Mechanical Sciences*, **131-132**(October), 408-413.

Annex A – Matrices involved in the definition of the auxiliary eigenvalue problem

The auxiliary eigenvalue problem (see Eq. (28)) is defined by means of the expressions providing the non-null matrix components, which read

(i) Symmetric flexibility matrix \mathbf{F} :

$$F_{11} = F_{22} = F_{55} = F_{66} = 1 \quad F_{33} = F_{44} = \frac{b_w}{3K} \cdot (\alpha_f + 1) \quad F_{34} = \frac{b_w}{6K} \quad (\text{A.1})$$

(ii) Wall relative rotation matrix $\ddot{\mathbf{w}}$:

$$\begin{aligned} \ddot{w}_{31} &= \frac{1}{b_w^2 \alpha_f} \frac{1}{\beta_s} & \ddot{w}_{32} &= \frac{1}{b_w^2 \alpha_f} \left(-1 - \frac{1}{\beta_s} - \frac{1}{\beta_f} \right) & \ddot{w}_{33} &= \frac{1}{b_w^2 \alpha_f} \left(2 + \frac{1}{\beta_f} \right) \\ \ddot{w}_{34} &= \frac{1}{b_w^2 \alpha_f} (-1 - \rho) & \ddot{w}_{35} &= \frac{1}{b_w^2 \alpha_f} \rho \\ \ddot{w}_{42} &= \rho \ddot{w}_{35} & \ddot{w}_{43} &= \rho \ddot{w}_{34} & \ddot{w}_{44} &= \rho \ddot{w}_{33} & \ddot{w}_{45} &= \rho \ddot{w}_{32} & \ddot{w}_{46} &= \rho \ddot{w}_{31} \end{aligned} \quad (\text{A.2})$$

where $\rho = 1$ (lipped channel cross-section) or $\rho = -1$ (zed-section).

(iii) Symmetric lateral/tangential translational spring stiffness matrix \mathbf{K}_Z :

$$K_{Z_{22}} = -K_{Z_{23}} = K_{Z_{33}} = \frac{K_{TG}^I}{(b_w \alpha_f)^2} \quad K_{Z_{44}} = -K_{Z_{45}} = K_{Z_{55}} = \frac{K_{TG}^{II}}{(b_w \alpha_f)^2} \quad (\text{A.3})$$

(iv) Symmetric out-of-plane vertical/normal translational spring stiffness matrix \mathbf{K}_Y :

$$\begin{aligned} K_{Y_{11}} &= \frac{1}{2b_w^2} \frac{K_{TN}^I}{2\beta_\ell^2} & K_{Y_{12}} &= \frac{1}{2b_w^2} \left(-\frac{K_{TN}^I}{2\beta_\ell \beta_f} - \frac{K_{TN}^I}{2\beta_\ell^2} \right) \\ K_{Y_{13}} &= \frac{1}{2b_w^2} \left(-\frac{K_{TN}^I}{2\beta_\ell} + \frac{K_{TN}^I}{2\beta_\ell \beta_f} \right) & K_{Y_{14}} &= \frac{1}{2b_w^2} \left(\frac{K_{TN}^I}{2\beta_\ell} \right) \\ K_{Y_{22}} &= \frac{1}{2b_w^2} \left(\frac{K_{TN}^I}{2\beta_f^2} + \frac{K_{TN}^I}{\beta_f \beta_s} + \frac{K_{TN}^I}{2\beta_\ell^2} \right) & K_{Y_{23}} &= \frac{1}{2b_w^2} \left(\frac{K_{TN}^I}{2\beta_f} + \frac{K_{TN}^I}{2\beta_\ell} - \frac{K_{TN}^I}{2\beta_f^2} - \frac{K_{TN}^I}{2\beta_\ell \beta_f} \right) \\ K_{Y_{24}} &= \frac{1}{2b_w^2} \left(-\frac{K_{TN}^I}{2\beta_\ell} - \frac{K_{TN}^I}{2\beta_f} \right) \\ K_{Y_{33}} &= \frac{1}{2b_w^2} \left(\frac{K_{TN}^I}{2} - \frac{K_{TN}^I}{\beta_f} + \frac{K_{TN}^I}{2\beta_f^2} + \frac{K_{TN}^{II}}{2} \right) & K_{Y_{34}} &= \frac{1}{2b_w^2} \left(-\frac{K_{TN}^I}{2} + \frac{K_{TN}^I}{2\beta_f} - \frac{K_{TN}^{II}}{2} + \frac{K_{TN}^{II}}{2\beta_f} \right) \\ K_{Y_{35}} &= \frac{1}{2b_w^2} \left(-\frac{K_{TN}^{II}}{2\beta_f} - \frac{K_{TN}^{II}}{2\beta_\ell} \right) & K_{Y_{36}} &= \frac{1}{2b_w^2} \left(\frac{K_{TN}^{II}}{2\beta_\ell} \right) \\ K_{Y_{44}} &= \frac{1}{2b_w^2} \left(\frac{K_{TN}^{II}}{2} - \frac{K_{TN}^{II}}{\beta_f} + \frac{K_{TN}^{II}}{2\beta_f^2} + \frac{K_{TN}^I}{2} \right) & K_{Y_{45}} &= \frac{1}{2b_w^2} \left(\frac{K_{TN}^{II}}{2\beta_f} + \frac{K_{TN}^{II}}{2\beta_\ell} - \frac{K_{TN}^{II}}{2\beta_f^2} - \frac{K_{TN}^{II}}{2\beta_\ell \beta_f} \right) \end{aligned}$$

$$\begin{aligned}
K_{Y_{46}} &= \frac{1}{2b_w^2} \left(-\frac{K_{TN}^{II}}{2\beta_\ell} + \frac{K_{TN}^{II}}{2\beta_\ell\beta_f} \right) \\
K_{Y_{55}} &= \frac{1}{2b_w^2} \left(\frac{K_{TN}^{II}}{2\beta_f^2} + \frac{K_{TN}^{II}}{\beta_f\beta_\ell} + \frac{K_{TN}^{II}}{2\beta_\ell^2} \right) & K_{Y_{56}} &= \frac{1}{2b_w^2} \left(-\frac{K_{TN}^{II}}{2\beta_\ell^2} - \frac{K_{TN}^{II}}{2\beta_\ell\beta_f} \right) \\
K_{Y_{66}} &= \frac{1}{2b_w^2} \frac{K_{TN}^{II}}{2\beta_\ell^2}
\end{aligned} \tag{A.4}$$

(v) Symmetric rotational spring stiffness matrix \mathbf{K}_R :

$$\begin{aligned}
K_{R_{11}} &= \frac{1}{b_w^4\alpha_f^2} \frac{K_R^I}{\beta_\ell^2} & K_{R_{12}} &= \frac{1}{b_w^4\alpha_f^2} \left(-\frac{K_R^I}{\beta_\ell^2} - \frac{K_R^I}{\beta_\ell\beta_f} \right) & K_{R_{13}} &= \frac{1}{b_w^4\alpha_f^2} \left(\frac{K_R^I}{\beta_\ell} + \frac{K_R^I}{\beta_\ell\beta_f} \right) \\
K_{R_{14}} &= \frac{1}{b_w^4\alpha_f^2} \left(-\frac{K_R^I}{\beta_\ell} \right) \\
K_{R_{22}} &= \frac{1}{b_w^4\alpha_f^2} \left(\frac{K_R^I}{\beta_\ell^2} + \frac{2K_R^I}{\beta_\ell\beta_f} + \frac{K_R^I}{\beta_f^2} \right) & K_{R_{23}} &= \frac{1}{b_w^4\alpha_f^2} \left(-\frac{K_R^I}{\beta_\ell} - \frac{K_R^I}{\beta_\ell\beta_f} - \frac{K_R^I}{\beta_f} - \frac{K_R^I}{\beta_f^2} \right) \\
K_{R_{24}} &= \frac{1}{b_w^4\alpha_f^2} \left(\frac{K_R^I}{\beta_\ell} + \frac{K_R^I}{\beta_f} \right) \\
K_{R_{33}} &= \frac{1}{b_w^4\alpha_f^2} \left(K_R^I + \frac{2K_R^I}{\beta_f} + \frac{K_R^I}{\beta_f^2} + K_R^{II} \right) & K_{R_{34}} &= \frac{1}{b_w^4\alpha_f^2} \left(-K_R^I - \frac{K_R^I}{\beta_f} - \frac{K_R^{II}}{\beta_f} - K_R^{II} \right) \\
K_{R_{35}} &= \frac{1}{b_w^4\alpha_f^2} \left(\frac{K_R^{II}}{\beta_\ell} + \frac{K_R^{II}}{\beta_f} \right) & K_{R_{36}} &= \frac{1}{b_w^4\alpha_f^2} \left(-\frac{K_R^{II}}{\beta_\ell} \right) \\
K_{R_{44}} &= \frac{1}{b_w^4\alpha_f^2} \left(K_R^{II} + \frac{2K_R^{II}}{\beta_f} + \frac{K_R^{II}}{\beta_f^2} + K_R^I \right) & K_{R_{45}} &= \frac{1}{b_w^4\alpha_f^2} \left(-\frac{K_R^{II}}{\beta_\ell} - \frac{K_R^{II}}{\beta_\ell\beta_f} - \frac{K_R^{II}}{\beta_f} - \frac{K_R^{II}}{\beta_f^2} \right) \\
K_{R_{46}} &= \frac{1}{b_w^4\alpha_f^2} \left(\frac{K_R^{II}}{\beta_\ell} + \frac{K_R^{II}}{\beta_\ell\beta_f} \right) \\
K_{R_{55}} &= \frac{1}{b_w^4\alpha_f^2} \left(\frac{K_R^{II}}{\beta_\ell^2} + \frac{2K_R^{II}}{\beta_\ell\beta_f} + \frac{K_R^{II}}{\beta_f^2} \right) & K_{R_{56}} &= \frac{1}{b_w^4\alpha_f^2} \left(-\frac{K_R^{II}}{\beta_\ell^2} - \frac{K_R^{II}}{\beta_\ell\beta_f} \right) \\
K_{R_{66}} &= \frac{1}{b_w^4\alpha_f^2} \frac{K_R^{II}}{\beta_\ell^2}
\end{aligned} \tag{A.5}$$

(vi) Symmetric warping stiffness matrix \mathbf{C} :

$$\begin{aligned}
C_{11} = C_{66} = 2C_{12} = 2C_{56} &= \frac{E b_w t}{3} \alpha_s & C_{22} = C_{55} &= \frac{E b_w t}{3} (\alpha_s + \alpha_f) \\
C_{33} = C_{44} &= \frac{E b_w t}{3} (\alpha_f + 1) & C_{23} = C_{45} &= \frac{E b_w t}{6} \alpha_f & C_{34} &= \frac{E b_w t}{6}
\end{aligned} \tag{A.6}$$

Annex B – Modal properties involved in the determination of buckling parameter estimates

The determination of the buckling moment/load parameter estimates (see Eqs. (22)-(23)) requires expressions providing the modal displacements and rotations, and modal mechanical and geometrical properties, which read

- (i) Cross-section in-plane displacements ($v_{p,r-LD}$ or $v_{p,r-D}$), rotations ($\theta_{p,r-LD}$ or $\theta_{p,r-D}$) and flexural displacements ($w_{p,r-LD}$ or $w_{p,r-D}$):

$$v_{p,1} = \frac{u_1 - u_2}{b_w \alpha_\ell} \quad v_{p,2} = \frac{u_2 - u_3}{b_w \alpha_f} \quad v_{p,3} = \frac{u_3 - u_4}{b_w} \quad v_{p,4} = \frac{u_4 - u_5}{b_w \alpha_f} \quad v_{p,5} = \frac{u_5 - u_6}{b_w \alpha_\ell} \quad (B.1)$$

$$\theta_{p,1} = \theta_{p,2} + \frac{\alpha_f b_w m_3}{6K} \quad \theta_{p,2} = \frac{1}{b_w \alpha_f} \left(-\frac{v_{p,1}}{\sin(\phi)} + \frac{v_{p,2}}{\tan(\phi)} - v_{p,3} \right) \quad \theta_{p,3} = -\frac{1}{b_w} (v_{p,2} + \rho v_{p,4})$$

$$\theta_{p,4} = \frac{\rho}{b_w \alpha_f} \cdot \left(-\frac{v_{p,5}}{\sin(\phi)} + \frac{v_{p,4}}{\tan(\phi)} - v_{p,3} \right) \quad \theta_{p,5} = \theta_{p,4} - \frac{\alpha_f b_w m_4}{6K} \quad (B.2)$$

$$w_{p,1} = -\frac{\alpha_\ell b_w \theta_{p,1}}{2} - \frac{v_{p,2}}{\sin(\phi)} + \frac{v_{p,1}}{\tan(\phi)} \quad w_{p,2} = \frac{1}{2} \left(\frac{v_{p,1}}{\sin(\phi)} - \frac{v_{p,2}}{\tan(\phi)} - v_{p,3} \right) \quad w_{p,3} = \frac{v_{p,2} - \rho v_{p,4}}{2}$$

$$w_{p,4} = \frac{\rho}{2} \left(-\frac{v_{p,5}}{\sin(\phi)} + \frac{v_{p,4}}{\tan(\phi)} + v_{p,3} \right) \quad w_{p,5} = \frac{\alpha_\ell b_w \theta_{p,5}}{2} + \frac{\rho v_{p,4}}{\sin(\phi)} - \frac{\rho v_{p,5}}{\tan(\phi)} \quad (B.3)$$

where $\rho=1$, for lipped channel cross-section, and $\rho=-1$, for Zed-section.

- (ii) Cross-section modal mechanical properties C_{LD} , B_{LD} , D_{LD} or C_D , B_D , D_D :¹⁷.

$$C_k = \frac{E t b_w}{3} \left[\alpha_\ell (u_1^2 + u_1 u_2 + u_2^2 + u_5^2 + u_5 u_6 + u_6^2) + \alpha_f (u_2^2 + u_2 u_3 + u_3^2 + u_4^2 + u_4 u_5 + u_5^2) + (u_3^2 + u_3 u_4 + u_4^2) \right] \quad (B.4)$$

$$B_k = \frac{b_w}{3 \cdot K} \left[\alpha_f (m_3^2 + m_4^2) + m_3^2 + m_3 m_4 + m_4^2 \right] + K_{TG}^I v_{p,2}^2 + K_{TG}^{II} v_{p,4}^2 + K_{TN}^I w_{p,2}^2 + K_{TN}^{II} w_{p,4}^2 + K_R^I \theta_{p,2}^2 + K_R^{II} \theta_{p,4}^2 \quad (B.5)$$

$$D_k = \frac{G \cdot t^3 \cdot b_w}{3} \left[\alpha_\ell (\theta_{p,1}^2 + \theta_{p,5}^2) + \alpha_f (\theta_{p,2}^2 + \theta_{p,4}^2) + \theta_{p,3}^2 \right] \quad (B.6)$$

- (iii) Cross-section modal geometrical properties ${}^P X_{LD}$ and ${}^S X_D$:

$${}^P X_k = \frac{b_w t}{30240 K^2 I_{Z'}} (X_k^I + X_k^{II} + X_k^{III} + X_k^{IV} + X_k^V) \quad (B.7)$$

$${}^S X_k = \frac{b_w t}{30240 K^2 A} (X_k^I + X_k^{II} + X_k^{III} + X_k^{IV} + X_k^V) \quad (B.8)$$

¹⁷ When comparing Eqs. (B.4) and (B.6) with Eqs. (5) and (7), note that (i) C_k only contains the warping membrane component o and (ii) D_k only takes into account the rotation of each wall element – as shown in [46-48], this simplification does not compromise the accuracy of the results.

with

$$I_{Z'} = \frac{b_w t}{12} (b_w^2 (1 + 6\alpha_f + 2\alpha_\ell (4\beta_\ell^2 - 6\beta_\ell + 3)) + 2t^2 (\alpha_f + \alpha_\ell - \beta_\ell \sin \phi)) \quad (\text{B.9})$$

$$A = b_w t (1 + 2\alpha_\ell + 2\alpha_f) \quad (\text{B.10})$$

$$\begin{aligned} X_k^I &= 15120 K^2 \left\{ \alpha_\ell [(v_{p,1}^2 + w_{p,1}^2)(^jU_1 + ^jU_2) + (v_{p,5}^2 + w_{p,5}^2)(^jU_5 + ^jU_6)] + \right. \\ &\quad \left. + \alpha_f [(v_{p,2}^2 + w_{p,2}^2)(^jU_2 + ^jU_3) + (v_{p,4}^2 + w_{p,4}^2)(^jU_4 + ^jU_5)] + \right. \\ &\quad \left. + (v_{p,3}^2 + w_{p,3}^2)(^jU_3 + ^jU_4) \right\} \\ X_k^{II} &= 1260 K^2 b_w^2 \left\{ \alpha_\ell^3 [\theta_{p,1}^2 (^jU_1 + ^jU_2) + \theta_{p,5}^2 (^jU_5 + ^jU_6)] + \right. \\ &\quad \left. + \alpha_f^3 [\theta_{p,2}^2 (^jU_2 + ^jU_3) + \theta_{p,4}^2 (^jU_4 + ^jU_5)] + \theta_{p,3}^2 (^jU_3 + ^jU_4) \right\} \\ X_k^{III} &= 5040 K^2 b_w \left\{ \alpha_\ell^2 [\theta_{p,1} w_{p,1} (^jU_2 - ^jU_1) + \theta_{p,5} w_{p,5} (^jU_6 - ^jU_5)] \right. \\ &\quad \left. + \alpha_f^2 [\theta_{p,2} w_{p,2} (^jU_3 - ^jU_2) + \theta_{p,4} w_{p,4} (^jU_5 - ^jU_4)] + \theta_{p,3} w_{p,3} (^jU_4 - ^jU_3) \right\} \\ X_k^{IV} &= b_w^4 \left\{ m_3^2 [\alpha_f^5 (29^jU_2 + 35^jU_3) + 29^jU_4 + 35^jU_3] + \right. \\ &\quad \left. + m_4^2 [\alpha_f^5 (29^jU_5 + 35^jU_4) + 29^jU_3 + 35^jU_4] + 62m_3 m_4 (^jU_3 + ^jU_4) \right\} \\ {}^jX_k^V &= 84 K b_w^2 \left\{ \alpha_f^3 [m_3 w_{p,2} (16^jU_3 + 14^jU_2) + m_4 w_{p,4} (16^jU_4 + 14^jU_5)] + \right. \\ &\quad + w_{p,3} [m_3 (16^jU_3 + 14^jU_4) + m_4 (16^jU_4 + 14^jU_3)] + \\ &\quad + b_w [\alpha_f^4 (m_3 \theta_{p,2} (2^jU_3 - ^jU_2) + m_4 \theta_{p,4} (^jU_5 - 2^jU_4) + \\ &\quad + \theta_{p,3} (m_3 (^jU_4 - 2^jU_3) + m_4 (2^jU_4 - ^jU_3))] \end{aligned} \quad (\text{B.11})$$

where (i) $I_{Z'}$ is the cross-section moment of inertia about the centroidal normal to the web (Z' -axis – see Fig. 19), (ii) A is the cross-section area and (iii) jU_i are the nodal axial displacements due to applied load, given by

$$^P U_1 = -^P U_6 = -b_w (0.5 - \beta_\ell) \quad {}^P U_2 = {}^P U_3 = -^P U_4 = -^P U_5 = -0.5 b_w \quad {}^S U_{1-6} = 1 \quad (\text{B.12})$$

Annex C – Listing of the Python program implementing the LD and D buckling formulae

Below is the listing of the Python program written to implement the LD and D buckling formulae addressed in Section 4. All the comments appearing in **bold** are intended to help the reader grasp the meaning of the various executable instructions of the program.

```

from math import *
import numpy as np
# Section Properties – Data Input
SM = "S" # Member type: "S" for studs or "P" for purlins
# [web width, flange width, lip width, thickness, lip inclination (degrees)]
bw = 9.84; bf = 7.84; bl = 0.92; t = 0.16; phi = 90;
E = 20500; nu = 0.3; rho = 1 # Cross-section shape factor: 1 (C) or -1 (Z)
# Restraint Values – Data Input
# [upper flange]
KtgI = 0.169061592; KtnI = 0.001056672; KrI = 1.033360968;
# [lower flange]
KtgII = 0.109888425; KtnII = 2.98516E-05; KrII = 0.354800418;
# Task I – Definition of the Auxiliary Eigenvalue Problem
# (I.i) Definition of the geometrical and mechanical parameters - Eq.(24)
alphal = bl/bw; alphaf = bf/bw; betal = alphal*sin(phi*pi/180);
betaf = alphaf*tan(phi*pi/180)
K = E*t**3/(12*(1-nu**2)); G = E/(2*(1+nu));
# (I.ii) Determination of the transverse bending moment matrix
# (Annex A.i) Symmetric flexibility matrix F - Eq. (A.1)
F = np.zeros([6, 6])
F[0, 0] = F[1, 1] = F[4, 4] = F[5, 5] = 1
F[2, 2] = F[3, 3] = bw/(3*K)*(alphaf+1)
F[2, 3] = F[3, 2] = bw/(6*K)
# (Annex A.ii) Wall relative rotation matrix ww - Eq. (A.2)
ww = np.zeros([6, 6])
ww[2, 0] = 1/(bw**2*alphaf)*1/betal; ww[3, 5] = rho*ww[2, 0];
ww[2, 1] = 1/(bw**2*alphaf)*(-1/betal-1/betaf-1);
ww[3, 4] = rho*ww[2, 1]; ww[2, 2] = 1/(bw**2*alphaf)*(2+1/betaf);
ww[3, 3] = rho*ww[2, 2]; ww[2, 3] = 1/(bw**2*alphaf)*(-1-rho);
ww[3, 2] = rho*ww[2, 3]; ww[2, 4] = 1/(bw**2*alphaf)*rho;
ww[3, 1] = rho*ww[2, 4];
# Stif = transverse stiffness matrix
Stif = np.linalg.inv(F)
# Determination of the transverse bending moment matrix - Eq. (25)
M = np.matmul(-Stif, ww)
# (I.iii) Bf matrix wall transverse bending stiffness - Eq. (26)
Bf = np.matmul(-np.transpose(ww), M)
# (I.iv) Determination of the elastic spring matrix
# (Annex A.iii) Tangential spring stiffness matrix KZ - Eq. (A.3)
Kz = np.zeros([6, 6])
Kz[1, 1] = Kz[2, 2] = KtgI/(bw*alphaf)**2;
Kz[3, 3] = Kz[4, 4] = KtgII/(bw*alphaf)**2;
Kz[2, 1] = Kz[1, 2] = -KtgI/(bw*alphaf)**2;
Kz[3, 4] = Kz[4, 3] = -KtgII/(bw*alphaf)**2
# (Annex A.iv) Translational spring stiffness matrix KY - Eq. (A.4)
Ky = np.zeros([6, 6])
Ky[0, 0] = 1/(2*bw**2)*(KtnI/(2*betal**2))
Ky[1, 1] = 1/(2*bw**2)*(KtnI/(2*betal**2)+
    KtnI/(betal*betaf)+KtnI/(2*betal**2))
Ky[2, 2] = 1/(2*bw**2)*(KtnI/(2)-KtnI/(betaf)+KtnI/(2*betal**2)+KtnII/(2))
Ky[3, 3] = 1/(2*bw**2)*(KtnII/(2)-KtnII/(betaf)+
    KtnII/(2*betal**2)+KtnI/(2))
Ky[4, 4] = 1/(2*bw**2)*(KtnII/(2*betal**2)+KtnII/(betal*betaf)+
    KtnII/(2*betal**2))
Ky[5, 5] = 1/(2*bw**2)*(KtnII/(2*betal**2))
Ky[0, 1] = Ky[1, 0] = 1/(2*bw**2)*(-KtnI/(2*betal*betaf)-KtnI/(2*betal**2))
Ky[0, 2] = Ky[2, 0] = 1/(2*bw**2)*(-KtnI/(2*betal)+KtnI/(2*betal*betaf))

```

```

Ky[0, 3] = Ky[3, 0] = 1/(2*bw**2)*(KtnI/(2*betal))
Ky[1, 2] = Ky[2, 1] = 1/(2*bw**2)*(KtnI/(2*betaf)+KtnI/(2*betal) -
    KtnI/(2*betaf**2)-KtnI/(2*betal*betaf))
Ky[1, 3] = Ky[3, 1] = 1/(2*bw**2)*(-KtnI/(2*betal)-KtnI/(2*betaf))
Ky[2, 3] = Ky[3, 2] = 1/(2*bw**2)*(-KtnI/2+KtnI/(2*betaf)-
    KtnII/2+KtnII/(2*betaf))
Ky[2, 4] = Ky[4, 2] = 1/(2*bw**2)*(-KtnII/(2*betaf)-KtnII/(2*betal))
Ky[2, 5] = Ky[5, 2] = 1/(2*bw**2)*(KtnII/(2*betal))
Ky[3, 4] = Ky[4, 3] = 1/(2*bw**2)*(KtnII/(2*betaf)+KtnII/(2*betal) -
    KtnII/(2*betaf**2)-KtnII/(2*betal*betaf))
Ky[3, 5] = Ky[5, 3] = 1/(2*bw**2)*(-KtnII/(2*betal)+KtnII/(2*betal*betaf))
Ky[4, 5] = Ky[5, 4] = 1/(2*bw**2)*(-KtnII/(2*betal**2)-
    KtnII/(2*betal*betaf))

# (Annex A.v) Rotational spring stiffness matrix KR - Eq. (A.5)
Kr = np.zeros([6, 6])
Kr[0, 0] = 1/(bw**4*alphaf**2)*(KrI/(betal**2))
Kr[1, 1] = 1/(bw**4*alphaf**2)*(KrI/betal**2+(2*KrI/(betaf*betal))+
    KrI/betaf**2)
Kr[2, 2] = 1/(bw**4*alphaf**2)*(KrI+(2*KrI/(betaf))+KrI/betaf**2+KrII)
Kr[3, 3] = 1/(bw**4*alphaf**2)*(KrII+(2*KrII/(betaf))+KrII/betaf**2+KrI)
Kr[4, 4] = 1/(bw**4*alphaf**2)*(KrII/betal**2+(
    2*KrII/(betaf*betal))+KrII/betaf**2)
Kr[5, 5] = 1/(bw**4*alphaf**2)*(KrII/(betal**2))
Kr[0, 1] = Kr[1, 0] = 1/(bw**4*alphaf**2)*(-KrI/(betal**2)-
    KrI/(betal*betaf))
Kr[0, 2] = Kr[2, 0] = 1/(bw**4*alphaf**2)*(KrI/(betal)+KrI/(betal*betaf))
Kr[0, 3] = Kr[3, 0] = 1/(bw**4*alphaf**2)*(-KrI/(betal))
Kr[1, 2] = Kr[2, 1] = 1/(bw**4*alphaf**2)*(-KrI/(betal)-KrI/(betal*betaf)-
    KrI/(betaf)-KrI/(betaf**2))
Kr[1, 3] = Kr[3, 1] = 1/(bw**4*alphaf**2)*(KrI/(betal)+KrI/(betaf))
Kr[2, 3] = Kr[3, 2] = 1/(bw**4*alphaf**2)*(-KrI-KrI/(betaf)-
    KrII/(betaf)-KrII)
Kr[2, 4] = Kr[4, 2] = 1/(bw**4*alphaf**2)*(KrII/(betal)+KrII/(betaf))
Kr[2, 5] = Kr[5, 2] = 1/(bw**4*alphaf**2)*(-KrII/(betal))
Kr[3, 4] = Kr[4, 3] = 1/(bw**4*alphaf**2)*(-KrII/(betal)-KrII /
    (betaf*betal)-KrII/(betaf)-
    KrII/(betaf**2))
Kr[3, 5] = Kr[5, 3] = 1/(bw**4*alphaf**2)*(KrII/(betal)+KrII/(betaf*betal))
Kr[4, 5] = Kr[5, 4] = 1/(bw**4*alphaf**2)*(-KrII/(betal**2)-
    KrII/(betaf*betal))

# (I.iv) Determination of the matrix elastic restraint springs - Eq. (27)
Bs = Kz+Ky+Kr; B = Bf+Bs;
# (Annex A.vi) Symmetric warping stiffness matrix C - Eq. (A.6)
C = np.zeros([6, 6])
C[0, 0] = C[5, 5] = E*bw*t/3*(alpha1);
C[1, 1] = C[4, 4] = E*bw*t/3*(alpha1+alphaf)
C[2, 2] = C[3, 3] = E*bw*t/3*(1+alphaf)
C[0, 1] = C[1, 0] = C[4, 5] = C[5, 4] = E*bw*t/6*(alpha1)
C[1, 2] = C[2, 1] = C[3, 4] = C[4, 3] = E*bw*t/6*(alphaf);
C[2, 3] = C[3, 2] = E*bw*t/6
Ci = np.linalg.inv(C)
s1 = np.matmul(Ci, B)
# Task II - Numerical Solution of the 6th-Order Eigenvalue Problem - Eq. (28)
Eva = np.linalg.eig(s1)
GBTeve = Eva[1].real
# (II.i) Nodal warping displacements associated with LD or D - Eq. (29)
if SM == "P":
    vector = np.copy(GBTeve[:, 3:4]) # (II.i.1)
elif SM == "S":
    vector = np.copy(GBTeve[:, 1:2]) # (II.i.2)
else:
    vector == "Insert a valid Structural Member option"
u = np.zeros(6)
for i in range(6):

```

```

        mx = max(abs(vector))
        u[i] = vector[i]/mx # normalizing as proposed in [22]
# (II.ii) Transverse bending moment vector - Eq. (30)
m = np.matmul(M, u)
# Task III - Modal Displacements and Mechanical/Geometric Properties
# (III.i) - In-plane(v) and flexural(w) displacements, and rotations(theta)
# Annex B - Eqs. (B.1), (B.2) and (B.3)
v = np.zeros(5)
v[0] = (u[0]-u[1])/(bw*alpha1); v[1] = (u[1]-u[2])/(bw*alpha1);
v[2] = (u[2]-u[3])/bw; v[3] = (u[3]-u[4])/(bw*alpha1);
v[4] = (u[4]-u[5])/(bw*alpha1)
theta = np.zeros(5)
theta[1] = 1/(alpha1*bw)*(-v[0]/sin(phi*pi/180)+v[1]/tan(phi*pi/180)-v[2]);
theta[2] = -1/bw*(v[1]+rho*v[3]);
theta[3]=rho/(alpha1*bw)*(-v[4]/sin(phi*pi/180)+v[3]/tan(phi*pi/180)-v[2]);
theta[0] = theta[1]+alpha1*bw*m[2]/(6*K);
theta[4] = theta[3]-alpha1*bw*m[3]/(6*K);
w = np.zeros(5)
w[0] = -alpha1*bw*theta[0]/2-v[1]/sin(phi*pi/180)+v[0]/tan(phi*pi/180);
w[1] = 0.5*(v[0]/sin(phi*pi/180)-v[1]/tan(phi*pi/180)-v[2]);
w[2] = 0.5*(v[1]-rho*v[3]);
w[3] = rho/2*(-v[4]/sin(phi*pi/180)+v[3]/tan(phi*pi/180)+v[2]);
w[4]=alpha1*bw*theta[4]/2+rho*(v[3]/sin(phi*pi/180)-v[4]/tan(phi*pi/180));
#(III.ii) Cross-section modal mechanical properties - Eq. B.4 - B.6
C=1/3*E*t*bw*(alpha1*(u[0]**2+u[0]*u[1]+u[1]**2+u[4]**2+u[4]*u[5]+u[5]**2)+
alpha1*(u[1]**2+u[1]*u[2]+u[2]**2+u[3]**2+u[3]*u[4]+u[4]**2)
+u[2]**2+u[2]*u[3]+u[3]**2)
B = bw/(3*K)*(alpha1*m[2]**2+m[3]**2+m[3]*m[2]+m[2]**2+alpha1*m[3]**2)+(
KtgI*v[1]**2 + KtnI*w[1]**2+KrI*theta[1]**2+
KtgII*v[3]**2+KtnII*w[3]**2+KrII*theta[3]**2)
D = bw*G*t**3/3*((theta[0]**2+theta[4]**2)*alpha1+
(theta[1]**2+theta[3]**2)*alpha1+theta[2]**2)
# (III.iii) Determination of the nodal axial displacement vectors - Eq. (B.12)
U = np.zeros(6)
if SM == "S":
    for i in range(6):
        U[i] = 1
    H = bw*t*(2*alpha1+2*alpha1+1)
elif SM == "P":
    U[0] = -bw*(0.5-beta1)
    U[1] = U[2] = -0.5*bw
    U[3] = U[4] = 0.5*bw
    U[5] = bw*(0.5-beta1)
    H = bw*t/12*(bw**2*(1+6*alpha1+2*alpha1*(4*beta1**2-6*beta1+3)) +
2*t**2*(alpha1+alpha1-beta1*sin(phi*pi/180)))
else:
    vector == "Insert a valid Structural Member option"
# (III.iv) Cross-section modal geometrical properties - Eqs. (B.7)-(B.11)
X = np.zeros(5)
X[0] = 15120*K**2*(alpha1*((v[0]**2+w[0]**2)*(U[0]+U[1])+
(v[4]**2+w[4]**2)*(U[4]+U[5]))+
alpha1*((v[1]**2+w[1]**2)*(U[1]+U[2])+
(v[3]**2+w[3]**2)*(U[3]+U[4]))+
(v[2]**2+w[2]**2)*(U[2]+U[3]))
X[1] = 1260*K**2*bw**2*(alpha1**3*(theta[0]**2*(U[0]+U[1])+
theta[4]**2*(U[4]+U[5]))+
alpha1**3*(theta[1]**2*(U[1]+U[2])+
theta[3]**2*(U[3]+U[4]))+
theta[2]**2*(U[2]+U[3]))
X[2] = 5040*K**2*bw*(alpha1**2*(theta[0]*w[0]*(U[1]-U[0])+
theta[4]*w[4]*(U[5]-U[4]))+
alpha1**2*(theta[1]*w[1]*(U[2]-U[1])+
theta[3]*w[3]*(U[4]-U[3]))+ theta[2]*w[2]*(U[3]-U[2]))
X[3] = bw**4*(m[2]**2*(alpha1**5*(29*U[1]+35*U[2])+(29*U[3]+35*U[2]))+

```

```

m[3]**2*(alphaf**5*(29*U[4]+35*U[3])+(29*U[2]+35*U[3]))+
62*m[2]*m[3]*(U[2]+U[3]))
X[4] = 84*K*bw**2*(alphaf**3*(m[2]*w[1]*(16*U[2]+14*U[1])+
m[3]*w[3]*(16*U[3]+14*U[4]))+
w[2]*(m[2]*(16*U[2]+14*U[3])+m[3]*(16*U[3]+14*U[2]))+
bw*(alphaf**4*(m[2]*theta[1]*(2*U[2]-U[1])+m[3]*theta[3]*(U[4]-2*U[3]))+
theta[2]*(m[2]*(U[3]-2*U[2])+m[3]*(2*U[3]-U[2]))))
X = bw*t/(30240*K**2*H)*np.sum(X)
# Minimum bifurcation moment/load parameter - Eq. (23)
Lcri = pi*(C/B)**0.25
Lambda = (2*(C*B)**0.5+D)/X
# Buckling moment/load parameter - Eq. (22)
def P(L, n): # L=Member Length n=longitudinal half-waves
    P = ((pi*n/L)**2*C+(L/(pi*n))**2*B+D)/X
    return P

```

Inputs

SM	“S” for studs or “P” for purlins
bw	Web width
bf	Flange width
bl	Lip width
ϕ	Lip inclination w.r.t. the horizontal direction (degrees)
t	Wall thickness
rho	Cross-section shape identification factor: “1” for C or “-1” for Z
E	Young’s modulus
nu	Poisson’s ration
KtgI and KtgII	Tangential spring stiffness values (upper and lower flange, respectively)
KtnI and KtnII	Transversal spring stiffness values (upper and lower flange, respectively)
KrI and KrII	Rotational spring stiffness values (upper and lower flange, respectively)
n	Half-wave number
L	Member length

Outputs

alphaI, alphaf, betal, betaf	Geometrical parameters
K, G	Mechanical parameters
F	Flexibility matrix
Stif	Transverse stiffness matrix
ww	Wall relative rotation matrix
M	Transverse bending moment matrix
Bf	Flexural matrix
Kz, Ky and Kr	Tangential, transversal and rotational spring stiffness matrices
Bs	Elastic spring matrix
C	Warping matrix
Eva	Eigenvalues in descending order
u	Warping displacements of the deformation mode
m,v,theta,w	Modal transverse bending moments and displacements(in plane, rotation and flexural)
C,B,D	Cross-section modal mechanical properties
U	Nodal axial displacements due to the applied load
X	Cross-section modal geometrical properties
Lcri, Lambda	Critical length and load parameters
P(L,n)	Critical moment/load of a member with length “L” and buckling in “n” half-waves